Die approbierte Originalversion dieser Diplom-/Masterarbeit ist in der Hauptbibliothek der Technischen Universität Wien aufgestellt und zugänglich.
http://www.ub.tuwien.ac.at

The approved original version of this diploma or master thesis is available at the main library of the Vienna University of Technology.
http://www.ub.tuwien.ac.at/eng

TECHNISCHE UNIVERSITÄT WIEN

D I P L O M A R B E I T

# Simulation of the Pulmonary Circulation: Model Comparison and Implementation

Ausgeführt am Institut für
Analysis und Scientific Computing
der Technischen Universität Wien

unter Anleitung von
A.o.Univ.Prof. Dipl.-Ing. Dr.techn. Felix Breitenecker
und
Univ.Lektor Dipl.-Ing. Dr.techn. Bernhard Hametner

durch
Claudia Wytrzens

Ort, Datum

Unterschrift

# Abstract

Pulmonary hypertension is a severe and incurable disease. It can even lead to heart failure. Thus, it is important to diagnose this type of disease as early as possible. Since blood pressure in the pulmonary circulation can only be obtained via invasive measurements, which is not an easy task, mathematical models for blood pressure and flow in this system are of great importance. Also in terms of investigating pressure and flow waveforms with respect to find significant parameters for distinguishing several disease stages of pulmonary hypertension, mathematical models are used.

In this thesis three different approaches of modelling the pulmonary circulation, which are most commonly applied for simulation in literature, are investigated. The mathematical formulation of each of these modelling approaches is derived in more detail and also some examples of applications in literature are given. The first modelling theory that is considered is the so called Windkessel model. It can be described by an ordinary differential equation of first order and is often related to an electrical circuit. It is a lumped parameter model and hence does not take spatial distribution of pressure and flow into account. The second model that is examined is based on the one-dimensional linearised Navier-Stokes equations, also referred to as Womersley equations. They are derived from the Navier-Stokes equations for Newtonian fluids. An advantage of this approach is, that it also considers spatial distribution and the possibility of wave reflections. The last approach taken into account is the system of one-dimensional non-linear Navier-Stokes equations. They are commonly solved numerically by finite element schemes and by using structured trees as outlet boundary conditions. Thereby, especially the pressure and flow waveforms in the small arterioles, capillaries and small venules can be simulated by the structured trees.

Furthermore, in terms of application of the Windkessel modelling method to the pulmonary circulation, an $RC$-tree model was implemented. The $RC$-tree model is a branching tree model based on 2-element Windkessel models for each vessel. For simulation 17 generations of pulmonary arterial vessels were considered. In the model the generations are connected in series while vessels within a specific generation are seen as parallel. The parallel vessels of one generation have the same resistances and compliances. This $RC$-tree modelling method is especially used to simulate the effects of different degrees of occlusion in different generations of the considered branching tree.

Comparing the mathematical formulations with one another leads to significant differences of the models. The most remarkable distinction of the two methods based on the Navier-Stokes equations is that for the Womersley equations stronger assumptions are needed than for the one-dimensional non-linear Navier-Stokes equations. The main difference between the one-dimensional models (one-dimensional linearised and non-linear Navier-Stokes equations) and the Windkessel modelling method is that the latter is a lumped parameter model and that

it does not take spatial distribution into account. Therefore, wave reflections and thus forward and backward travelling waves can only be investigated via the approaches based on the Navier-Stokes equations. Literature review also showed that different types and disease stages of pulmonary hypertension can be distinguished by all three modelling methods. Moreover, via the Windkessel models $RC$-time was identified to be constant throughout all patients with and without pulmonary hypertension. However, on the assumption of constant compliance and the possibility of occlusion of vessels the simulation results of the $RC$-tree model did not show this characteristic. Thus, it did not explain constant $RC$-time which was stated in the literature.

Altogether, in the course of this thesis, three different main approaches of modelling and simulating the pulmonary circulation found in literature were studied. In terms of simulation of the pulmonary circulation each of these modelling methods has its advantages and disadvantages. So, applying one of these models to the pulmonary circulation also depends on the order of detail and complexity, which is needed for modelling a specific problem. Furthermore, it was possible to distinguish between healthy and ill patients by each of the considered types of models. Lastly, especially effects of occlusion on the pulmonary circulation could be seen in the simulation results of the own implemented $RC$-tree model. The qualitative behaviour of the results was concluded to be similar to simulation results stated in literature.

# Kurzfassung

Pulmonale Hypertonie ist eine ernstzunehmende Krankheit, die unheilbar ist und sogar zum Herzversagen führen kann. Daher ist eine frühe Diagnose dieser Krankheit sehr wichtig. Da jedoch der Blutdruck im pulmonalen Kreislauf nur invasiv gemessen werden kann und dies vor allem in den kleineren Gefäßen eine Herausforderung darstellt, werden mathematische Methoden zur Modellierung von Blutdruck und -fluss verwendet. Außerdem werden diese Modelle auch eingesetzt, um signifikante Parameter zur Differenzierung verschiedener Arten pulmonaler Hypertonie anhand zugehöriger Druck- und Flusskurven zu identifizieren.

Im Rahmen dieser Arbeit werden drei verschiedene Methoden zur Modellierung ebendieses Kreislaufs betrachtet. Diese drei Methoden kommen in der Literatur bezogen auf die Simulation des pulmonalen Kreislaufs am häufigsten zum Einsatz. Es werden sowohl mathematische Formulierungen und Herleitungen dieser drei Modelle als auch exemplarische Anwendungen in der Literatur erläutert. Einer der Ansätze zur Modellierung, der in dieser Arbeit berücksichtig wird, ist das sogenannte Windkesselmodell. Es kann über eine lineare Differentialgleichung erster Ordnung beschrieben werden und wird oftmals auch als elektrischer Schaltkreis dargestellt. Das Windkesselmodell ist ein Modell, welches die Veränderung von Druck und Fluss in einem Gefäß über die Zeit ohne Ortsausbreitung modelliert. Der zweite Ansatz, auf den in der Arbeit näher eingegangen wird, basiert auf den sogenannten Womersley Lösungen. Dies sind Lösungen von eindimensionalen linearisierten Navier-Stokes Gleichungen für Newtonsche Flüssigkeiten. Einer der Vorteile dieses Modellierungsansatzes ist, dass nun sowohl räumliche Ausbreitung als auch eventuell auftretende Wellenreflexionen modelliert werden können. Die dritte betrachtete Modellierungsmethode bezieht sich auf die eindimensionalen nicht-linearisierten Navier-Stokes Gleichungen. Diese werden oftmals numerisch über Finite-Elemente-Methoden gelöst, wobei als rechte Randbedingung sehr häufig ein Strukturbaum der kleinsten Blutgefäße verwendet wird. Dadurch können insbesondere Druck und Fluss in den kleinen Arteriolen und Venolen sowie Kapillaren modelliert und simuliert werden.

Darüber hinaus wurde ein $RC$-Baum zur Simulation des pulmonalen Kreislaufs implementiert. Über einen $RC$-Baum ist es möglich den Arterienbaum im pulmonalen Kreislauf zu modellieren. Der $RC$-Baum basiert auf 2-elementigem Windkesselmodellen, wobei jedes der betrachteten Gefäße vermittels eines 2-elementigen Windkesselmodells dargestellt wird. Zur Simulation dieses Modells wurden 17 Generationen pulmonaler Blutgefäße in das Modell integriert. Zur Modellierung wurden die einzelnen Generationen seriell hintereinander geschaltet. Gefäße innerhalb einer Generation wurden als parallel angesehen und hatten dieselben Widerstände und Compliances als Parameter. Das $RC$-Baum Modell bietet auch die Möglichkeit der Simulation von Gefäßverschlüssen unterschiedlichster Ordnungen im pulmonalen Arterienbaum.

Der Vergleich der unterschiedlichen Modellierungsmethoden, die im Zuge der Arbeit in Betracht gezogen wurden, lässt deutliche Unterschiede der Modelle erkennen. Einen der sig-

nifikantesten Unterschiede zwischen den beiden Ansätzen, die auf den Navier-Stokes Gleichungen basieren, stellen die unterschiedlich starken Annahmen für deren Herleitungen dar. Eine sehr charakteristische Eigenschaft der eindimensionalen Modelle verglichen zum Windkesselmodell ist, dass die erstgenannten auch örtliche Ausbreitung von Druck- und Flusswellen in Betracht ziehen. Somit können auch Wellenreflexionen sowie vorwärts- und rückwärtslaufende Wellen mit Hilfe der eindimensionalen Modelle berücksichtigt werden. Die durchgeführte Literaturrecherche ließ außerdem darauf schließen, dass verschiedene Krankheitsgrade und –arten pulmonaler Hypertonie mit Hilfe der drei betrachteten Modelle unterschieden werden können. Für diese Differenzierung können verschiedenste Parameter der Modellierungsmethoden betrachtet werden. Außerdem wurde die $RC$-Zeit, unabhängig von der Patientengruppe und des zugehörigen Krankheitsgrades pulmonaler Hypertonie, als konstant identifiziert. Jedoch konnte dieses Verhalten der $RC$-Zeit nicht unter der Annahme von konstanter Compliance und der Möglichkeit des Gefäßverschlusses in den Simulationsergebnissen des $RC$-Baum Modells beobachtet und erklärt werden.

Zusammengefasst kann gesagt werden, dass im Zuge dieser Arbeit die drei häufigsten Modellierungsmethoden zur Simulation des pulmonalen Kreislaufs in der Literatur studiert wurden. Jede dieser Methoden zur Modellierung des pulmonalen Kreislaufs hat Vor- und Nachteile bezogen auf die Simulation dieses Kreislaufs. Im Kontext einer gewissen Fragestellung hängt es insbesondere von der geforderten Komplexität und der Detailliertheit ab welches der Modelle zur Simulation des pulmonalen Kreislaufs angewandt werden sollte. Es war außerdem auch möglich zwischen gesunden und kranken Personen mit Hilfe jedes der drei Modelle zu differenzieren. Schlussendlich konnten auch Auswirkungen von Gefäßverschlüssen im pulmonalen Kreislauf betrachtet werden. Diese Auswirkungen wurden in den Simulationsergebnissen des implementierten $RC$-Baums untersucht. Zugleich wurde darauf geschlossen, dass das qualitative Verhalten der Simulationsergebnisse ähnlich zu Ergebnissen aus der Literatur ist.

# Danksagung

An dieser Stelle möchte ich mich bei all denjenigen bedanken, die zum Entstehen dieser Arbeit beigetragen haben und mich während meines Studiums unterstützt, motiviert und im Gebet getragen haben.

Mein besonderer Dank gilt Professor Felix Breitenecker für die Betreuung dieser Diplomarbeit und für die vielen Erfahrungen, die ich im Zuge meiner Tätigkeiten in seiner Forschungsgruppe sammeln durfte. Außerdem möchte ich mich bei ihm für die Möglichkeiten der Teilnahme an verschiedensten Konferenzen, Summerschools und sozialen Events bedanken.

Weiters möchte ich mich sehr herzlich bei all meinen Kolleginnen und Kollegen am Austrian Institute of Technology bedanken. Ich habe die Zeit mit ihnen in den letzten Jahren sehr genossen. Ganz besonders möchte ich Bernhard Hametner vor allem für seine Betreuung und die großartige Unterstützung und Geduld danken. Ich sehe es nicht als Selbstverständlichkeit an, dass ich jederzeit mit Fragen zu ihm kommen konnte, um Denkanstöße und neue Anregungen zu bekommen. Herzlichen Dank auch für die vielen Stunden, die er in das Korrekturlesen meiner Arbeit investiert hat. Des Weiteren möchte ich auch Siegfried Wassertheurer meinen Dank aussprechen, durch den ich schon davor die Möglichkeit hatte in das Gebiet der Herzkreislaufsimulation am AIT hineinzuschnuppern. Außerdem hat er es mir ermöglicht meine Diplomarbeit im Zuge eines FEMtech Praktikums am AIT zu bearbeiten. Vielen Dank auch an Stephanie Parragh, die immer ein offenes Ohr für meine Fragen hatte und auch immer ein aufmunterndes und motivierendes Wort für mich hatte.

Der Abschluss meines Studiums wäre mir nicht gelungen ohne die gute und fruchtbare Zusammenarbeit mit meinen Studienkolleginnen und Studienkollegen all die Jahre über. Namentlich möchte ich hier nur Andi, Fabian, Lisi und Steffi nennen, die sich dankenswerterweise die Mühe gemacht haben meine Arbeit Korrektur zu lesen. Großen Dank auch an Philipp, der mich seit dem ersten Tag meines Studiums begleitet und immer wieder aufs Neue motiviert hat.

Mein tiefster Dank gebührt meiner Familie und meinen Freunden, die mich vor allem in der letzten Phase meines Studiums ertragen haben und mich immer wieder aufgebaut und motiviert haben. Allen voran möchte ich mich von ganzem Herzen bei meinen Eltern, nicht nur für die finanzielle Unterstützung sondern auch für den Rückhalt und die Sicherheit, die sie mir all die Jahre über gegeben haben, bedanken. Auch meinen Geschwistern möchte ich Dank sagen dafür, dass sie mich immer unterstützt haben und mir in jeder Lebenslage zur Seite standen.

# Contents

**Abstract** **iii**

**Kurzfassung** **v**

**Danksagung** **vii**

**List of Abbreviations** **xi**

**1 Introduction** **1**
1.1 Motivation . . . . . 1
1.2 Aim of the Thesis . . . . . 1
1.3 Thesis Outline . . . . . 2

**2 The Cardiovascular System** **3**
2.1 Physiology of the Pulmonary Circulation . . . . . 3
2.1.1 Anatomy of the Pulmonary Circulation . . . . . 3
2.1.2 Pulmonary Blood Flow and Pressures . . . . . 5
2.1.3 Morphometry of the Pulmonary Circulation . . . . . 9

**3 Mathematical Models of the Pulmonary Circulation** **11**
3.1 Windkessel Model . . . . . 11
3.1.1 Mathematical Derivation and Formulation . . . . . 11
3.1.2 Literature Review of Applications of the Windkessel Model in the Pulmonary Circulation . . . . . 14
3.2 One-Dimensional Linearised Navier-Stokes Equations (Womersley Equations) . . 26
3.2.1 Mathematical Derivation and Formulation . . . . . 26
3.2.2 Literature Review of Applications of the Womersley Equations in the Pulmonary Circulations . . . . . 34
3.3 One-Dimensional Non-Linear Navier-Stokes Equations . . . . . 43
3.3.1 Mathematical Derivation and Formulation . . . . . 43
3.3.2 Literature Review of Applications of the One-Dimensional Non-Linear Navier-Stokes Equations in the Pulmonary Circulation . . . . . 49

**4 Comparison and Discussion of the Mathematical Models** **61**

**5 Simulation of the Pulmonary Circulation** **67**
5.1 Implementation of a 2-element Windkessel Model . . . . . 67
5.2 Implementation of an *RC*-tree Model . . . . . 67
5.3 Results . . . . . 70
5.3.1 Simulation Results for Occlusion . . . . . 72
5.4 Conclusion . . . . . 77

**List of Figures** **80**

**List of Tables** **81**

**Bibliography** **85**

# List of Abbreviations

| | |
|---|---|
| **CO** | cardiac output |
| **CT** | computer tomography |
| **CTEPH** | chronic thromboembolic pulmonary hypertension |
| **HLD** | hypoxic lung disease |
| **IPAH** | idiopathic pulmonary arterial hypertension |
| **LA** | left atrium |
| **LIA** | left interlobular artery |
| **LIV** | left inferior pulmonary vein |
| **LPA** | left pulmonary artery |
| **LSV** | left superior pulmonary vein |
| **LTA** | left trunk artery |
| **MPA** | main pulmonary artery |
| **MRI** | magnet resonance imaging |
| **NONPH** | no pulmonary hypertension |
| **PAH** | pulmonary arterial hypertension |
| **PH** | pulmonary hypertension |
| **PVR** | pulmonary vascular resistance |
| **RIA** | right interlobular artery |
| **RIV** | right inferior pulmonary vein |
| **RPA** | right pulmonary artery |
| **RSV** | right superior pulmonary vein |
| **RTA** | right trunk artery |
| **RV** | right ventricle |

# 1 Introduction

## 1.1 Motivation

Pulmonary hypertension is a rare disease [5, 21]. It is also a very severe disease which can even lead to heart failure [5, 21]. Pulmonary hypertension occurs when blood pressure in the pulmonary arteries is raised. This means that at rest the mean blood pressure equals or is greater than 25 mmHg in the pulmonary artery. This raised blood pressure is due to pulmonary vascular remodelling and eventually restriction of the blood flow. [5]

By the World Health Organisation pulmonary hypertension is classified into 5 groups: pulmonary arterial hypertension (PAH), pulmonary hypertension caused by left heart disease, pulmonary hypertension caused by lung diseases and/or hypoxia, chronic thromboembolic pulmonary hypertension (CTEPH) and pulmonary hypertension caused by multifactorial mechanisms [5, 21]. In Western countries the most common causes for pulmonary hypertension are left heart disease and chronic hypoxic lung disease [21, 5]. In contrast to this, the main reasons for pulmonary hypertension in developing countries are sickle cell disease and schistosomiasis [5, 21]. The gold standard for the diagnosis of pulmonary hypertension is right heart catheterization, which is an invasive procedure [5]. But also non-invasive techniques are taken into account such as echocardiography or magnet resonance imaging (MRI) measurements, which is the gold standard for right ventricle (RV) volume measurements [5].

In the last two decades the knowledge about this disease has improved immensely, but further research still needs to be done as there is no cure for pulmonary hypertension [5, 21]. Hence, it is of great importance to be able to diagnose the disease as early as possible. Therefore, it is also beneficial to increase knowledge of pressures and flows in the pulmonary circulation. To achieve this task mathematical models are of great importance, since measuring pressures and flows in the lungs, especially in the capillary bed, is not an easy task and has to be done invasively.

## 1.2 Aim of the Thesis

The aim of this thesis can be separated into two goals: First of all, the identification, derivation and comparison of the most common mathematical models applied to the pulmonary circulation in literature. Secondly, the implementation of an $RC$-tree model, based on Lankhaar [14], as well as simulation of blood pressure in the pulmonary circulation during occlusion of pulmonary arterial vessels.

## 1.3 Thesis Outline

In Chapter 1 the thesis is motivated and the aim is specified. A short introduction into the human cardiovascular system focused on the pulmonary circulation and its features is given in Chapter 2. Chapter 3 deals with the three most common mathematical models for simulation of the pulmonary circulation in literature. Specifically, the Windkessel modelling, Womersley equations' and one-dimensional non-linearised Navier-Stokes equations' approaches are considered and their mathematical formulation are taken into account in more detail as well as their simulations in literature. Furthermore, these three modelling techniques are compared and discussed in Chapter 4. Chapter 5 provides the implementation of an RC-tree model, based on [14], as well as the implementation of an 2-element Windkessel model and their simulation results. Moreover, the obtained simulation results are compared to results from literature in this chapter.

# 2 The Cardiovascular System

The human cardiovascular system is composed out of the systemic and the pulmonary circulations. It is responsible for transporting oxygen and nutrients to the tissue and removing waste products from the tissue. Its driving force is the pumping heart, which can be divided into the left and right heart. The right heart is in charge of pumping the blood into the lungs, whereas the left heart is responsible for blood supply of the systemic part. Oxygenated blood flows from the left atrium into the left ventricle. There it is ejected via contraction through the aortic valve into the aorta and the subsequent systemic arteries. The blood further traverses via the small arterioles into the capillaries, where the gas exchange takes place. The now de-oxygenated blood travels through the small venules into the veins and eventually into the right atrium and right ventricle. In the right ventricle blood enters the pulmonary circulation. This is again caused by contraction. From the right ventricle the de-oxygenated blood is ejected through the pulmonary valve into the main pulmonary artery. The blood further flows through the pulmonary arterial system into the alveoli. There gas is exchanged. The now oxygenated blood flows through the pulmonary venous system back to the left atrium (LA) of the heart, where the pulmonary circulation terminates.

As already mentioned the heart is pumping the blood periodically into the cardiovascular system. This is based on contraction and relaxation. The period of contraction is called systole and starts with opening the aortic and pulmonary valves. At the point in time when the valves close diastole and hence a period of relaxation begins. During this time period the heartchambers are again filled with blood. Hence, a cardiac cycle is composed of systole and diastole. [11, 13]

The described circulation of the blood throughout the cardiovascular system is depicted on the right side of Figure 2.1. On the left side this figure also shows the before described course of the blood flow through the four chambers of the heart.

## 2.1 Physiology of the Pulmonary Circulation

In the following Section 2.1.1 the vasculature of the pulmonary circulation will be described according to [11, 6, 4] and in Section 2.1.2 the pressures and blood flows, which control the pulmonary circulation are explained following [11], if not stated differently. All values given in Section 2.1.2 are also taken from [11], if not explicitly specified.

### 2.1.1 Anatomy of the Pulmonary Circulation

The pathway from the heart to the alveoli and back to the heart is given by the pulmonary vasculature. Its main artery - the pulmonary trunk, also called the main pulmonary artery (MPA) - originates from the RV and therefore is the stem of the pulmonary arterial tree. The

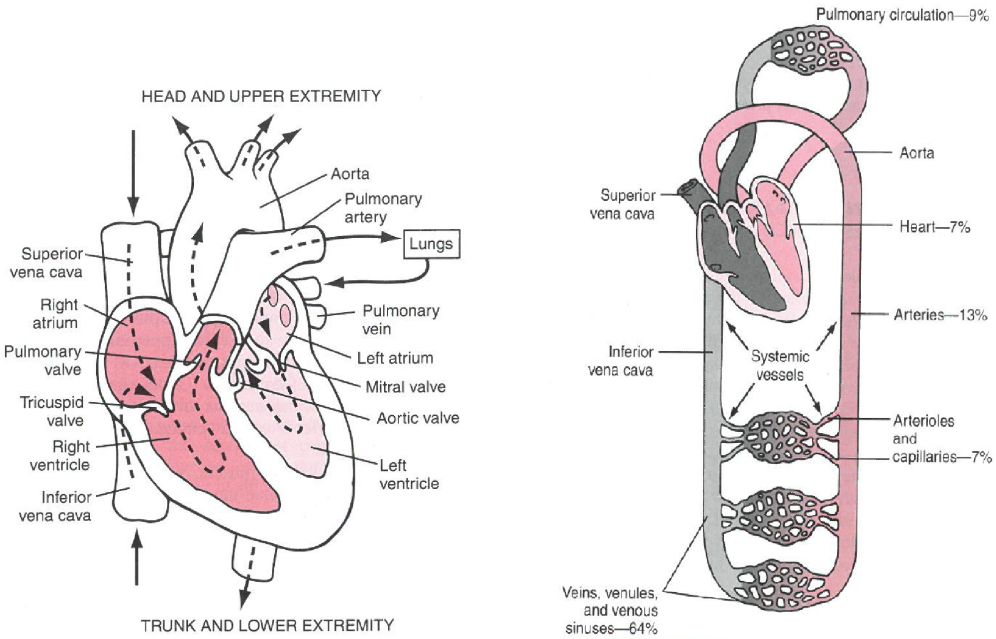


(a) Blood flow through the heart

(b) Blood circulation through the entire cardiovascular system

Figure 2.1: Circulation of the blood through (a) the four chambers of the heart and (b) the whole cardiovascular system with the amount of blood volume in the different parts of the system. (Source: [11, p. 97, p. 145])

pulmonary trunk is about 5 - 6 cm long [6] and has a circumference of about 2.5 - 3 cm [6]. It is of tapered shape [26]. Moreover, its wall is very thin, with a wall thickness of about one third that of the aorta and around twice the thickness of the venae cavae respectively. It bifurcates into two arteries: the left pulmonary artery (LPA) and right pulmonary artery (RPA). Those two arteries supply the left and the right lung with blood accordingly. The two lungs together are subdivided into 5 different lobes, which are functionally independent of each other. Because of the position of the heart, the right pulmonary artery is generally larger and longer than its left counterpart. Moreover, the left lung is in total smaller than the right. As the left and right pulmonary arteries enter the lungs their branches begin to divide into pulmonary arteries, smaller arteries and arterioles as long as they eventually form capillaries around the alveoli. In the alveoli gas exchange and hence aeration of the blood takes place. From there venules originate from the pulmonary capillaries. These venules unite to form pulmonary veins. The four main pulmonary veins emerge from the two lungs. As the veins of the right upper and middle lobe are merging into one vein, each side is supported by two veins, a superior and inferior vein. Therefore, the two left and two right pulmonary veins lead into the LA. These characteristics of the pulmonary circulation can be seen in Figure 2.2.

In contrast to the pulmonary arterial tree, which traverses the lung following the bronchial tree, the pulmonary venous tree evolves independently of the arteries and bronchi. Moreover, the pulmonary veins are short and they do not feature valves unlike most of the systemic veins. But

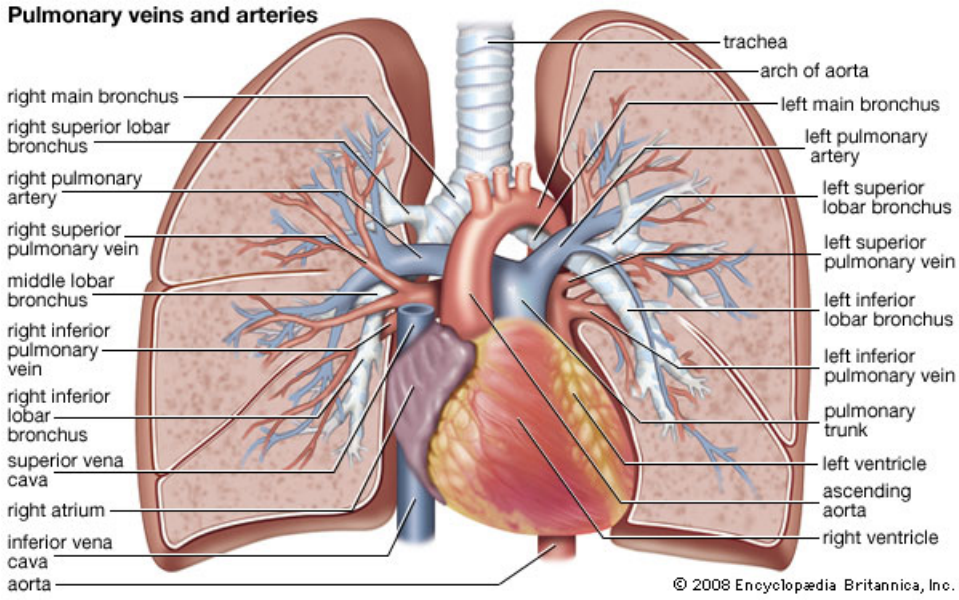


Figure 2.2: Schematic representation of the pulmonary circulation, with the heart, the arteries and veins in the right and left lung, as well as the bronchial tree. (Source: [9])

they are, like their systemic counterparts, thin walled and have similar distensibility properties.

A main difference between the pulmonary arterial tree and the systemic arterial tree is that the pulmonary branches are very short compared to the systemic ones. Furthermore, all the pulmonary arteries and arterioles on the one hand have larger diameters and on the other hand have considerably thinner walls than their systemic counterparts. These properties as well as the fact that pulmonary arteries are very distensible are responsible for the large compliance of the pulmonary arterial tree. This compliance is quite similar to the compliance of the whole systemic arterial tree and on average takes the value of about 7 ml/mmHg [4]. Hence, around two thirds of the right ventricle's stroke volume's output can be stored in the pulmonary arteries. A further difference between the pulmonary and the systemic circulation is that the number of peripheral vessels is $\sim 8 - 10$ times higher in the pulmonary system [24].

### 2.1.2 Pulmonary Blood Flow and Pressures

In the RV the pressure during the systole is on average about 25 mmHg, which is about one fifth that of the left ventricle, and 0-1 mmHg during diastole respectively. Hence, the pressure during systole in the pulmonary trunk is the same as in the RV. After closure of the pulmonary valve the pressure in the pulmonary trunk drops slower due to the blood flowing through the pulmonary capillaries. Therefore, the pressure in the pulmonary trunk during diastole averages about 8 mmHg. The mean pressure in this vessel is 15 mmHg. These different pressures are illustrated in Figure 2.3, in which the pulmonary trunk and RV pressure curves are also compared to the aortic pressure curve. The mean pressure in the pulmonary capillaries takes the value of around 7 mmHg, which is notably lower than the capillary pressure in the systemic circulation

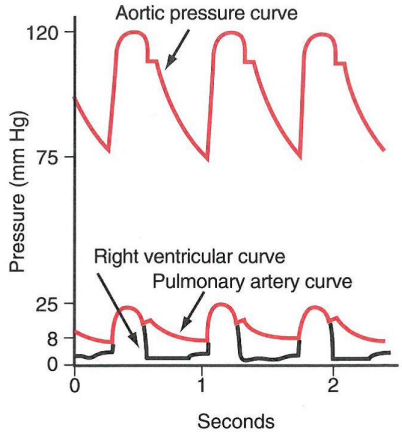


Figure 2.3: Pressure pulse curves in the pulmonary artery (red line) and the right ventricle (black line) at the bottom, and that in the aorta at the top for comparsion. It can be seen that during diastole the blood pressure in the pulmonary artery drops more slowly than in the right ventricle (RV). (Source: [11, p. 445])

of 17 mmHg. Furthermore, in the main pulmonary veins as well as in the left atrium the mean pressure varies from values of 1 mmHg up to 5 mmHg and averages about 2 mmHg in a lying person. This distribution of the pressure throughout the pulmonary circulation is illustrated in Figure 2.4.

The pulmonary circulation normally accommodates a blood volume of about 450 ml, which is only around 9% of the overall blood volume in the cardiovascular system. But this amount of blood volume in the lungs can vary from half of the normal amount up to twice of the normal volume because of many different physiologic and pathologic reasons. Since the blood volume of the lungs is just about one ninth of the systemic circulation, shifting blood from one system to the other has greater effects on the pulmonary than on the systemic system. Nevertheless, the cardiac output (CO) of the pulmonary system is the same as of the systemic system [24, 13]. Since the CO is equal to the blood flow in the lungs, the pulmonary blood flow is controlled by factors which also control the CO. The pulmonary vessels are normally like passive distensible tubes under most conditions. With increasing pressure the pulmonary vessels are enlarging and they are narrowing with decreasing pressure, contrariwise.

Furthermore, the distribution of the blood in the lungs in some way is also controlled by the oxygen concentration of the alveoli. If this concentration drops below the normal concentration, that is 73 mmHg $PO_2$, the adjoining vessels constrict during the following 3 to 10 minutes. So, at very low oxygen levels the vascular resistance can raise up to the fivefold of its normal value. Especially the vasoconstriction induced by poor ventilation leading to low $O_2$ saturation of the alveoli is quite contrary to the effect of low oxygen concentration in the systemic circulation, as vessels would rather dilate. But this effect in the pulmonary circulation is quite important in its function since blood can be distributed to regions of the lungs where it is most effective. Thereby, the blood is forced to flow to areas where alveoli are better oxygenated.

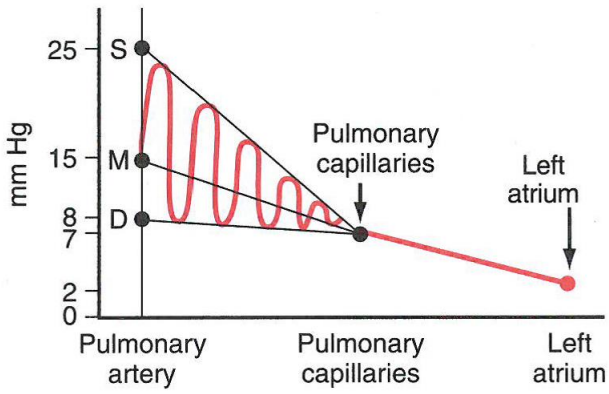


Figure 2.4: Distribution of the pressure in the different vessels of the lungs beginning at the pulmonary artery, leading to the pulmonary capillaries and terminating in the LA. S = systolic pressure, M = mean pressure, D = diastolic pressure. These values are represented by the black lines, while the red curve illustrates arterial pulsations. (Source: [11, p. 445])

Additionally, hydrostatic pressure is also influencing the pulmonary blood flow. Since the distance between the lowest and the highest point of the lungs is around 30 cm in an upright resting adult, there exists a 23 mmHg pressure difference. Hence, the pulmonary arterial pressure at the highest point in a standing person is 15 mmHg less and at the undermost point 8 mmHg than the pressure at the level of the heart. To explain these pressure differences, a zonal blood flow model of the lung is often used. The pulmonary capillaries are surrounded by gas and their structure is lacking support, because it is based only on a thin layer of cells, which line the alveoli. They are easily distended and collapsed by the blood pressure inside them and the alveolar air pressure outside respectively. Thus, the lung under normal and pathologic conditions is divided into three different zones depending on the blood flow in the pulmonary capillaries. [4, 11]

Figure 2.5 illustrates the dominating pressures - the pulmonary arteriole ($P_{pa}$) and venule pressure ($P_{pv}$) and the alveolar pressure ($P_A$) - and the resulting blood flow of the different zones.

**Zone I:** $P_A > P_{pa} > P_{pv}$. There exists no or nearly no blood flow in this zone. If at all, blood only flows in the apexes of the lungs, which belong to this zone, due to the gravitational dependence of the blood flow. This zone occurs in case the alveolar pressure is greater than the pulmonary arteriole and venule pressure. Thus, the capillaries are collapsed and therefore no gas exchange takes place in this region. [4, 13] Such a zone does not exist under normal conditions [4].

**Zone II:** $P_{pa} > P_A > P_{pv}$. In this zone the pulmonary arteriole pressure is greater than the alveolar pressure, which in turn is greater than the pulmonary venule pressure [4, 13]. So the alveolar pressure will be exceeded by the pulmonary arteriole pressure and intermittent blood flow occurs as there still is variability in blood pressure [4]. Therefore, the blood flow depends

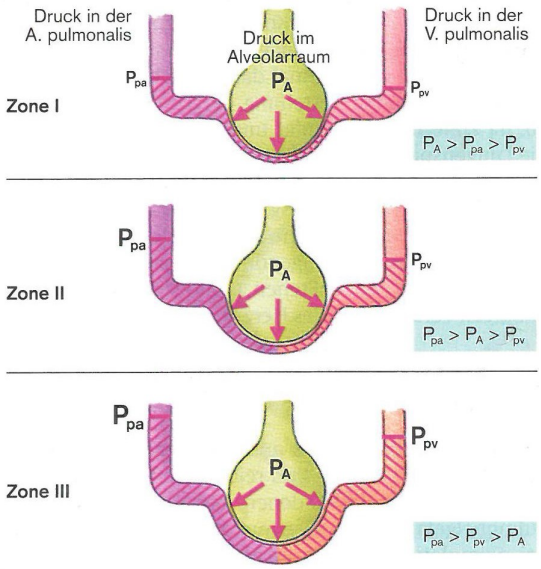


Figure 2.5: Here, the three different zones of the lungs are pictured. They differ in the values of the different pressures - pulmonary arteriole respectively venule pressure and the alveolar pressure. In zone I there is no blood flow, zone II exists of intermittent blood flow and in zone III all the pulmonary capillaries are open and therefore continuous blood flow occurs. (Source: [13, p. 183]

only on the difference of the alveolar pressure and the pulmonary arteriole pressure. It is nearly unaffected by the pulmonary venule pressure. [13] This special hemodynamical situation is often referred to as the Starling resistor phenomenon or the waterfall effect [4, 13] since the pulmonary capillaries serve as gates in order to control the blood flow [4].

Within this zone the blood flow increases from top to bottom since the arteriole pressure rises with decreasing lung level and the alveolar pressure stays the same throughout the region [4, 13].

**Zone III:** $P_{pa} > P_{pv} > P_A$. The characteristic of the third zone is that the pulmonary venule pressure is greater than the alveolar pressure [4, 13]. Hence, blood flow only depends on the difference of pulmonary arteriole and venule pressure which is the same in the whole area of zone III [13]. However, the blood flow still increases from top to bottom [4, 13], because the resistance decreases with increasing internal pressure [13]. So, all pulmonary capillaries are open and hence, there is only little resistance [13], which leads to continuous blood flow in this zone [4].

Altogether, it can be said that under normal lung conditions there does not exist zone I blood flow, which means under such circumstances there only occurs zone II and zone III blood flow in the lungs. The majority of the blood flow takes place in zone III, since all the capillaries are open. Thus, the majority of gas exchange occurs in this zone as well. Hence, zone III is the dominant zone in terms of blood flow. [4, 11]

### 2.1.3 Morphometry of the Pulmonary Circulation

There are different ways of classifying branches of tree-like structures such as the pulmonary arterial respectively the venous branching tree. The main difference is how the branches are grouped by their characteristics as for example by their length or diameter [4, 25]. Therefore, the main approaches are the Weibel generation classification and different kinds of Strahler ordering [4, 12, 25]. Here the different methods will be described with respect to the pulmonary arterial system.

#### Weibel Generation

The Weibel generation method numbers the vessels downwards beginning with the stem - in this case the MPA - as the first generation [4, 25]. Therefore, at each bifurcation the generation number is increased by 1 [4]. Thus, the terminal vessels have the highest counters of all other vessels in their branching tree [4]. The generation number of a considered vessel equals the number of bifurcations $n$ between the main pulmonary artery and this vessel plus 1 [4]. Hence it equals $n + 1$. But with raising asymmetry in the system the Weibel generation approach is not satisfactory, because this kind of classification neglects the fact that branches with similar characteristics (e.g. same radii, lengths, etc.) are spread over different generations [4, 25]. Conversely, a single generation also can include branches, such that they have a wide range of diameter [25]. An example for the Weibel generation approach is shown in Figure 2.6.

#### Strahler Ordering

Other methods of classification are grouping the branches together in orders. The Strahler ordering system is such kind of method and was originally developed to describe river systems, but is generally applicable to branching systems such as the pulmonary arterial tree [4, 25]. By this approach the most distal and thus terminal branches are declared to be of order 1 [4, 12, 25]. The order number of a branch, which results out of two branches of the same order number $n$, is increased by 1 and therefore equals $n+1$ [4, 12, 25]. If two daughter branches meet while having different ordering numbers, the order of the parent branch remains the same as the order of the daughter branch with the higher order [4, 12, 25]. As this numeration of branches continues till the stem, i.e. the main pulmonary artery, [4], the Strahler ordering system as well as its modified methods, for example the diameter-defined Strahler ordering, which will be described in the following paragraph, are upward approaches.

As there is no need of increasing the order at every bifurcation, this method is especially useful for systems where several small side branches join to one larger central branch [4, 25]. One major disadvantage of this ordering system is that there are large overlaps with respect to the diameters in sequential orders of the branches [4, 12]. Another difficulty is that all the branches of the same order are treated as parallel, without the possibility of using a series-parallel feature [12]. A small illustration of the Strahler ordering method is shown in Figure 2.6.

### Diameter-Defined Strahler Ordering

As mentioned before the Strahler ordering technique has some disadvantages especially in terms of applying it to the pulmonary arterial tree [4, 12]. Hence, the above mentioned Strahler ordering system was modified to the diameter-defined Strahler ordering technique [12], which will only be described roughly here. The terminal branches, i.e. the smallest non-capillary vessels in the pulmonary arterial tree, are declared as order 1, as in the Strahler ordering system [12]. The numeration of the further vessels is mainly following the same rules as described for the Strahler ordering systems, but the following further additional rule is introduced: Considering two daughter vessels, of which at least one is of order $n$ and the other of order less or equal to $n$, leads to order $n + 1$ of their parent vessel if and only if the diameter of the parent vessel is greater than a certain threshold. Otherwise, the order of the parent vessel remains $n$. [4, 12] Again a small example of this method is given in Figure 2.6.

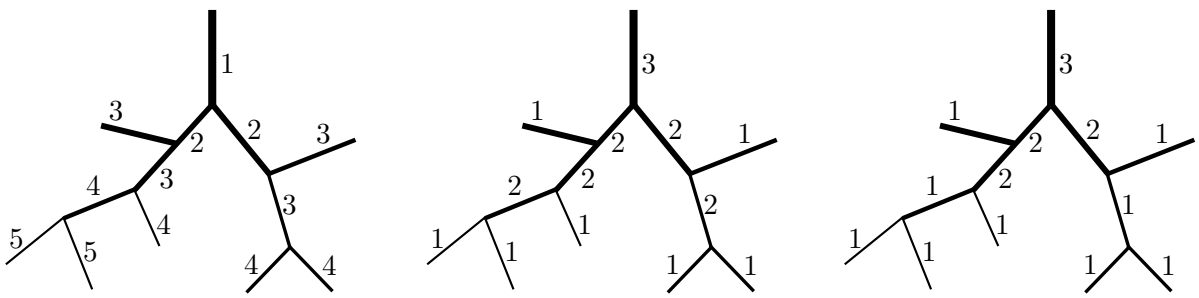


Figure 2.6: Illustration of the different approaches for grouping together vessels of a branching tree. Weibel's generation method is shown in the left graph. The branching tree in the middle represents the ordering technique of Strahler and the more special diameter-defined Strahler ordering approach is illustrated on the right side.

# 3 Mathematical Models of the Pulmonary Circulation

This chapter is about the main approaches of modelling the pulmonary circulation over the last decades. Such mathematical models of the lung function have the aim to support and improve the understanding of pulmonary health and changes of the arterial vasculature, which can lead to diseases. To be able to develop such models some simplifying assumptions have to be made. Some of these assumptions are related to the huge number of arterioles, venules and capillaries existing in the pulmonary circulation and also to the tapered form of the pulmonary trunk. However, a mathematical model is always a simplification of reality. Therefore, it does not desire to represent every single function and feature of the system one is looking at. [26]

The three main approaches, which will be described below, are the Windkessel model, a modelling method based on the Womersley equations and moreover the approach via the one-dimensional non-linear Navier-Stokes equations, which are commonly used to describe blood flow in vessels.

## 3.1 Windkessel Model

The fist approach, which will be considered, is the Windkessel modelling method. The Windkessel models are lumped parameter models, since the whole system is seen as one single compartment. They are mathematically described by linear ordinary differential equations of first order and explained in more detail in the following section. Furthermore, a small literature review of applications of this modelling technique and their simulation results is provided.

### 3.1.1 Mathematical Derivation and Formulation

One might be looking at the heart as a pump, which is connected with the organs by elastic tubes, specifically by arteries. Because of repeatedly turning on (systole) and off (diastole) this pump, there might be the problem that the organs are supplied with blood only intermittently. The elastic arteries help to overcome this problem. Hence, the elastic and therefore compliant arteries, which are linked to the heart, store some of the blood during systole to be able to release it during diastole. Thereby, the organs are supplied by blood flow in a more steady way. This reservoir-like storage of blood is described by the so called Windkessel model. [2]

The Windkessel model is commonly compared to an electrical circuit [12, 15]. The whole arterial tree is modelled as one compartment [20]. Therefore, it describes the variation of the pressure over time, but not in terms of spatial distribution [2, 20]. Hence, it is a lumped parameter model and one will not be able to look at for example wave transmission or wave reflections in the arteries with this model [2, 28]. There are different degrees of complexity of

the Windkessel model, the 2-element, 3-element and 4-element Windkessel models respectively. Windkessel models are models which describe the pulmonary circulation in terms of peripheral resistance $R_p$ and arterial compliance $C_a$ (2-element Windkessel model) [2, 20, 24, 28] and additionally in terms of characteristic impedance $Z_c$ (3-element Windkessel model)[2, 14, 15, 20, 24, 28] and inertance $L$ (4-element Windkessel model) [20, 28]. Hence, the parameters are limited [15, 28] and even more have a physiological meaning [15, 24, 28].

### 2-element Windkessel Model

As already mentioned, the 2-element Windkessel model consists of 2 components: the peripheral resistance and the arterial compliance. $R_p$ is the resistance the blood has to overcome to be able to leave the compartment [20]. Since Poiseuille's law states that the resistance of a vessel is inverse proportional to its diameter to the power of 4, $R_p$ is dominated by the resistance of small arteries and arterioles [24, 28] and can be calculated by

$$R_p = \frac{P_{MPA,mean} - P_\infty}{CO},$$

where $P_{MPA,mean}$ is the mean pulmonary artery pressure and CO the cardiac output of the pulmonary circulation [24, 28]. $P_\infty$ is a constant, which represents a base pressure in the system [20]. It can also be seen as the pressure under which the flow is running dry in the mircocirulation [20]. For simplification it is set to 0 here [20]. Hence, the peripheral resistance can be approximated by

$$R_p = \frac{P_{MPA,mean}}{CO}. \tag{3.1}$$

The arterial compliance represents the elasticity of the arterial network [15, 20, 28]. Therefore, it also stands for the capacity of the arteries and arterioles together [24] and can be gained by adding the compliances of all arterial vessels in the network [28]. $C_a$, as the total arterial compliance, is defined as the ratio of the change in volume $\Delta V$ and the resulting change of pressure $\Delta p$ [20, 24, 28]. Hence, $C_a$, seen as a constant, is given by [20, 24, 28]

$$C_a = \frac{\Delta V}{\Delta p}.$$

Also described in [20], the main pulmonary arterial pressure and thus the Windkessel pressure have to fulfil the following differential equation

$$\dot{p}(t) + \frac{1}{R_p C_a} p(t) = \frac{1}{C_a} q(t), \tag{3.2}$$

where $q(t)$ is the blood flow. If additionally,

$$p(0) = P_0 \tag{3.3}$$

is given as an initial value, $p(t)$ is the solution of the initial value problem consisting of equations

(3.2) and (3.3). If the pulmonary valve is closed, there is no blood flow during that time of closure. Hence, $q(t) = 0$ during diastole. Therefore, the initial value problem simplifies to [20]

$$\dot{p}(t) = -\frac{1}{R_p C_a} p(t), \quad p(T) = P_0, \tag{3.4}$$

for $t \in [t_d, T]$. Here, $T$ stands for the duration of one heart beat and $t_d$ is the point of time of the beginning of the diastole. Since pressure and flow are assumed to be periodic, $p(T)$ equals $p(0)$ and thus $P_0$ equals $p(T)$ [20]. The solution of the initial value problem (3.4) for the pressure during diastole $p_{dias}(t)$ is given by [20, 28]

$$p_{dias}(t) = P_0 e^{\frac{T-t}{R_p C_a}}, \tag{3.5}$$

for $t \in [t_d, T]$. Consequently, the Windkessel model predicts that the aortic pressure decreases with constant $RC$-time during diastole [2, 20, 24, 28].

The Windkessel model is commonly seen as an electrical circuit analogue, which is illustrated in Figure 3.1, as previously mentioned. Thus, the pressure $p(t)$ correlates with the total voltage and the flow $q(t)$ correlates with the total current in an electrical circuit [20].

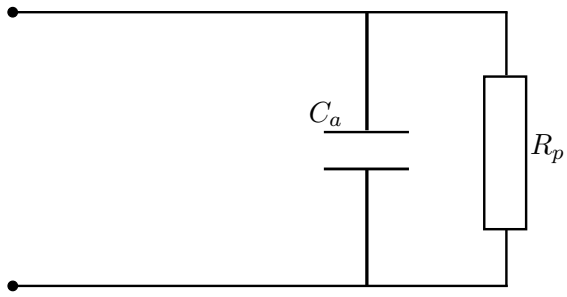


Figure 3.1: Illustration of the electrical circuit analogue of the 2-element Windkessel model with peripheral resistance $R_p$ and arterial compliance $C_a$ as components.

### 3-element Windkessel Model

Although the 2-element Windkessel model predicts the behaviour of blood pressure $p(t)$ during diastole quite good, it has some shortcomings during systole [20, 28]. Thus, a third element for the Windkessel model is added, namely the characteristic impedance $Z_c$. The characteristic impedance describes the relation of pressure and flow without reflections [20] and can be calculated by

$$Z_c = \frac{c\rho}{A},$$

with $c$ as pulse wave velocity, $\rho$ as blood density and $A$ as the cross-sectional area [2, 24, 28]. Furthermore, $Z_c$ connects aspects of wave propagation of the arterial system with lumped Windkessel theory [2, 20, 28]. $Z_c$ is seen as an additional resistor in respect of the blood flow in the proximal pulmonary artery during systole [20, 24, 28]. Hence, the modelling equation is

modified and given by

$$p(t) = Z_c q(t) + p_{WK}(t), \tag{3.6}$$

where $p_{WK}(t)$ is the solution of (3.2) and of (3.2)-(3.3), if an initial value is given [20]. As $q(t) = 0$ during diastole, there is no difference between the 3-element and the 2-element Windkessel models during this time [20, 28] and therefore equation (3.4) with solution (3.5) holds true [20]. The electrical circuit illustration of the 3-element Windkessel model is shown in Figure 3.2.

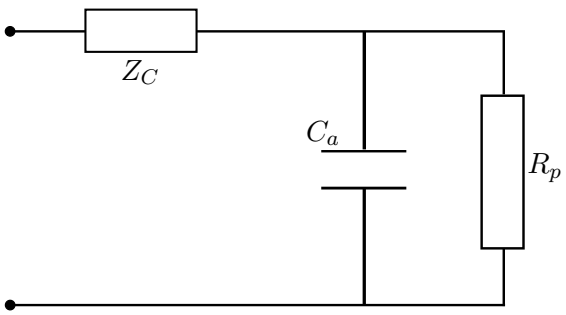


Figure 3.2: Illustration of the electrical circuit analogue of the 3-element Windkessel model with peripheral resistance $R_p$, arterial compliance $C_a$ and characterisitic impedance $Z_c$ as components.

#### 4-element Windkessel Model

As inertance $L$ is restraining every kind of acceleration of the blood, the 4-element Windkessel model was established. The fourth component, namely inertance $L$, stands for the proportionality of pressure, causing acceleration, and the resulting change of the flow $\dot{q}(t)$. [20]

There exist two different approaches of modelling the 4-element Windkessel. $Z_c$ and $L$ can be connected either in parallel or in series. Exemplary only the equation for the serial model is provided here. It is given by

$$p(t) = L\dot{q}(t) + Z_c q(t) + p_{WK}(t), \tag{3.7}$$

where $p_{WK}(t)$ again is the solution of (3.2). If there is also an initial value $p(0) = P_0$ given, $p_{WK}(t)$ is the solution of the initial value problem (3.2)-(3.3). Again, like the 3-element Windkessel model, the 4-element Windkessel model only differs from the 2-element Windkessel model during systole. During diastole all the Windkessel models coincide. [20]

The electrical circuit analogue of the 4-element Windkessel model in series is pictured in Figure 3.3.

### 3.1.2 Literature Review of Applications of the Windkessel Model in the Pulmonary Circulation

The Windkessel approach of modelling the pulmonary circulation is straightforward also in terms of interpretation [2] as its parameters have physiological meanings [15, 24, 28]. The compliance

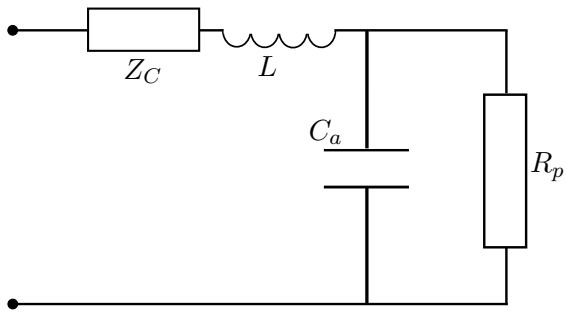


Figure 3.3: Illustration of the electrical circuit analogue of the 4-element Windkessel model with peripheral resistance $R_p$, arteraial compliance $C_a$, characteristic impedance $Z_c$ and inertance $L$ as components.

of the arterial tree is in charge of storing the ejected blood which is done by dilation of the vessels during systole [20, 24]. Hence, it is also responsible for constriction of the vessels during diastole when the pressure is decreasing [20, 24]. Therefore, blood is released during diastole, which leads to continuous blood flow during the cardiac cycle [20, 24]. Moreover, the compliant arteries are damping the pressure as well [24]. Thus, the variation of pressure during diastole in the main pulmonary artery is not as large as in the RV [24]. Hence, as the parameters of the models can be interpreted in physiological context and since the model is not very complex and thereby easy to handle, the Windkessel model is commonly used for modelling the pulmonary circulation. Hereafter, only a small selection of applications of this kind of modelling approach for the pulmonary circulation in literature is given.

**Bouwmeester et al. [3]**

The aim of the study of Bouwmesster et al. [3] was to decompose the pulmonary vascular resistance (PVR) into the resistances of the arterial, venous and microcirculatory parts of the pulmonary vascular bed by a reservoir-wave model. PVR correlates mean pressure $\bar{P}$ and mean flow $\bar{Q}$ via PVR $= \frac{\bar{P}}{\bar{Q}}$. Hence, PVR can be seen as measurement of resistance to the blood flow in the lungs.

The reservoir-wave model was constructed such that the resistance of the pulmonary arteries was separated from the remaining arterial reservoir - standing for the small vessels. Hence, this part of the pulmonary circulation was modelled by a 2-element Windkessel model. The venous part was separated in the same way and thus was also represented by a 2-element Windkessel model. The arterial as well as the venous reservoir are modelled by pulmonary arterial/venous resistance $(R_{PA}, R_{PV})$, compliance $(C_{PA}, C_{PV})$ and corresponding constant asymptotic pressure $(P_{\infty-PA}, P_{\infty-PV})$. Furthermore, the two reservoirs were linked together by the microcirculatory resistance. Figure 3.4 shows the electrical circuit analogue of the entire model. Additionally, the modelling equations are given by

$$\frac{\mathrm{d}P_{res-PA}(t)}{\mathrm{d}t} = \frac{Q_{in-PA}(t) - Q_{out-PA}(t)}{C_{PA}} \quad \text{with} \quad Q_{out-PA} = \frac{P_{res-PA}(t) - P_{\infty-PA}}{R_{PA}} \tag{3.8}$$

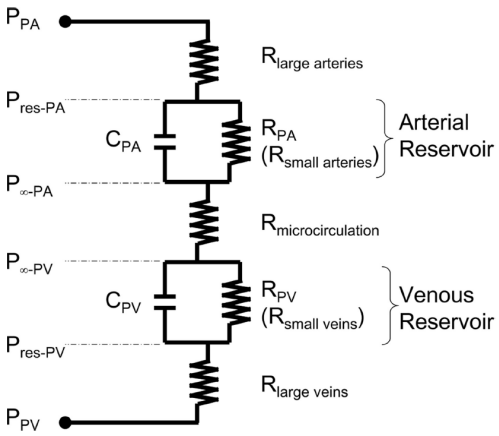


Figure 3.4: Schematic representation of the reservoir-wave model as an electrical circuit analogue including the whole pulmonary circulation by Bouwmeester et al. [3]. (Source: [3, p. 1839])

for the arterial part and by

$$\frac{\mathrm{d}P_{res-PV}(t)}{\mathrm{d}t} = \frac{Q_{in-PV}(t) - Q_{out-PV}(t)}{C_{PV}} \quad \text{with} \quad Q_{in-PV} = \frac{P_{\infty-PV} - P_{res-PV}(t)}{R_{PV}} \tag{3.9}$$

for the venous part. For the arterial reservoir the inflow was measured and used as an input for modelling the outflow, given in (3.8). Contrariwise, measured outflow of the pulmonary vascular bed was used as input for the venous reservoir and hence inflow was modelled by equation (3.9). For adequate parameters of the reservoirs a fitting algorithm using "fminsearch" in MATLAB was used with arbitrary initial values. The PVR was then calculated by

$$\text{PVR} = \frac{\text{mean}P_{PA} - \text{mean}P_{PV}}{\text{mean}Q_{PA}}.$$

Bouwmeester et al. applied this reservoir-model and PVR estimations to pressure and flow measurements of 11 dogs to investigate differences in PVR composition of arterial, venous and microcirculatory resistances in terms of acute hypoxia ventilation, nitric oxide inhalation as well as volume load and positive end-expiratory pressure. From their simulation results, illustrated in Figure 3.5, they concluded that total PVR and small artery resistance is increasing with hypoxia and contrarily decreasing with nitric oxide ventilation. Additionally, resistance in the veins is also increasing with hypoxia. Furthermore, it can be seen that volume loading leads to a decrease of each resistance component and thus to a decrease of total PVR. They also observed that with positive end-expiratory pressure only the microcirculatory resistance is increasing and that it does not significantly effect the other components.

Overall, Bouwmeester et al. deduced that in respect to hypoxia and ventilation with nitric oxide the small arteries are most responsible for changes in resistance and that volume loading affects each PVR component while positive end-expiratory pressure only influences the microcirulatory resistance.

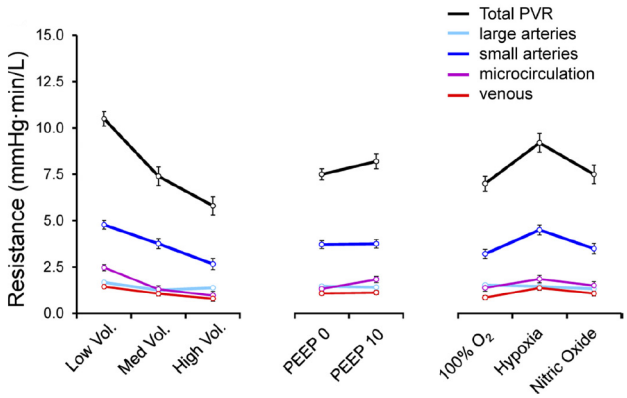


Figure 3.5: Illustration of the different PVR components grouped into the investigated types of volume load, positive end-expiratory pressure and ventilation by Bouwmeester et al. [3]. The data points correspond to the least-squared mean values $\pm SD$ of each component of PVR. (Source: [3, p. 1843])

### Lungu et al. [18]

The aim of Lungu et al. [18] is to find diagnostic parameters in respect to the Windkessel model by using non-invasive MRI flow measurements. These flow measurements were used as input for a 3-element Windkessel model. The parameters of this Windkessel model are $R_C, R_d$ and $C$. Instead of the characteristic impedance $Z_c$, they used $R_C$, a free parameter serving as a capacitor's proximal resistance. $R_d$ stands for the peripheral resistance and $C$ for the compliance. Furthermore, PVR$=\frac{\text{mean}P}{\text{mean}Q}$ was assumed to be equal to $R_C + R_d$. Figure 3.6 shows the electrical circuit analogue of the Windkessel model considered, which is described by the following equations

$$Q_0(t) = C\frac{\mathrm{d}P_C}{\mathrm{d}t} + \frac{P_C(t)}{R_d}, \tag{3.10}$$

$$P_0(t) = P_C(t) + R_C \cdot Q_0(t). \tag{3.11}$$

Here, $P_C$ is the capacitor's pressure drop. At the domain inlet the measured flows and pressures are given by $Q_0(t)$ and $P_0(t)$.

For determining the values of $R_C$, $C$, and $R_d$ an optimisation algorithm was applied to the model. This optimisation algorithm is based on minimising the absolute error of the simulated pressure and the measured pressure.

Measurements of pressure and flow were performed in 35 patients, which were divided into four distinct groups. The first group consisted of 8 healthy volunteers. The other groups were patients suffering from severe pulmonary hypertension (PH) ($n = 14$, PVR $\geq 4$ mmHg s/ml) or suffering from mild PH ($n = 9$, PVR $\leq 4$ mmHg s/ml) and patients with suspected PH, but a measured pressure lower than 25 mmHg (NoPH, $n = 4$).

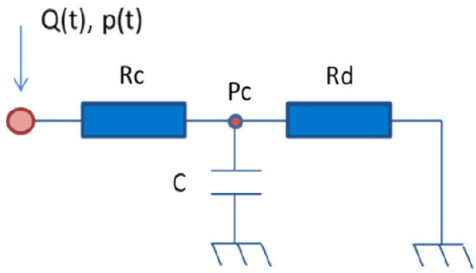


Figure 3.6: Illustration of the 3-element Windkessel model as an electrical circuit analogue used by Lungu et al. [18]. Instead of $Z_c$ for the characteristic impedande, $R_C$, serving as the capacitor's proximal resistance, is used. (Source: [18, p. 2942])

Their simulation results of the Windkessel model (see Figure 3.7) indicate that $R_d$ is increasing significantly with increasing disease stage. Contrariwise, $C$ is decreasing related to disease severity. The mean compliance ranges from 4.19 ml/mmHg in the healthy group to 0.78 ml/mmHg in the patients with severe PH. $R_d$ takes the value of 0.24 mmHg s/ml in the NoPH group, 0.57 mmHg s/ml in the mild PH group and 1.2 mmHg s/ml in the severe PH group. The total resistance $R_{total}$ was also found to increase with disease stage, but not significantly. Furthermore, the relation of $R_d$ to $R_{total}$ showed only significant differences between the healthy persons and the other groups, but not among the other groups. Additionally, Lungu et al. detected that the parameter $R_C$ is not significantly varying among the different groups of patients. They also compared their results with the results of Lankhaar et al. [15] and identified comparable results for average values of $C$ and $R_d$. Overall, Lungu et al. concluded that especially the peripheral resistance $R_d$ might be used as a differentiation criteria between patients suffering from PH and healthy persons or NoPH patients in respect to non-invasive MRI measurements.

**Lankhaar et al. [15]**

Lankhaar et al. [15] used a 3-element Windkessel model for investigating differences in the Windkessel parameters $R_p$, $C$ and $Z_c$ of three separate patient groups. Two of the three examined patient groups were patients with no pulmonary hypertension (NONPH) (n=10) and on the other hand patients with idiopathic pulmonary arterial hypertension (IPAH) (n=9). The third group was formed out of patients suffering from chronic thromboembolic pulmonary hypertension (CTEPH) (n=10). For these patients pressure and flow were obtained by invasive measurements and via MRI velocity quantification respectively. The so recorded flow served as input to the model. The three parameters for the 3-element Windkessel model were obtained from the recorded data via an energy balance method. The compliance gained by this method is denoted by $C_{EBM}$. Furthermore, the compliance was additionally estimated with the help of the pulse pressure method ($C_{PPM}$) as well as by the ratio of stroke volume to pulse pressure ($C_{SVPP}$). In Figure 3.8 all the estimated parameters are illustrated for each patient group.

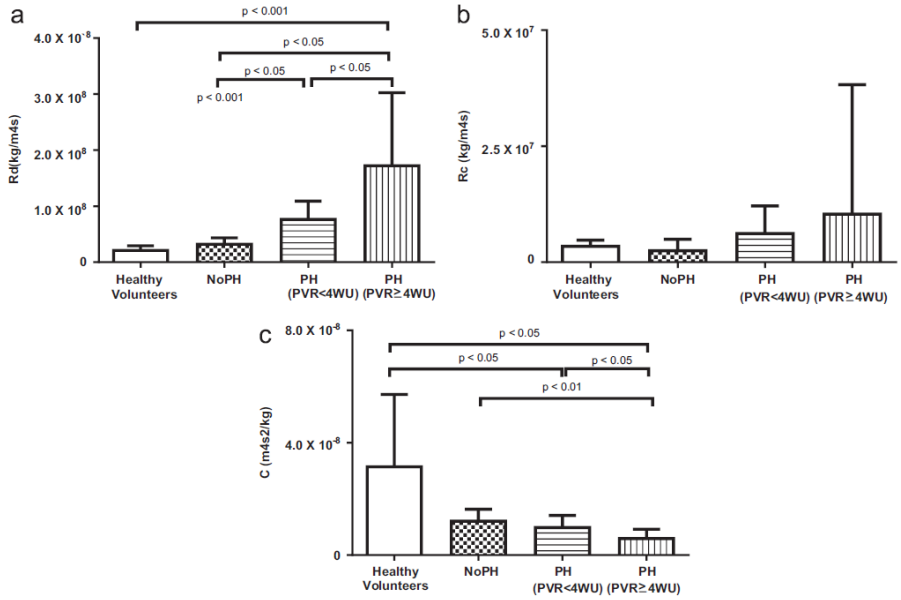


Figure 3.7: Simulation resutls by Lungu et al. [18] in terms of the paramters of the 3-element Windkessel model. The results show that the distal resistance $R_d$ is increasing with increasing disease stage and that compliance $C$ acts contrarily. Furthermore, characteristic resistance $R_C$ is not significantly differing among the patient groups. (Source: [18, p. 2945])

They concluded that the peripheral resistance and the characteristic impedance were significantly lower in the NONPH group than in the other two groups. Additionally, the arterial compliance was significantly higher for the NONPH patients than for the others. Furthermore, they found out that the IPAH and CTEPH groups only differed significantly in terms of peripheral resistance and characteristic impedance, but not in terms of arterial compliance. It was also deduced, that the significance levels with respect to compliance did not depend on the estimation method of this parameter among the three patient groups. Moreover, they observed that the relationship of $R_p$ and $C$ is inverse, independent of the considered types of diseases, which is shown in Figure 3.9. This also leads to a constant $RC$-time of $\tau = 0.75$ s for $C = C_{EBM}$ among all the patients unrelated to their pulmonary hypertension group. In general this $RC$-time is responsible for the typical exponential pressure decay during diastole, as given in equation (3.5).

Altogether, Lankhaar et al. concluded that the three Windkessel parameters give a possibility to distinguish distinct patient groups such as patients suffering from CTEPH, IPAH or NONPH and that there exists a remarkable inverse relationship between resistance and compliance among all patients included in this study.

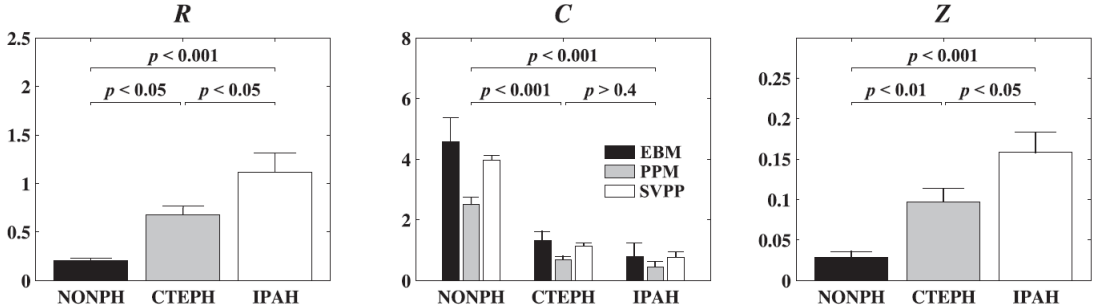


Figure 3.8: Illustration of the results of the parameter estimations of the 3-element Windkessel model for three distinguishable patient groups (NONPH, CTEPH and IPAH) by Lankhaar et al. [15]. Here, mean values for $R_p$ and $Z_c$ are given in mmHg s/ml and the mean values for the three different estimations (energy balance method (EBM), pulse pressure method (PPM) and the ratio of stroke volume to pulse pressure (SVPP)) of $C$ in ml/mmHg. (Source: [15, p. H1734])

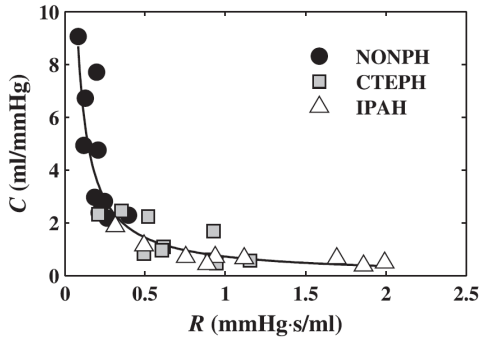


Figure 3.9: Graphical representation by Lankhaar et al. [15] of the relationship of the estimated values of the parameters $R_p$ and $C_{EBM}$ of a 3-element Windkessel model among all three patient groups (NONPH,CTEPH and IPAH). (Source: [15, p. H1734])

### Lankhaar [14]

Lankhaar [14] developed a further Windkessel model in the course of his PhD thesis. The aim of this model was to detect the mechanisms by which the relationship between total resistance and total compliance of the pulmonary vascular bed stays inverse. This was uncovered in the previous mentioned study of Lankhaar et al. [15]. In this context, he furthermore wanted to investigate the effects of occlusion on resistance and compliance throughout the pulmonary arterial vascular bed. Hence, a branching tree model based on a 2-element Windkessel model with parameters $R$ and $C$ for the arterial side of the pulmonary vascular bed was developed. In the entire vascular bed considered, the resistances and compliances were varying with segmental order of the vessels. The model was composed of three sections: the entrance section, the middle section and the terminating section. The entrance section was followed by $N-1$ generations. Each of these generations of order $k$ were represented by $n_k$ middle sections. Subsequently the branching tree model is completed by $n_N$ terminating vessels. The electrical circuit analogue of

these three sections of the model are exemplary depicted in Figure 3.10. For simplification all segments of the same order were assumed to be equal.

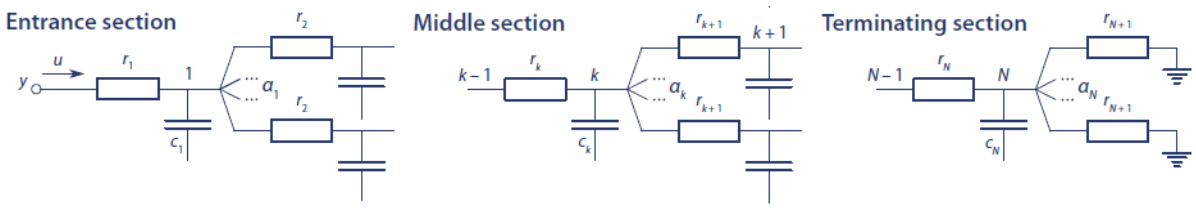


Figure 3.10: Schematic representantion of the entrance, middel and terminating sections of the $RC$-tree model developed by Lankhaar[14]. Here, $y$ is the pressure and hence the output and $u$ is the input flow of the model. Moreover, $\alpha_k$ represents the number of daughters of the parent vessel $k$. Furthermore, all middle sections of order $k$ are handled as parallel and thus equal. (Source: [14, p. 138])

Furthermore, the flow $u$ served as input at the entrance and the pressure $y$ at the entrance was the output of the model. The mathematical formulation of the entire model is given by

$$\dot{\boldsymbol{x}} = A \cdot \boldsymbol{x} + \begin{pmatrix} \frac{1}{c_1} \\ 0 \\ \vdots \\ 0 \end{pmatrix} \cdot u \tag{3.12}$$

$$y = \boldsymbol{x}(1) + r_1 \cdot u \tag{3.13}$$

with

$$A = \begin{pmatrix} -\frac{\alpha_1}{\tau_{21}} & \frac{\alpha_1}{\tau_{21}} & 0 & & & & \\ \frac{1}{\tau_2} & -\left(\frac{1}{\tau_2} + \frac{\alpha_2}{\tau_{32}}\right) & \frac{\alpha_2}{\tau_{32}} & 0 & & & \\ & & \ddots & & & & \\ & 0 & \frac{1}{\tau_k} & -\left(\frac{1}{\tau_k} + \frac{\alpha_k}{\tau_{k+1,k}}\right) & \frac{\alpha_k}{\tau_{k+1,k}} & 0 & \\ & & & \ddots & & & \\ & & & 0 & \frac{1}{\tau_{N-1}} & -\left(\frac{1}{\tau_{N-1}} + \frac{\alpha_{N-1}}{\tau_{N,N-1}}\right) & \frac{\alpha_{N-1}}{\tau_{N,N-1}} \\ & & & & 0 & \frac{1}{\tau_N} & -\left(\frac{1}{\tau_N} + \frac{\alpha_N}{\tau_{N+1,N}}\right) \end{pmatrix}.$$

Here, $\alpha_k,\ k \in \{1, ..., N\}$ is the number of daughters of order $k$. $\tau_{ij}$ is defined by $\tau_{ij} = r_i c_j$ for all $1 \leq i \neq j \leq N$ and $\tau_i = r_i c_i$ $(= \tau_{ij}$ for $i = j)$. Occlusion and loss of vessels respectively was simulated by reduction of $\alpha_k$, which causes changes in the total resistances and compliances of orders $j > k$. Moreover, compliance was taken into account in two ways for simulation of occlusion. First of all, compliance was considered to be constant and was thus calculated by

$$C = \frac{3V}{E} \frac{\left(\frac{a}{h} + 1\right)^2}{2\frac{a}{h} + 1}, \tag{3.14}$$

where $E$ is Young's modulus, $h$ the vessel wall thickness, $a$ the radius of the vessel and $V$ the corresponding volume. On the other hand, pressure dependent compliance was assumed to be inversely proportional to the pressure in the considered vessel and hence

$$C(p) = \frac{\beta}{p} \tag{3.15}$$

with $\beta$ being a constant. But for implementation this pressure-dependent compliance was assumed to be equal to its average for a given mean pressure.

As already mentioned the flow at the entrance was used as the input condition of the model. For the simulation study Lankhaar used a triangular flow as input. This triangular flow is peaking at one third of the systole. Diastole starts at one third of the heart beat period and during diastole flow is set to zero. Furthermore, heart rate period was set to 70 beats per minute and stroke volume was assumed to be 80 ml. In regard of the stability of the simulation step size was set to $1 \cdot 10^{-5}$ s and for maintaining a periodic output more than 10 cardiac cycles were simulated. Moreover, the branching tree model was considered to be composed out of 17 generations and occlusion was simulated in generations 5 to 17.

The simulation results showed that the developed model tends to have the same input impedance as a single 2-element Windkessel model. Additionally, the calculated pressure waveform of the branching tree model is identical to the pressure waveform calculated by a corresponding 2-element Windkessel model. The total resistance and compliance without taking occlusion into account were 0.18 mmHg s/ml and 3.5 ml/mmHg respectively. Hence, the default $RC$-time takes the value of 0.63 s. The results for the simulation of occlusion indicated that resistance is not increasing evenly with increase of occlusion. Resistance only increases notably when most of the vascular bed (85%) is closed. Constant compliance is increasing marginally with closure of only small vessels and decreasing with the amount of occlusion of larger vessels. Unfortunately, this behaviour of constant compliance leads to unrealistic results of the $RC$-time. On the other hand, the variation of pressure-dependent compliance in terms of occlusion simulation was also investigated. For pressure-dependent compliance it was concluded that the $RC$-time varies to a much lesser extent and is similar to measured values. This is due to the more realistic decrease of pressure-dependent compliance for occlusion.

Overall, by using the $RC$-tree model for the pulmonary circulation Lankhaar came to the conclusion that the previously observed inverse relationship between pulmonary resistance and compliance [15] can be explained by a combination of pressure-dependent compliance and the distribution of resistance and compliance throughout the pulmonary vascular bed.

Table 3.1 gives a short overview of the literature review of the studies of Bouwmeester et al. [3], Lungu et al. [18], Lankhaar et al. [15] and Lankhaar [14], given before.

Table 3.1: Overview of the literature review of studies which used the Windkessel modelling approach for modelling and simulation of the pulmonary circulation.

| | **Bouwmeester et al. [3]** | **Lungu et al. [18]** | **Lankhaar et al. [15]** | **Lankhaar [14]** |
|---|---|---|---|---|
| species | dog | human<br>*4 groups:* healthy, no PH, mild PH, severe PH | human<br>*3 groups:* NONPH, IPAH, CTEPH | human |
| modelled geometry | MPA, lumped pulmonary arterial bed, microcirculation, lumped venous bed, larger pulmonary veins<br><br>different forms of ventilation | lumped pulmonary arterial bed | lumped pulmonary arterial bed | 17 generations via $RC$-tree model (entrance, middle and terminating section)<br><br>simulation of occlusion |
| modelling equations | reservoir-wave model; arterial & venous reservoirs modelled by 2-element Windkessel model, given by equations (3.8) & (3.9) | 3-element Windkessel model $(R_C, R_d, C)$ given by equations (3.10) & (3.11) | 3-element WK model $(Z, R, C)$ | branching tree model based on 2-element Windkessel model (see equations (3.12) & (3.13)) |

Table 3.1 – continued from previous page

| | **Bouwmeester et al. [3]** | **Lungu et al. [18]** | **Lankhaar et al. [15]** | **Lankhaar [14]** |
|---|---|---|---|---|
| parameter estimations | fitting algorithm including "fminsearch" in MATLAB<br>arbitrary initial values | optimisation algorithm based on minimising absolute error between computed and measured pressure | $R, C, Z$ estimated via energy balance method;<br>$C$ additionally estimated via pulse pressure method and via the ratio of stroke volume to pulse pressure | parameters taken from literature<br>$C$ considered to be constant (3.14) as well as pressure-dependent (3.15) |
| initial condition | measured $P_0$ | measured $P_0$ (non-invasive) | measured $P_0$ | arbitrary $P_0$ |
| input to model | *arterial reservoir:* measured inflow<br>*venous reservoir:* measured outflow | measured flow via MRI | measured flow via MRI | triangular flow |

Table 3.1 – continued from previous page

| | **Bouwmeester et al. [3]** | **Lungu et al. [18]** | **Lankhaar et al. [15]** | **Lankhaar [14]** |
|---|---|---|---|---|
| results | total PVR and small-artery resistance increase with hypoxia and decrease with nitric oxide ventilation and volume loading<br><br>venous resistance increases with hypoxia and decreases with volume loading | $R_d$: increasing with disease stage<br>$C$: decreasing with severity<br>$R_C$: not significantly different among the patient groups<br><br>$R_d$ possible differentiable criteria between patient groups | $C$ significantly higher, $R, Z$ significantly lower for NONPH than for IPAH and CTEPH<br><br>IPAH and CTEPH differed in terms of $R$ and $Z$<br><br>Inverse relation between $R$ and $C$ and hence constant $RC$-time ($\tau = 0.75$ s) among all patients | $R$: not increasing evenly with occlusion, notably increasing when 85% of vascular bed is closed<br>*constant* $C$: variation with occlusion leads to unrealistic results<br>*pressure-dependent* $C$: similar to measured values also during occlusion, $RC$-time more realistic<br><br>total $RC$-time equals 0.63 s<br><br>inverse relationship observed in [15] can be explained by considering pressure-dependent $C$ and distribution of $R$ and $C$ among entire vascular bed |

## 3.2 One-Dimensional Linearised Navier-Stokes Equations (Womersley Equations)

Another approach of modelling the pulmonary circulation is by considering the motion of blood as the motion of a Newtonian fluid in a tube with constant length [10, 29, 30]. This motion is mathematically described by the Navier-Stokes equations and will be derivated in the following discourse based on [10, 27, 29, 30], if not stated differently. The aim of this discourse is to eventually obtain the Womersely equations and their corresponding solutions. Furthermore, a short overview of applications of this modelling method of the pulmonary circulation in literature is given.

### 3.2.1 Mathematical Derivation and Formulation

The following derivation is based on assuming blood flow as a Newtonian fluid flow in a tube with constant length. For considering blood as a Newtonian fluid and for validity of the Navier-Stokes equations some assumptions have to be made. First of all, it is assumed that the dynamic viscosity $\mu$ and the density $\rho$ of the blood are constant in space and time. Considering constant density is equivalent to regarding an incompressible fluid. Secondly, the shear stress and the velocity gradient are linearly correlated. Hence, blood is referred to as a Newtonian fluid. Furthermore, gravitation and other external forces are neglected. It is reasonable to consider blood as an incompressible Newtonian fluid, as the effects of its non-Newtonian properties on the pulse transmission in large vessels are only little compared to its effects in microcirculation, where they are more significant. Since the vessels are modelled as a segment of a uniform elastic tube with circular cross-section $A$ and constant length $L$, a further assumption is that the vessels are circular with an axisymmetric flow field. Because of this assumed axisymmetric flow field, all variables and the following equations depending on the cylindrical coordinate system are independent of the angular velocity component and of derivatives in direction of the angle $\theta$. Furthermore, to be able to describe the flow of a viscous fluid, a non-slip boundary condition at the wall is necessary. This boundary condition implies that the fluid, which is directly in contact with the tube wall, has the same velocity as the wall. The Navier-Stokes equations (see equations (3.16) - (3.18)) can be written in terms of a cylindrical coordinate system as

$$\frac{\partial u}{\partial x} + \frac{\partial v}{\partial r} + \frac{v}{r} = 0, \tag{3.16}$$

$$\rho\left(\frac{\partial u}{\partial t} + u\frac{\partial u}{\partial x} + v\frac{\partial u}{\partial r}\right) + \frac{\partial p}{\partial x} = \mu\left(\frac{\partial^2 u}{\partial x^2} + \frac{\partial^2 u}{\partial r^2} + \frac{1}{r}\frac{\partial u}{\partial r}\right), \tag{3.17}$$

$$\rho\left(\frac{\partial v}{\partial t} + u\frac{\partial v}{\partial x} + v\frac{\partial v}{\partial r}\right) + \frac{\partial p}{\partial r} = \mu\left(\frac{\partial^2 v}{\partial x^2} + \frac{\partial^2 v}{\partial r^2} + \frac{1}{r}\frac{\partial v}{\partial r} - \frac{v}{r^2}\right), \tag{3.18}$$

with the following variables and parameters:

| | |
|---|---|
| $p$ | pressure, |
| $u$ | axial velocity, |
| $v$ | radial velocity, |
| $x$ | axial coordinate, |
| $r$ | radial coordinate, |
| $t$ | time, |
| $\rho$ | density of the fluid, |
| $\mu$ | dynamic viscosity of the fluid. |

Equation (3.16) is describing the conservation of mass and is also known as the continuity equation.

Since uniform elastic tubes are considered as basic elements for modelling the pulmonary vessels, also wave motion along the vessels has to be taken into account. Therefore, the wave speed $c_0$ is approximated by the Moens-Korteweg formula

$$c_0 = \sqrt{\frac{Eh}{\rho d(1-\sigma^2)}}, \tag{3.19}$$

where $E$ stands for Young's modulus for the vessel wall, $h$ for the vessel wall thickness, $\rho$ again is the density of the fluid, $d$ represents the diameter of the vessel and $\sigma$ is the Poisson ratio. But this approximation only holds if assuming that the viscosity is negligible and that wall thickness compared to the vessel radius is small. Under further presuppositions the governing equations (3.16)-(3.18) can be simplified. For simplification, it has to be assumed that on the one hand the wave length $\lambda$ compared to the vessel radius $r_0$ and on the other hand the wave velocity $c_0$ compared to the average flow velocity $\bar{u}$ are large.

In respect of further reduction of the Navier-Stokes equations (3.17) and (3.18), transformation into a dimensionless form of these equations and utilisation of the before mentioned assumptions is applied, as described in more detail in [10, 27]. Thus, the last two equations of the Navier-Stokes equations simplify to

$$\rho\frac{\partial u}{\partial t} + \frac{\partial p}{\partial x} = \mu\left(\frac{\partial^2 u}{\partial r^2} + \frac{1}{r}\frac{\partial u}{\partial r}\right), \tag{3.20}$$

$$\frac{\partial p}{\partial r} = 0. \tag{3.21}$$

Equation (3.21) means that the pressure is independent of $r$ and hence $p = p(x,t)$. Since the system of equations ((3.16), (3.20), (3.21)) is still a two-dimensional space system, namely depending on $x$ and $r$, its dependence on $r$ is eliminated by integration over the cross-sectional area [10, 27, 30]. Thus, the flow velocity is changed to the flow rate $q = q(x,t)$. Given that a distensible tube is considered, the radius of the tube $a$ is not constant over time and space, hence, $a = a(x,t)$. Integration of equations (3.16) and (3.20) over the cross-sectional area leads

to

$$2\pi \int_0^a r\frac{\partial u}{\partial x}\,\mathrm{d}r + 2\pi \int_0^a r\left(\frac{\partial v}{\partial r} + \frac{v}{r}\right)\,\mathrm{d}r = 0, \tag{3.22}$$

$$2\pi\rho \int_0^a r\frac{\partial u}{\partial t}\,\mathrm{d}r + 2\pi \int_0^a r\frac{\partial p}{\partial x}\,\mathrm{d}r = 2\pi\mu \int_0^a r\left(\frac{\partial^2 u}{\partial r^2} + \frac{1}{r}\frac{\partial u}{\partial r}\right)\,\mathrm{d}r. \tag{3.23}$$

To express equations (3.22) and (3.23) in respect to pressure $p$, flow $q$, cross-sectional area $A$ and shear stress $\tau_\omega$ these equations are transformed under further assumptions as described hereinafter.

In addition to the already mentioned no-slip boundary condition $u(a) = 0$, also a "matching" boundary condition $v(a,t) = \frac{\partial a}{\partial t}$ has to be taken into account. This equality means, that at the tube wall the radial velocity $v$ is the same as the rate of change of the tube radius $a$. This boundary condition is necessary for preserving the mechanism of wave propagation. Applying this equality to the last integral in equation (3.22) and considering that $r\left(\frac{\partial v}{\partial r} + \frac{v}{r}\right) = \frac{\partial}{\partial r}(vr)$ as well as applying the Leibniz theorem for integration and differentiation on the first integral and taking into account that the non-slip boundary condition is valid and that $2\pi \int_0^a ru\,\mathrm{d}r = q$, yields

$$\begin{aligned}
0 &= 2\pi \int_0^a r\frac{\partial u}{\partial x}\,\mathrm{d}r + 2\pi \int_0^a r\left(\frac{\partial v}{\partial r} + \frac{v}{r}\right)\,\mathrm{d}r = 2\pi \int_0^a r\frac{\partial u}{\partial x}\,\mathrm{d}r + 2\pi \int_0^a \frac{\partial}{\partial r}(vr)\,\mathrm{d}r = \\
&= 2\pi \int_0^a r\frac{\partial u}{\partial x}\,\mathrm{d}r + 2\pi a v(a) \overset{\text{Leibniz}}{\underset{\text{theorem}}{=}} \frac{\partial}{\partial x}\underbrace{2\pi \int_0^a ru\,\mathrm{d}r}_{=q} - \underbrace{u(a)\frac{\partial a}{\partial x}2\pi a}_{=0} + 2\pi a\frac{\partial a}{\partial t} = \\
&= \frac{\partial q}{\partial x} + 2\pi a\frac{\partial a}{\partial t}.
\end{aligned}$$

Since the cross-sectional area $A$ of the tube is given by $A(t) = \pi a^2(t)$, it holds that $\frac{\partial A}{\partial t} = 2\pi a\frac{\partial a}{\partial t}$. Hence, equation (3.22) can be rewritten as

$$0 = \frac{\partial q}{\partial x} + \frac{\partial A}{\partial t}. \tag{3.24}$$

By applying the Leibniz theorem on the first term of equation (3.23) and the non-slip boundary condition as well as the integral formulation of $q$ and considering that $p$ is independent of $r$, because of equation (3.21), and since $\left(\frac{\partial^2 u}{\partial r^2} + \frac{1}{r}\frac{\partial u}{\partial r}\right) = \frac{1}{r}\frac{\partial}{\partial r}\left(r\frac{\partial u}{\partial r}\right)$, equation (3.23) becomes

$$
\begin{aligned}
& 2\pi\rho\int_0^a r\frac{\partial u}{\partial t}\,\mathrm{d}r + 2\pi\int_0^a r\frac{\partial p}{\partial x}\,\mathrm{d}r = 2\pi\mu\int_0^a r\left(\frac{\partial^2 u}{\partial r^2}+\frac{1}{r}\frac{\partial u}{\partial r}\right)\mathrm{d}r \\
\Leftrightarrow\quad & \frac{\partial}{\partial t}\underbrace{\rho\left(2\pi\int_0^a ru\right)}_{=q}\mathrm{d}r - \underbrace{2\pi\rho a u(a)\frac{\partial a}{\partial t}}_{=0} + 2\pi\frac{\partial p}{\partial x}\int_0^a r\,\mathrm{d}r = 2\pi\mu\int_0^a r\frac{1}{r}\frac{\partial}{\partial r}\left(r\frac{\partial u}{\partial r}\right)\mathrm{d}r \\
\Leftrightarrow\quad & \rho\frac{\partial q}{\partial t} + 2\pi\frac{\partial p}{\partial x}\frac{r^2}{2}\bigg|_0^a = 2\pi\mu\int_0^a\frac{\partial}{\partial r}\left(r\frac{\partial u}{\partial r}\right)\mathrm{d}r \\
\Leftrightarrow\quad & \rho\frac{\partial q}{\partial t} + \pi a(t)^2\frac{\partial p}{\partial x} = 2\pi\mu\left(r\frac{\partial u}{\partial r}\right)\bigg|_0^a \\
\Leftrightarrow\quad & \rho\frac{\partial q}{\partial t} + \pi a(t)^2\frac{\partial p}{\partial x} = 2\pi\mu a(t)\left(\frac{\partial u}{\partial r}\right)\bigg|_{r=a}.
\end{aligned}
$$

Since $A(t) = \pi a(t)^2$ and $\mu\left(\frac{\partial u}{\partial r}\right)\Big|_{r=a} = -\tau_\omega$ with $\tau_\omega$ being the shear stress exerted to the wall, equation (3.23) can be written as

$$\rho\frac{\partial q}{\partial t} + A\frac{\partial p}{\partial x} = -2\pi a\tau_\omega. \tag{3.25}$$

As described in [10, 27, 30] the shear stress $\tau_\omega$ can also be set in relation to the flow $q$. This is done in order to express $\tau_\omega$ via the flow $q$. Thus, equation (3.25) will no longer explicitly no longer $\tau_\omega$. To be able to do so, a wave ansatz $u(x,r,t) = U(r)e^{i\omega\left(t-\frac{x}{c}\right)}$ is inserted into equation (3.20) to obtain an expression for $\tau_\omega$ via this ansatz, especially in respect to the received solution for $U(r)$. Hence, this equation transforms into

$$
\begin{aligned}
& i\omega\rho U(r)e^{i\omega\left(t-\frac{x}{c}\right)} + \frac{\partial p}{\partial x} = \mu\left(\frac{\partial^2 U}{\partial r^2}e^{i\omega\left(t-\frac{x}{c}\right)} + \frac{1}{r}\frac{\partial U}{\partial r}e^{i\omega\left(t-\frac{x}{c}\right)}\right) \\
\Leftrightarrow\quad & i\omega\rho U(r) + \frac{\partial p}{\partial x}e^{-i\omega\left(t-\frac{x}{c}\right)} = \mu\left(\frac{\partial^2 U}{\partial r^2} + \frac{1}{r}\frac{\partial U}{\partial r}\right).
\end{aligned} \tag{3.26}
$$

Here, $i$ is the imaginary unit and $\omega$ the angular velocity. As $\frac{\partial p}{\partial x}e^{-i\omega\left(t-\frac{x}{c}\right)}$ is the only term depending on $x$ in this equation and since $p$ is independent of $r$ (see equation (3.21)) and contrariwise $U$ only depends on $r$, it has to equal a constant $k = \frac{\partial p}{\partial x}e^{-i\omega\left(t-\frac{x}{c}\right)}$. Hence,

$$ke^{i\omega\left(t-\frac{x}{c}\right)} = \frac{\partial p}{\partial x}.$$

Inserting this expression for $\frac{\partial p}{\partial x}$ into equation (3.26), dividing by $\mu$ and multiplying by $r^2$ yields

$$\frac{kr^2}{\mu} = r^2\frac{\partial^2 U}{\partial r^2} + r\frac{\partial U}{\partial r} - \frac{i\Omega^2 r^2}{a^2}U(r),$$

with $\Omega = \sqrt{\frac{\omega\rho}{\mu}}a$ being the so-called Womersley number. Via coordinate transformation, given by $\zeta(r) = \Lambda\frac{r}{a}$, with $\Lambda = i^{\frac{3}{2}}\Omega$, the homogeneous part of this equation can be further transformed

into a Bessel equation of order 0 and so the solution of the last equation is given by

$$U(r) = \frac{ika^2}{\mu\Omega^2}\left(1 - \frac{J_0(\zeta(\Omega))}{J_0(\Lambda)}\right).$$

$J_0$ is a Bessel function of order 0. Inserting this solution of $U(r)$ into the wave ansatz for $u(x,r,t)$ results in

$$u(x,r,t) = \frac{ika^2}{\mu\Omega^2}\left(1 - \frac{J_0(\zeta(\Omega))}{J_0(\Lambda)}\right)e^{i\omega\left(t-\frac{x}{c}\right)}. \tag{3.27}$$

Substituting this expression for $u$ in the relation for the shear stress, $\mu\left(\frac{\partial u}{\partial r}\right)\Big|_{r=a} = -\tau_\omega$, mentioned before, and considering that $\frac{\mathrm{d}J_0(\zeta)}{\mathrm{d}\zeta} = -J_1(\zeta)$ is a Bessel function of order 1 leads to

$$\begin{aligned}
\tau_\omega &= -\frac{ika^2}{\Omega^2}e^{i\omega\left(t-\frac{x}{c}\right)}\frac{\partial}{\partial r}\left(1 - \frac{J_0(\zeta(r))}{J_0(\Lambda)}\right)_{r=a} = -\frac{ka}{\Lambda}\frac{J_1(\Lambda)}{J_0(\Lambda)}e^{i\omega\left(t-\frac{x}{c}\right)} \\
\Leftrightarrow \qquad -\tau_\omega\frac{J_0(\Lambda)}{J_1(\Lambda)} &= \frac{ka}{\Lambda}e^{i\omega\left(t-\frac{x}{c}\right)}.
\end{aligned} \tag{3.28}$$

Moreover, the flow $q$ can be obtained by integration of the flow velocity $u$ over the cross-sectional area $A$ of the tube, as already mentioned. Thereby, $q$ can be written as

$$\begin{aligned}
q &= 2\pi\int_0^a ru\,\mathrm{d}r \overset{(3.27)}{=} 2\pi\frac{ika^2}{\mu\Omega^2}e^{i\omega\left(t-\frac{x}{c}\right)}\int_0^a r\left(1 - \frac{J_0(\zeta(r))}{J_0(\Lambda)}\right)\mathrm{d}r = \\
&= \frac{i\pi ka^4}{\mu\Omega^2}\left(1 - \frac{2J_1(\Lambda)}{\Lambda J_0(\Lambda)}\right)e^{i\omega\left(t-\frac{x}{c}\right)}.
\end{aligned} \tag{3.29}$$

This was done to be able to express $q$ with respect to $\tau_\omega$. The last equality holds since $\int \zeta J_0(\zeta)\,\mathrm{d}\zeta = \zeta J_1(\zeta)$. Inserting equation (3.28) into relation (3.29) yields

$$\begin{aligned}
q &= \frac{i\pi ka^4}{\mu\Omega^2}\left(1 - \frac{2J_1(\Lambda)}{\Lambda J_0(\Lambda)}\right)e^{i\omega\left(t-\frac{x}{c}\right)} = \underbrace{e^{i\omega\left(t-\frac{x}{c}\right)}\frac{ka}{i^{\frac{3}{2}}\Omega}}_{=-\tau_\omega\frac{J_0(\Lambda)}{J_1(\Lambda)}}\cdot\frac{i\pi a^3 i^{\frac{3}{2}}}{\mu\Omega}\left(1 - \frac{2J_1(\Lambda)}{\Lambda J_0(\Lambda)}\right) = \\
&= -\tau_\omega\frac{J_0(\Lambda)}{J_1(\Lambda)}\cdot\frac{i\pi a^3 i^{\frac{3}{2}}}{\mu\Omega}\left(1 - \frac{2J_1(\Lambda)}{\Lambda J_0(\Lambda)}\right).
\end{aligned} \tag{3.30}$$

By defining the Womersley function $F_{10} = \frac{2J_1\left(i^{\frac{3}{2}}\Omega\right)}{i^{\frac{3}{2}}\Omega J_0\left(i^{\frac{3}{2}}\Omega\right)}$ and taking into account that $\Lambda = i^{\frac{3}{2}}\Omega$, the relation (3.30) for $q$ can be rewritten as

$$\begin{aligned}
q &= -\tau_\omega\frac{J_0(\Lambda)}{J_1(\Lambda)}\cdot\frac{i\pi a^3 i^{\frac{3}{2}}}{\mu\Omega}\left(1 - \frac{2J_1(\Lambda)}{\Lambda J_0(\Lambda)}\right) = -\tau_\omega\underbrace{\frac{\Lambda J_0(\Lambda)}{2J_1(\Lambda)}}_{=\frac{1}{F_{10}(\Omega)}}\cdot\frac{2i\pi a^3}{\mu\Omega^2}\underbrace{\left(1 - \frac{2J_1(\Lambda)}{\Lambda J_0(\Lambda)}\right)}_{=1-F_{10}(\Omega)} \\
&= -\tau_\omega\frac{1 - F_{10}(\Omega)}{F_{10}(\Omega)}\frac{2i\pi a^3}{\mu\Omega^2} = -\tau_\omega\frac{1 - F_{10}(\Omega)}{F_{10}(\Omega)}\frac{2i\pi}{\rho\omega}a.
\end{aligned}$$

By this equation the shear stress $\tau_\omega$ can be expressed with respect to $q$ by

$$\tau_\omega = \frac{i\rho\omega}{2\pi a}\frac{F_{10}(\Omega)}{1-F_{10}(\Omega)}q,$$

and therefore, equation (3.25) eventually becomes

$$\rho\frac{\partial q}{\partial t} + A\frac{\partial p}{\partial x} = -2\pi\tau_\omega = -i\rho\omega\frac{F_{10}(\Omega)}{1-F_{10}(\Omega)}q. \tag{3.31}$$

The objective of the following calculations is to reformulate equation (3.24), such that a second one-dimensional differential equation of first order depending on the according derivatives of pressure $p$ and flow $q$ is obtained.

For further simplification of equation (3.24) it is assumed that $A$ is not explicitly depending on time $t$. $A$ is rather depending on $t$ via the pressure $p$. Thus, $\frac{\partial A}{\partial t}$ can be expressed as

$$\frac{\partial A}{\partial t} = \frac{\partial A}{\partial p}\frac{\partial p}{\partial t}, \tag{3.32}$$

where $\frac{\partial A}{\partial p}$ describes the degree of distension of the cross-sectional area under pressure. Thereby, equation (3.24) turns into

$$0 = \frac{\partial q}{\partial x} + \frac{\partial A}{\partial p}\frac{\partial p}{\partial t}. \tag{3.33}$$

Now, to derive another expression for the constant $c_0$, inviscid flow, which implies $\mu = 0$, is assumed. Therefore, $\tau_\omega$ is set to zero in equation (3.25). Hereinafter, it will be shown that pressure $p$ and flow $q$ are underlying the same wave-equation. Hence, they travel with the same wave speed. To be able to show this, the equations

$$0 = \frac{\partial q}{\partial x} + \frac{\partial A}{\partial p}\frac{\partial p}{\partial t},$$
$$0 = \rho\frac{\partial q}{\partial t} + A\frac{\partial p}{\partial x},$$

will be reduced. In order to do so, $\frac{\partial A}{\partial p}$ is assumed to be constant with respect to $x$ as well as $t$, which is equivalent to the assumption of linear elasticity. Differentiation of the equations given above with respect to $x$ and $t$ leads to

$$0 = \frac{\partial}{\partial x}\left(\frac{\partial q}{\partial x} + \frac{\partial A}{\partial p}\frac{\partial p}{\partial t}\right) = \frac{\partial^2 q}{\partial x^2} + \underbrace{\frac{\partial}{\partial x}\left(\frac{\partial A}{\partial p}\right)}_{=0}\frac{\partial p}{\partial t} + \frac{\partial A}{\partial p}\frac{\partial^2 p}{\partial x \partial t}, \tag{3.34}$$

$$0 = \frac{\partial}{\partial t}\left(\frac{\partial q}{\partial x} + \frac{\partial A}{\partial p}\frac{\partial p}{\partial t}\right) = \frac{\partial^2 q}{\partial t \partial x} + \underbrace{\frac{\partial}{\partial t}\left(\frac{\partial A}{\partial p}\right)}_{=0}\frac{\partial p}{\partial t} + \frac{\partial A}{\partial p}\frac{\partial^2 p}{\partial t^2}, \tag{3.35}$$

$$0 = \frac{\partial}{\partial x}\left(\rho\frac{\partial q}{\partial t} + A\frac{\partial p}{\partial x}\right) = \rho\frac{\partial^2 q}{\partial t \partial x} + \frac{\partial A}{\partial p}\frac{\partial p}{\partial x}\frac{\partial p}{\partial x} + A\frac{\partial^2 p}{\partial x^2}, \tag{3.36}$$

$$0 = \frac{\partial}{\partial t}\left(\rho\frac{\partial q}{\partial t} + A\frac{\partial p}{\partial x}\right) = \rho\frac{\partial^2 q}{\partial t^2} + \frac{\partial A}{\partial p}\frac{\partial p}{\partial t}\frac{\partial p}{\partial x} + A\frac{\partial^2 p}{\partial x \partial t}. \tag{3.37}$$

Via linearisation with respect to $p$ equations (3.36) and (3.37) become

$$0 = \rho\frac{\partial^2 q}{\partial t \partial x} + A\frac{\partial^2 p}{\partial x^2}, \tag{3.38}$$

$$0 = \rho\frac{\partial^2 q}{\partial t^2} + A\frac{\partial^2 p}{\partial t \partial x}. \tag{3.39}$$

Subtracting equation (3.39) from equation (3.34) and equation (3.38) from equation (3.35) results in

$$0 = \frac{A}{\rho}\frac{\partial^2 q}{\partial x^2} - \frac{\partial A}{\partial p}\frac{\partial^2 q}{\partial t^2},$$

$$0 = \frac{\partial A}{\partial p}\frac{\partial^2 p}{\partial t^2} - \frac{A}{\rho}\frac{\partial^2 p}{\partial x^2},$$

which is equivalent to

$$\frac{\partial^2 q}{\partial t^2} = c_0^2\frac{\partial^2 q}{\partial x^2},$$

$$\frac{\partial^2 p}{\partial t^2} = c_0^2\frac{\partial^2 p}{\partial x^2},$$

with the constant $c_0$ given by

$$c_0^2 = \frac{A}{\rho}\frac{\partial p}{\partial A}. \tag{3.40}$$

Hence, to be able to rewrite equation (3.24) in terms of $\frac{\partial p}{\partial t}$ instead of $\frac{\partial A}{\partial t}$, the relationship (3.40) between the wave speed $c_0$ for inviscid flow and $\frac{\partial A}{\partial p}$ is inserted into equation (3.32), which yields

$$\frac{\partial A}{\partial t} = \frac{A}{\rho c_0^2}\frac{\partial p}{\partial t}.$$

Finally, equation (3.24) and hence also equation (3.22) can be rewritten as

$$0 = \frac{\partial q}{\partial x} + \frac{A}{\rho c_0^2}\frac{\partial p}{\partial t}. \tag{3.41}$$

The differential equations system of the Womersley equations is eventually given by equations (3.41) and (3.31)

$$0 = \frac{\partial q}{\partial x} + \frac{A}{\rho c_0^2}\frac{\partial p}{\partial t}, \tag{3.42}$$

$$\rho\frac{\partial q}{\partial t} + A\frac{\partial p}{\partial x} = -i\rho\omega\frac{F_{10}(\Omega)}{1 - F_{10}(\Omega)}q. \tag{3.43}$$

Their solution - following [10] - for a periodic input waveform can be written as sum of a stationary and an oscillatory part. For deriving the oscillatory component of the solution, Fourier analysis amongst others was used. But for further detail how the whole solution can be deduced see [10, 30]. The solution takes the form

$$p(x,t) = p_s(x) + Real\left(\sum_{n=1}^{\infty} p_{f,n}(x,t) + \sum_{n=1}^{\infty} p_{b,n}(x,t)\right)$$
$$q(x,t) = q_s(x) + Real\left(\sum_{n=1}^{\infty} q_{f,n}(x,t) + \sum_{n=1}^{\infty} q_{b,n}(x,t)\right)$$

The stationary components, $p_s(x)$ and $q_s(x)$, are given by

$$p_s(x) = p_s(0) + \frac{\Delta p_s}{L}x,$$
$$q_s(x) = -\Delta p_s \frac{\pi a^4}{8\mu L}.$$

But for $\Delta p_s$ the pressures at the inlet and outlet of a vessel have to be known. For the oscillatory components at harmonic $n$ one has to look at forward, $p_{f,n}$, and backward, $p_{b,n}$, pressure waves, which are given by

$$p_{f,n}(x,t) = P_{f,n} e^{i\omega_n\left(t - \frac{x}{c_n}\right)}, \tag{3.44}$$
$$p_{b,n}(x,t) = P_{b,n} e^{i\omega_n\left(t + \frac{x}{c_n}\right)}. \tag{3.45}$$

Here, $P_{f,n}$ and $P_{b,n}$ are coefficients, which are different for the various vessels. $c_n$ is the wave speed and it holds that $c_n = c_0\sqrt{(1 - F_{10}(\Omega))\frac{1}{1-\sigma^2}}$ with $c_0$ given by equation (3.19) and $\Omega_n = \sqrt{\frac{\rho\omega_n}{\mu}}a$ and $\omega_n = 2\pi n f_0$, being the angular frequency, $f_0$ the heart rate and $n$ the harmonic. Forward, $q_{f,n}$, and backward, $q_{b,n}$, flow waves are given similarly by

$$q_{f,n}(x,t) = Q_{f,n} e^{i\omega_n\left(t - \frac{x}{c_n}\right)}, \tag{3.46}$$
$$q_{b,n}(x,t) = Q_{b,n} e^{i\omega_n\left(t + \frac{x}{c_n}\right)}. \tag{3.47}$$

Furthermore, it can be shown, that the relation between forward and backward waves can be described with the help of the reflection coefficient $d_n$. Since, in this model reflection and therefore backward travelling waves only arise from bifurcation, the reflection coefficient is defined as ratio of backward to forward travelling waves at the bifurcation $x = L$ and therefore

$$d_n = \frac{p_{b,n}(L,t)}{p_{f,n}(L,t)}.$$

The reflection coefficient takes only non negative values. For $d_n = 1$, it means that total reflection occurs, while $d_n$ close to 0 means that reflection of only a small part of the forward wave takes place. Furthermore, $d_n$ can be described in terms of pressure waves as well as in terms of flow

waves. Considering flow waves, it has to be taken into account that flow is reflected negatively. Thus, $Q_{b,n}$ is negative and in order to obtain a positive reflection coefficient $d_n$, the backward travelling wave $q_{b,n}$ has to be multiplied by $-1$. Hence,

$$d_n = \frac{p_{b,n}(L,t)}{p_{f,n}(L,t)} = \frac{-q_{b,n}(L,t)}{q_{f,n}(L,t)}. \tag{3.48}$$

By inserting equations (3.44) and (3.45) at $x = L$ into equation (3.48) one gets

$$d_n = \frac{p_{b,n}(L,t)}{p_{f,n}(L,t)} = \frac{P_{b,n}e^{i\omega_n\left(t-\frac{L}{c_n}\right)}}{P_{f,n}e^{i\omega_n\left(t+\frac{L}{c_n}\right)}} = \frac{P_{b,n}e^{i\omega_n(t)}e^{i\omega_n\left(\frac{-L}{c_n}\right)}}{P_{f,n}e^{i\omega_n(t)}e^{i\omega_n\left(\frac{L}{c_n}\right)}} = \frac{P_{b,n}}{P_{f,n}}e^{\frac{-2i\omega_n L}{c_n}}. \tag{3.49}$$

Thus, the following equation is valid for the pressure wave

$$P_{b,n} = P_{f,n}d_n e^{\frac{2i\omega_n L}{c_n}},$$

and similarly for the flow waves

$$Q_{b,n} = -Q_{f,n}d_n e^{\frac{2i\omega_n L}{c_n}}.$$

Moreover, the coefficients of the pressure and flow waves are also related to the characteristic impedance $Z_{c,n}$ of the vessel via their ratio and hence given by

$$Z_{c,n} = \frac{p_{f,n}(x,t)}{q_{f,n}(x,t)} = \frac{P_{f,n}}{Q_{f,n}} = -\frac{P_{b,n}}{Q_{b,n}} = \frac{c_0^2\rho}{\pi a^2 c_n}.$$

### 3.2.2 Literature Review of Applications of the Womersley Equations in the Pulmonary Circulations

The Womersley equations have been used for describing pressure and flow not only in the systemic but also in the pulmonary circulation for example by Wiener et al. [29], Milnor et al. [19] and Bargainer [1]. Milnor et al. [19] motivated the application of the Womersley method in the pulmonary circulation by three reasons:

1. The impacts of the violation of the assumptions one has to make for applying the Womersley equations which can be estimated are relatively small.

2. The values estimated by the theory of Womersley in the range of $\Omega = 25-30$, which match with the first harmonic in man, correspond quite well with the results of measurements with electromagnetic flowmeters of the longitudinal impedance in the pulmonary artery of dogs.

3. Recordings by electromagnetic flowmeters of the flow pulses agree with their contours computed by the Womersley equations from the differential pressure in the pulmonary artery in the canine and human.

Hereinafter, a short overview of simulation results of applications of the the Womersely equations to the pulmonary circulation in literature is given.

**Wiener et al. [29]**

Wiener et al. [29] used uniform elastic tubes with circular cross-sections as basic elements to construct a mathematical model of the whole pulmonary circulation of dogs. They used the Weibel generation system for modelling the pulmonary branching system. Because the same assumptions as in Section 3.2.1 were considered, the Womersley equations and hence their solutions were used in this paper for modelling the pulmonary circulation. But they used a different formulation of equation (3.43). This formulation is based on the analogy of equation (3.43) to one electrical transmission line equation. Considering that it is possible to approach the solution for the periodic flow via waves, $q$ can be written as

$$q(t) = Qe^{i\omega t},$$

with $Q$ being the complex amplitude. Differentiating $q$ according to $t$ leads to

$$\frac{\partial q}{\partial t} = i\omega Q e^{i\omega t} = i\omega q. \tag{3.50}$$

Now, by inserting this relationship into equation (3.31) one gets

$$\rho i\omega q + A\frac{\partial p}{\partial x} = i\omega\rho\frac{1 - Me^{i\theta}}{Me^{i\theta}}q, \qquad \text{with} \qquad 1 - Me^{i\theta} = \frac{2J_1(i^{\frac{3}{2}}\Omega)}{i^{\frac{3}{2}}\Omega J_0(i^{\frac{3}{2}}\Omega)} = F_{10}(\Omega). \tag{3.51}$$

Further transformation like subtracting the first term, dividing by $-A$, factoring out equal terms and using Euler's formula result in

$$\begin{aligned} -\frac{\partial p}{\partial x} &= i\omega\frac{\rho}{A}\left(\frac{1 - Me^{i\theta}}{Me^{i\theta}}\right)q + i\omega\frac{\rho}{A}q = \frac{i\omega\rho}{A}\left(\frac{1 - Me^{i\theta}}{Me^{i\theta}} + 1\right)q = \frac{i\omega\rho}{A}\left(\frac{1}{Me^{i\theta}}\right)q = \\ &= \frac{i\omega\rho}{AM}\left(\cos(\theta) - i\sin(\theta)\right)q = \frac{i\omega\rho}{AM}\cos(\theta)q + \frac{\omega\rho}{AM}\sin(\theta)q = \\ &\overset{(3.50)}{=} \underbrace{\frac{\rho}{AM}\cos(\theta)}_{=:\tilde{L}}\frac{\partial q}{\partial t} + \underbrace{\frac{\omega\rho}{AM}\sin(\theta)}_{=:\tilde{R}}q. \end{aligned} \tag{3.52}$$

The in the last equality defined terms $\tilde{L}$ and $\tilde{R}$ are corresponding to the inductance and resistance of the electrical transmission line analogue.

Since the whole system includes bifurcations, also continuity of pressure and flow at each bifurcation was taken into account. Thus, the pressure of the parent vessel has to equal the pressures in the daughter vessels and on the other hand the flow in the stem has to be the same as the sum of the flows in the evolving vessels. The recorded pressures and flows from the MPA and the LA of 14 dogs were used as boundary conditions for the arterial and venous system. For computing flows and pressures, they firstly had to transform the measured pressure pulses

into their Fourier components. After calculating the Fourier coefficients, they found out that the first 10 harmonics already fit the measured curves within good accuracy. Then for each harmonic the arterial and venous pressures have been computed. The shape and magnitude of the peaks of the resulting flow were similar to measured ones, but particularly differed in detail at the venous ends, which can be seen in Figure 3.11.

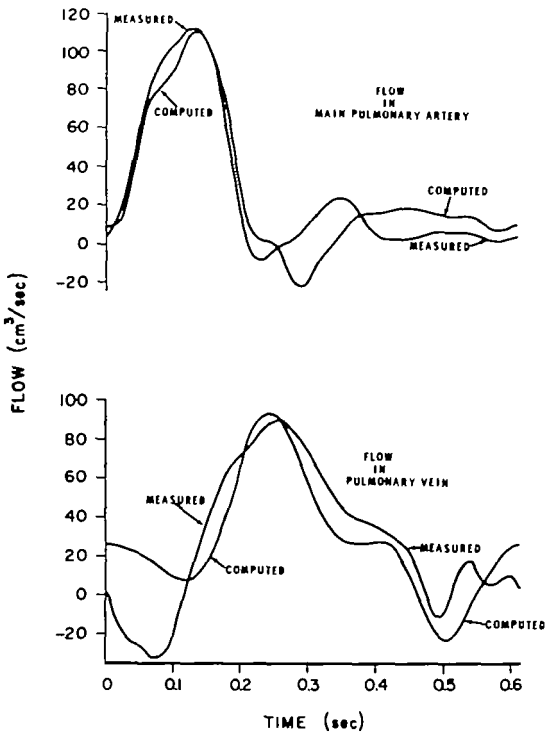


Figure 3.11: Comparsion of measured and simulated flow waveforms in the main pulmonary artery (MPA) (plot at the top) and a pulmonary vein (plot at the bottom). (Source: [29, p. 842])

They also investigated that pressure pulse becomes peaked during systole and flattens during diastole while the flow acts contrarily. In the small arteries both pressure and systolic flow are attenuated and the flow's diastolic peak vanishes. Furthermore, by passing through the capillary bed, the pressure is further reduced while the flow remains unchanged. The reason for the before mentioned characteristics is that the microcirculation is, compared to the arterial system, relatively indistensible. Hence, the pressure is severely damped because of viscous resistance and, on the other hand, the flow contour does not change since the rate of the outflow has to equal the rate of the inflow in this region. In terms of pulse transmission these observations are important features, since the indistensibility of small blood vessels is responsible for these effects. Hence, looking at the effects of the RV and the LA pulsations by separating them into arterial and venous pulses, this paper supports the view that because of the effect of the indistensible vessels on the pulmonary blood flow the venous blood flow is originating from the RV. The behaviour of pressure and flow waveforms throughout the whole pulmonary circulation

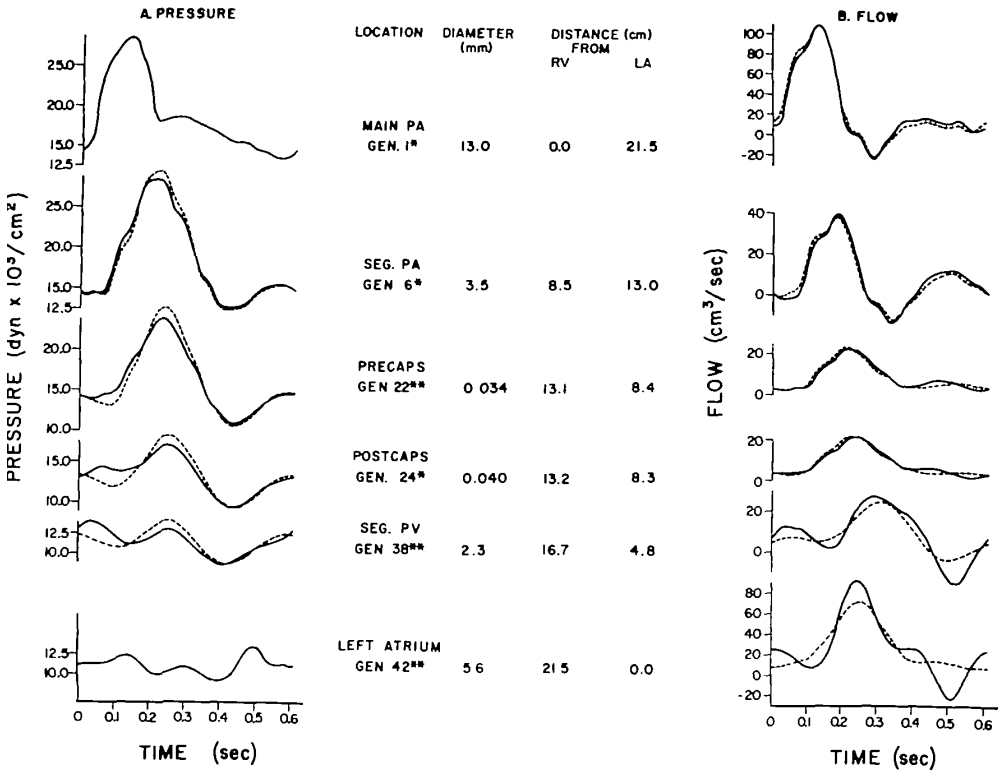


Figure 3.12: The pressure (left side of figure) and flow (right side of figure) pulses throughout the pulmonary circulation is shown here. The pressure curves in the main pulmonary artery (MPA) (top plot on left side) and the left atrium (LA) (bottom plot on left side) are experimentally measured pressure curves, which were used as boundary conditions. The dashed lines stand for the mean pressure/flow pulses and the corresponding oscillations originating from the right ventricle (RV). The solid lines additionally includes the oscillatory parts of the LA pressure/flow. Thus, the solid lines stand for the sum of the mean, arterial pulse and venous pulse pressure/flow. (Source: [29, p. 843])

is depicted in Figure 3.12.

Moreover, the impedance calculated from the computed data of the main pulmonary artery served as input impedance for the whole lung. They observed that the computed input impedances compared to the measured ones agree quite good up to the second harmonic (3.2 cycles/s). But at some higher frequencies they differ notably. For example the large computed impedance at the forth harmonic suggests that at this frequency there is resonance existent in this model. Since the pressure and flow are both relatively small for that harmonic, this modelling defect does not perceptibly influence the computed results.

Overall, they concluded that the results show that their branching elastic tube model may be utilised for describing the wave propagation in the whole pulmonary circulation in a useful way. They also deduced that the non-linear terms in the Navier-Stokes equations are on average small enough to get good approximations by the Womersley equations, although they might not be totally negligible. Furthermore, the results also indicated to which extent the shape of

the flow and pressure pulses traversing the vessels are affected by the interaction of arteries, capillaries and veins.

**Milnor et al [19]**

Milnor et al. [19] computed instantaneous blood flow velocity from differential pressure in the main pulmonary artery through Womersley's and McDonald's method. In this study the apparent phase velocity of the pressure wave as well as input impedance were measured in 10 humans. 7 of the subjects were patients with pulmonary hypertension and mitral stenosis. The other 3 might have had slight abnormalities in structure and function but without any evidence of effects on the pulmonary vessels and hence, they were seen as "normal" subjects. Also the pressures in the LA were recorded in all except of one subject. The recorded proximal, distal and differential pressures were then converted into Fourier series, on the one hand, to make corrections and, on the other hand, to compute different parameters at each harmonic frequency. Four of these parameters were

- blood flow velocity determined by the Womersley equation from differential pressure,
- volume flow,
- pulmonary arterial input impedance and
- apparent phase velocity of the pressure wave.

For the calculations just harmonics below 12 cycles/s were considered. Furthermore, also mean flow, average phase velocity and characteristic impedance modulus were calculated. Here, the mean flow was averaged under the assumption that flow equals zero on average during diastole. The average phase velocity and the characteristic impedance are both estimated in the same way. They are defined as the means of the corresponding observed values but excluding all values which were too high and at low frequencies precipitously falling values and at the end of this decline also its minimum value. Especially the averaged phase velocity was calculated this way to gain a phase velocity which is not influenced by reflections any more.

They investigated that the shape of the computed flow waves resembled those of other studies, which were recorded with the help of electromagnetic flowmeters in the pulmonary artery of dogs. In all subjects the impedance modulus precipitously dropped from a high value at frequency 0 cycles/s to a minimum. This minimum appeared in most cases in the frequency range of $2-5$ cycles/s. Furthermore, small oscillations at frequencies higher than the mentioned minimum were observed. In the phase velocity spectrum similar characteristics appeared. This can be also seen in Figure 3.13 exemplary for three different patients (2 normal ones and one with pulmonary hypertension).

Also notably is that phase velocity and characteristic impedance both were lower in the "normal" subjects ($mean = 1.68$ m/s for phase velocity and $mean = 23$ dyne·s·cm$^{-5}$ for characteristic impedance) than in the subjects with pulmonary hypertension ($mean = 4.77$ m/s and

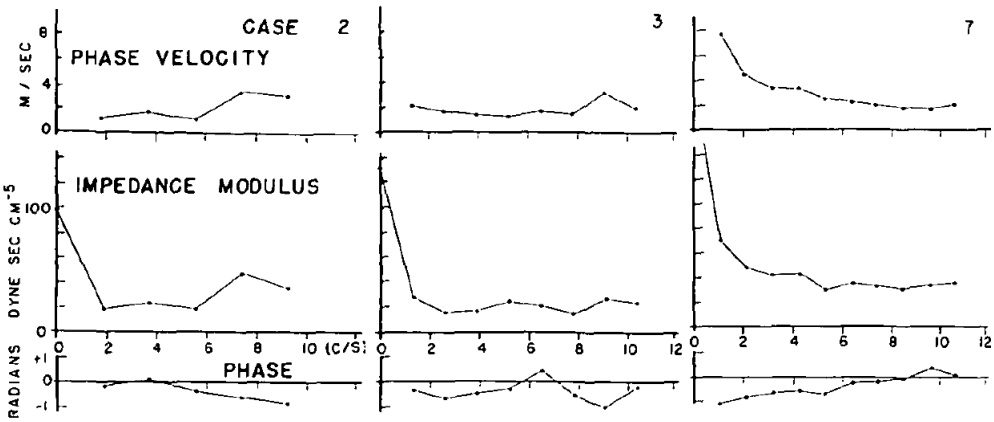


Figure 3.13: The apparent phase velocity (top), input impedance modulus (center) and input impedance phase (bottom) for three subjects. Here number 2 and 3 are referred to as "normal" cases and number 7 has pulmonary hypertension. (Source: [19, p. 640])

*mean* $= 46$ dyne $\cdot$ s $\cdot$ cm$^{-5}$ respectively). Additionally, they detected that phase velocity and characteristic impedance both correlate with the mean pulmonary arterial pressure. It was also found out that the frequencies, at which the first minimum was reached by impedance modulus and at which the zero baseline was crossed by impedance phase, are in direct relationship with the degree of pulmonary hypertension. So, they generalised this observation such that it can be said that the spectra are shifted to the right with increasing pulmonary arterial pressure. They also concluded that the results suggested that the humans with pulmonary hypertension had stiffer arteries than the 3 "normal" subjects. One possible explanation for this could be that arteries become stiffer because of distension.

**Bargrainer [1]**

One of the results of Bargainer's paper [1] is, as he concluded, supporting the approach of applying the Womersley theory to the pulmonary circulation. Bargainer performed experiments of measuring the differential pressure in the main pulmonary artery of 11 dogs. Therefore, via directly needle puncturing at two sides of the artery proximal and distal pressures were recorded simultaneously. The main aim was to determine the apparent phase velocity from the recorded input pressures. After preceding calculations like subtracting zero baseline from the input pressures and computing mean values for each pressure, a Fourier analysis was performed on the oscillatory waves. So, $P(t)$, the pressure pulsations, as function of time could be described as $P(t) = \bar{P} + \sum_{n=1}^{N} P_n \sin(n\omega t + \phi_n)$, where $\bar{P}$ is the mean pressure. $n$ represents the harmonic number, $N$ is the highest harmonic computed, $P_n$ stands for the modulus of the $n$th harmonic and $\phi_n$ for its phase. Afterwards, the apparent phase velocity was calculated. Bargainer observed that the average apparent phase velocity in the MPA over all measurements had a minimum at $2-3$ cycles/s and its maximum at approximately 5 cycles/s. After this maximum the phase velocity tends to oscillate. This behaviour can also be seen in Figure 3.14. Since this apparent

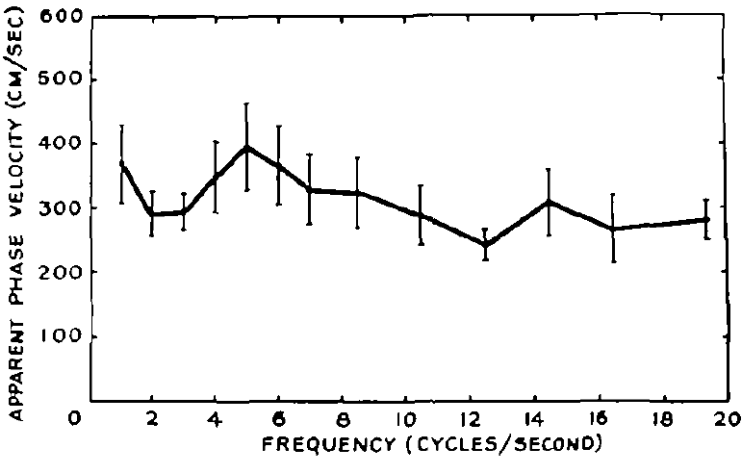


Figure 3.14: Average apparent phase velocity in the MPA from measurements of 11 dogs. Minimum of 292 cm/s between 2 and 3 cycles/s, maximum of 397 cm/s at 5 cycles/s. (Source: [1, p. 632])

phase velocity can be seen as the experimentally measured propagation velocity of the sinusoidal wave, it is influenced by incident and reflected waves and their summation and cancellation. So, phase velocity itself does not take these effects of reflections into account and was approximated by averaging the apparent phase velocity at frequencies $9 - 23$ cycles/s . The average phase velocity of all animals was 275 cm/s with $SD = 16$ cm/s. But it was significantly higher during serotonin infusion (417 cm/s with $SD = 29$ cm/s, while the same animal had a mean phase velocity of 267 cm/s with $SD = 22$ cm/s during the control period without serotonin infusion), which was also investigated. Also the elastic modulus could be calculated with the help of the phase velocity and took the value of $1.19 \cdot 10^6$ dyne/cm$^3$, which, he concluded, was in good agreement with other papers. Additionally, also characteristic impedance was computed by the relationship given by Womersley depending on the phase velocity

$$Z_0 = \frac{\rho c_0}{\sqrt{1-\sigma^2}} \frac{1}{\sqrt{M}} e^{(\frac{-i\theta}{2})}.$$

Here, $M$ and $\theta$ are functions of the Womersley number $\Omega$ as given in equation (3.51). The result given in this paper equals $Z_0 = 289$ dyne $\cdot$ s $\cdot$ cm$^{-3}$, which he again deduced to be similar to results of other studies. Hence, he came to the conclusion that this result supports the applicability of the Womersley's equations to the pulmonary vessels.

A short overview of the literature review of simulation of the pulmonary circulation with the Womersley equations approach given before, specifically the results of the studies of Wiener et al. [29], Milnor et al. [19] and Bargainer [1], is provided in Table 3.2.

Table 3.2: Overview of the literature review of papers which used the Womersley equations for modelling and simulation of the pulmonary circulation.

| | **Wiener et al. [29]** | **Milnor et al. [19]** | **Bargainer [1]** |
|---|---|---|---|
| species | dog | human | dog |
| modelled geometry | arterial & venous system (based on Weibel generation system) | MPA | MPA and pulmonary arteries |
| geometry data obtained from | measured values, others calculated from measured values and further taken from literature | measurements via angiograms | |
| modelling equations | Womersley equations based on analogy to one electrical transmission line equation ((3.42) & (3.52)) | Womersley's and McDonald's method | Womersley equations |
| boundary conditions | measured pressures in MPA and LA | measured pressure in MPA | measured pressure in MPA |

Table 3.2 – continued from previous page

| | **Wiener et al. [29]** | **Milnor et al. [19]** | **Bargainer [1]** |
|---|---|---|---|
| results | ressure pulse peakes during systole and flattens during diastole; flow acts contrarily<br>in the small arteries the flow's diastolic peak vanishes; by passing through the capillary bed the flow remains unchanged while pressure is further damped<br>computed input impedances at higher frequencies differ notably to measured ones | impedance modulus drops from high value at 0 cycles/s to a minimum at $2-5$ cycles/s and subsequently shows oscillatory behaviour<br>phase velocity spectrum indicates to have similar characteristics<br>phase velocity and characteristic impedance is lower in subjects without PH than in patients suffering from PH; the spectra are also shifted to the right with increasing disease stage | average apparent phase velocity in MPA has minimum at $2-3$ cycles/s and maximum at about 5 cycles/s; these characteristics are followed by an oscillatory behaviour<br>during serotonin infusion phase velocity was observed to be higher (417 cm/s) than during control period (267 cm/s) |

## 3.3 One-Dimensional Non-Linear Navier-Stokes Equations

The third method of modelling the blood flow in the pulmonary circulation considered in this thesis is again utilising the Navier-Stokes equations, but in contrast to the Womersley approach (given in Section 3.2) they are not linearised here. The discourse of the derivation of the one-dimensional non-linear Navier-Stokes equations is following the master thesis of Descovich [8], if not stated differently. Besides this discourse, also a small selection of applications and simulation results of this modelling approach in literature is provided.

### 3.3.1 Mathematical Derivation and Formulation

For applying the Navier-Stokes equations and their simplifications, the vessels are again assumed to be cylindric, elastic tubes with constant lengths. Furthermore, blood is considered to be an incompressible, homogeneous Newtonian fluid. Considering cylindrical coordinates the further assumptions are similar to those declared in Section 3.2. Hence, it is assumed that the vessels have circular cross-sections with an axisymmetric flow field and that external forces are negligible. Because of the axisymmetric flow field all variables are independent of the variable $\theta$. Another presumption is that pressure is only depending on position $x$ and time $t$, which means that pressure is constant at each cross-sectional area. Additionally, only radial distension is assumed. Hence, the wall is only distensible along the radial coordinate. So, for each point on the vessel wall the distension can be written as $\boldsymbol{\eta} = \eta \boldsymbol{e}_r$, with $\eta = a - a_0$ being the wall distension and $\boldsymbol{e}_r$ the unit vector in terms of the radial coordinate. Here, $a$ denotes the vessel radius and $a_0$ the radius at $t = 0$. Moreover, it is assumed that the velocity components, which are orthogonal to the $x-$axis are negligible compared to the velocity component $u_x$ in $x-$direction. The velocity component $u_x$ can also be written as

$$u_x(x, r, t) = \bar{u}(x) \cdot s\left(\frac{r}{a(x,t)}\right), \tag{3.53}$$

where $\bar{u}$ is the average flow velocity along each cross-sectional area and the function $s : \mathbb{R} \to \mathbb{R}$ describes the velocity profile. On all these assumptions the conservation of mass together with the Navier-Stokes equations in cylindrical coordinates can be written as

$$\operatorname{div} \boldsymbol{u} = 0, \qquad x \in (0, L), t \in I, \tag{3.54}$$

$$\frac{\partial u_x}{\partial t} + \operatorname{div}(u_x \boldsymbol{u}) + \frac{1}{\rho}\frac{\partial p}{\partial x} - \nu \Delta u_x = 0, \qquad x \in (0, L), t \in I. \tag{3.55}$$

Here, $\boldsymbol{u}$ is the velocity vector, $\rho$ stands for the density and $\nu$ is the kinematic viscosity and equals $\frac{\mu}{\rho}$, where $\mu$ is the dynamic viscosity used in Section 3.2. Furthermore, $p$ stands for the pressure and $I = [t_0, t_1]$ is the time interval one is looking at.

For the further derivation of the reduced one-dimensional non-linear Navier-Stokes model, the tube is considered of being a region $\Omega_t$, with $\Gamma_t^\omega := \{(x, r, \theta) : x \in (0, L), r = a(x, t), \theta \in [0, 2\pi)\}$

being the wall of the tube, which is moving under pressure.

$$\Gamma_t^{in} := \{(x, r, \theta) : x = 0, r \in [0, a(x,t)], \theta \in [0, 2\pi)\} \subset \partial\Omega_t$$

and

$$\Gamma_t^{out} := \{(x, r, \theta) : x = L, r \in [0, a(x,t)], \theta \in [0, 2\pi)\} \subset \partial\Omega_t$$

are the virtual boundaries at $x = 0$ and $x = L$ respectively, which is also depicted in Figure 3.15.

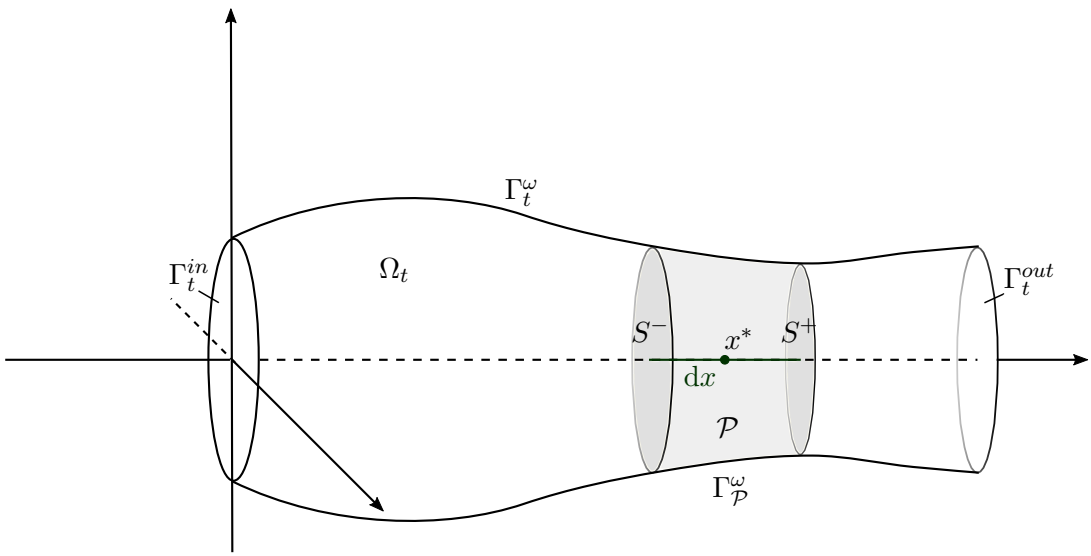


Figure 3.15: Schematic description of an elastic tube $\Omega_t$ with its wall $\Gamma_t^{\omega}$ and virtual boundaries $\Gamma_t^{in}$ and $\Gamma_t^{out}$. Also the tube section $\mathcal{P}$ with center $x^*$ and length $\mathrm{d}x$ and boundaries $\Gamma_{\mathcal{P}}^{\omega}, S^-$ and $S^+$ is depicted here.

Since there only is radial tube wall distensibility permitted, $\Gamma_t^{\omega}$ is moving while $\Gamma_t^{in}$ as well as $\Gamma_t^{out}$ are fixed. Furthermore, $\boldsymbol{n}$ is denoted as the outward-pointing unit vector of the surface $\partial\Omega_t$ and it holds that

$$\boldsymbol{u} = \dot{\boldsymbol{\eta}} \qquad on \quad \Gamma_t^{\omega}, \tag{3.56}$$

for all $t \in I$.

In the following, the equations (3.54) and (3.55) will be integrated over a tube section $\mathcal{P} \subset \Omega_T$ with length $\mathrm{d}x$. The centre of $\mathcal{P}$ is denoted as $x^* \in (0, L)$ and $\Gamma_{\mathcal{P}}^{\omega}$ is the wall of the tube section $\mathcal{P}$, see also Figure 3.15. For integration, it is presupposed that $\mathrm{d}x$ is sufficiently small, such that $x^* - \frac{\mathrm{d}x}{2} > 0$ and $x^* + \frac{\mathrm{d}x}{2} < L$. On the assumption that all functions are sufficiently smooth, the limit $\mathrm{d}x \to 0$ will be built. Overall, integration and subsequent converging of $\mathrm{d}x$ to 0 equals the integration over the cross-sectional area for deducing the Womersley equations.

Moreover, the average flow $q$ will be defined as

$$q = \int_S u_x \, \mathrm{d}\sigma = A\bar{u}. \tag{3.57}$$

Since $A$ is the cross-sectional area given as

$$A(x,t) = \pi a^2(x,t)$$

and the average flow velocity $\bar{u}$ can be written as

$$\bar{u}(x) = A^{-1} \int_S u_x \, \mathrm{d}\sigma,$$

where $S = S(x,t)$ represents a cross-sectional area, over which $u_x$ is integrated. Also a correction coefficient $\alpha$ given by

$$\alpha = \frac{\int_S u_x^2 \, \mathrm{d}\sigma(r)}{A\bar{u}^2} = \frac{\bar{u}^2 \int_S s^2 \, \mathrm{d}\sigma(r)}{A\bar{u}^2} = \frac{\int_S s^2 \, \mathrm{d}\sigma(r)}{A} \tag{3.58}$$

is needed and it holds that $\alpha \geq 1$. $\alpha$ is depending on the velocity profile, but here it is assumed to be constant. Hence, a constant velocity profile is presumed. For example, $\alpha$ takes the value of $\frac{4}{3}$, if there is a parabolic velocity profile present.

Now, considering the conservation of mass (see equation (3.54)) it will not be deduced into its reduced form again in this section, since all assumptions and the derivation are equivalent to those stated in Section 3.2. Hence, equation (3.54) can also be written as

$$\frac{\partial q}{\partial x} + \frac{\partial A}{\partial t} = 0. \tag{3.59}$$

For the derivation of the Navier-Stokes equation (3.55), only the terms which differ in the reduced form from the Womersley equation (3.43) will be concerned. So, by integration over $\mathcal{P}$ and by multiplying by $\rho$ and subsequently dividing by $\mathrm{d}x$ as well as building the limit $\mathrm{d}x \to 0$ equation (3.55) becomes

$$\lim_{\mathrm{d}x \to 0} \left( \frac{\rho}{\mathrm{d}x} \int_{\mathcal{P}} \left( \frac{\partial u_x}{\partial t} + \operatorname{div}(u_x \boldsymbol{u}) + \frac{1}{\rho} \frac{\partial p}{\partial x} \right) \right) = \lim_{\mathrm{d}x \to 0} \left( \frac{\nu \rho}{\mathrm{d}x} \int_{\mathcal{P}} \Delta u_x \right) \tag{3.60}$$

$$\Leftrightarrow \lim_{\mathrm{d}x \to 0} \frac{\rho}{\mathrm{d}x} \int_{\mathcal{P}} \frac{\partial u_x}{\partial t} + \lim_{\mathrm{d}x \to 0} \frac{\rho}{\mathrm{d}x} \int_{\mathcal{P}} \operatorname{div}(u_x \boldsymbol{u}) + \lim_{\mathrm{d}x \to 0} \frac{1}{\mathrm{d}x} \int_{\mathcal{P}} \frac{\partial p}{\partial x} = \lim_{\mathrm{d}x \to 0} \left( \frac{\mu}{\mathrm{d}x} \int_{\mathcal{P}} \Delta u_x \right). \tag{3.61}$$

The first term of equation (3.61) equals the first term in equation (3.23) and the third term equals the second term in equation (3.23). Hence, no closer look at the derivation of these terms will be taken. They can be rewritten as

$$\lim_{\mathrm{d}x \to 0} \frac{\rho}{\mathrm{d}x} \int_{\mathcal{P}} \frac{\partial u_x}{\partial t} \, \mathrm{d}V = \rho \frac{\partial q}{\partial t}, \tag{3.62}$$

$$\lim_{\mathrm{d}x \to 0} \frac{1}{\mathrm{d}x} \int_{\mathcal{P}} \frac{\partial p}{\partial x} \, \mathrm{d}V = A \frac{\partial p}{\partial x}. \tag{3.63}$$

The main difference between equation (3.61) and equation (3.23) is that in (3.61) there is still the divergence term $\int_{\mathcal{P}} \operatorname{div}(u_x \boldsymbol{u}) \, \mathrm{d}V$. In the derivation of the Womersley equations further assumptions were made. Specifically, it was assumed that the wave length $\lambda$ is large compared

to the vessel radius $a_0$. Additionally, the wave speed $c_0$ was presumed to be large compared to the average flow velocity $\bar{u}$. Therefore, after coordinate transformation the divergence term was negligible because of these assumptions. Since these assumptions are not made in this section, this term has to be specifically taken into account. So, considering the second term of equation (3.61) firstly Gauss's theorem will be applied. Hence, the divergence term can be written as

$$\lim_{\mathrm{d}x\to 0}\frac{\rho}{\mathrm{d}x}\int_{\mathcal{P}}\operatorname{div}(u_x\boldsymbol{u})\,\mathrm{d}V = \lim_{\mathrm{d}x\to 0}\frac{\rho}{\mathrm{d}x}\int_{\partial\mathcal{P}}u_x\boldsymbol{u}\cdot\boldsymbol{n}\,\mathrm{d}\sigma =$$
$$= \lim_{\mathrm{d}x\to 0}\frac{\rho}{\mathrm{d}x}\left(\int_{S^-}u_x\boldsymbol{u}\cdot(-\boldsymbol{e}_x)\,\mathrm{d}\sigma + \int_{S^+}u_x\boldsymbol{u}\cdot\boldsymbol{e}_x\,\mathrm{d}\sigma + \underbrace{\int_{\Gamma^\omega_{\mathcal{P}}}u_x\boldsymbol{g}\cdot\boldsymbol{n}\,\mathrm{d}\sigma}_{=0}\right).$$

Here $\boldsymbol{g}$ stands for the velocity at the boundary and is given by $\boldsymbol{g}=\dot{\boldsymbol{\eta}}$ on $\Gamma^\omega_{\mathcal{P}}$. The last equality in the equation given above holds, since for $\partial\mathcal{P}$ the equality $\partial\mathcal{P}=S^-\cup S^+\cup\Gamma^\omega_{\mathcal{P}}$ is valid as well as $\boldsymbol{n}=-\boldsymbol{e}_x$ on $S^-$ and $\boldsymbol{n}=\boldsymbol{e}_x$ on $S^+$. Furthermore, equation (3.56) implies that $u_x=0$ on $\Gamma^\omega_{\mathcal{P}}$. So, the last term of the above given equation equals zero. By first applying equation (3.58) to the remaining integrals and then approximating via Taylor polynomials around $x^*$, the divergence term subsequently becomes

$$\lim_{\mathrm{d}x\to 0}\frac{\rho}{\mathrm{d}x}\int_{\mathcal{P}}\operatorname{div}(u_x\boldsymbol{u})\,\mathrm{d}V = \lim_{\mathrm{d}x\to 0}\frac{\rho}{\mathrm{d}x}\left(-\int_{S^-}u_x^2\,\mathrm{d}\sigma + \int_{S^+}u_x^2\,\mathrm{d}\sigma\right)\overset{(3.58)}{=}$$
$$= \lim_{\mathrm{d}x\to 0}\frac{\rho}{\mathrm{d}x}\left(-\alpha A\left(x^*-\frac{\mathrm{d}x}{2}\right)\bar{u}^2\left(x^*-\frac{\mathrm{d}x}{2}\right)+\alpha A\left(x^*+\frac{\mathrm{d}x}{2}\right)\bar{u}^2\left(x^*+\frac{\mathrm{d}x}{2}\right)\right)\underset{\text{approximation}}{\overset{\text{Taylor}}{=}}$$
$$= \lim_{\mathrm{d}x\to 0}\frac{\rho}{\mathrm{d}x}\left(-\left(\alpha A(x^*)\bar{u}^2(x^*)-\frac{\mathrm{d}x}{2}\frac{\partial(\alpha A(x^*)\bar{u}^2(x^*))}{\partial x}\right)+\alpha A(x^*)\bar{u}^2(x^*)+\right.$$
$$\left.+\frac{\mathrm{d}x}{2}\frac{\partial(\alpha A(x^*)\bar{u}^2(x^*))}{\partial x}+o(\mathrm{d}x^2)\right)=$$
$$= \lim_{\mathrm{d}x\to 0}\frac{\rho}{\mathrm{d}x}\left(\mathrm{d}x\frac{\partial(\alpha A(x^*)\bar{u}^2(x^*))}{\partial x}+o(\mathrm{d}x^2)\right)=\rho\frac{\partial(\alpha A(x^*)\bar{u}^2(x^*))}{\partial x}.$$

Overall, the divergence term can be reduced to

$$\lim_{\mathrm{d}x\to 0}\frac{\rho}{\mathrm{d}x}\int_{\mathcal{P}}\operatorname{div}(u_x\boldsymbol{u})\,\mathrm{d}V=\rho\frac{\partial(\alpha A(x^*)\bar{u}^2(x^*))}{\partial x}. \tag{3.64}$$

Looking at the right hand side of equation (3.61) and considering that $\Delta u_x = \operatorname{div}(\nabla u_x)$ and applying the divergence theorem as well as splitting the boundary $\partial\mathcal{P}$ into $S^-, S^+$ and $\Gamma^\omega_{\mathcal{P}}$, as in the deviation above, leads to

$$\begin{aligned}
\lim_{\mathrm{d}x\to 0}\frac{\mu}{\mathrm{d}x}\int_{\mathcal{P}}\Delta u_x\,\mathrm{d}V &= \lim_{\mathrm{d}x\to 0}\frac{\mu}{\mathrm{d}x}\int_{\mathcal{P}}\operatorname{div}(\nabla u_x)\,\mathrm{d}V \overset{\text{divergence}}{\underset{\text{theorem}}{=}} \\
&= \lim_{\mathrm{d}x\to 0}\frac{\mu}{\mathrm{d}x}\int_{\partial\mathcal{P}}\nabla u_x\cdot\boldsymbol{u}\,\mathrm{d}\sigma \overset{\partial\mathcal{P}=S^-\cup S^+\cup\Gamma^\omega_{\mathcal{P}}}{=} \\
&= \lim_{\mathrm{d}x\to 0}\frac{\mu}{\mathrm{d}x}\left(\int_{S^-}\nabla u_x\cdot(-\boldsymbol{e}_x)\,\mathrm{d}\sigma + \int_{S^+}\nabla u_x\cdot\boldsymbol{e}_x\,\mathrm{d}\sigma + \int_{\Gamma^\omega_{\mathcal{P}}}\nabla u_x\cdot\boldsymbol{n}\,\mathrm{d}\sigma\right) = \\
&= \lim_{\mathrm{d}x\to 0}\frac{\mu}{\mathrm{d}x}\left(\int_{S^-}-\frac{\partial u_x}{\partial x}\,\mathrm{d}\sigma + \int_{S^+}\frac{\partial u_x}{\partial x}\,\mathrm{d}\sigma + \int_{\Gamma^\omega_{\mathcal{P}}}\nabla u_x\cdot\boldsymbol{n}\,\mathrm{d}\sigma\right).
\end{aligned}$$

By assuming that the change of $\frac{\partial u_x}{\partial x}$ along $x$ is small compared to the other terms, $\frac{\partial u_x}{\partial x}$ is considered to be small enough to be neglected. Hence, the first two integrals equal 0 and the above given equation chain further turns into

$$\begin{aligned}
\lim_{\mathrm{d}x\to 0}\frac{\mu}{\mathrm{d}x}\int_{\mathcal{P}}\Delta u_x\,\mathrm{d}V &= \lim_{\mathrm{d}x\to 0}\frac{\mu}{\mathrm{d}x}\int_{\Gamma^\omega_{\mathcal{P}}}\nabla u_x\cdot\boldsymbol{n}\,\mathrm{d}\sigma = \lim_{\mathrm{d}x\to 0}\frac{\mu}{\mathrm{d}x}\int_{\Gamma^\omega_{\mathcal{P}}}\nabla u_x\cdot(\boldsymbol{n}_x+\boldsymbol{n}_r+\boldsymbol{n}_\theta)\,\mathrm{d}\sigma \overset{\boldsymbol{n}_\theta=0}{=} \\
&= \lim_{\mathrm{d}x\to 0}\frac{\mu}{\mathrm{d}x}\left(\int_{\Gamma^\omega_{\mathcal{P}}}\nabla u_x\cdot\boldsymbol{n}_x\,\mathrm{d}\sigma + \int_{\Gamma^\omega_{\mathcal{P}}}\nabla u_x\cdot\boldsymbol{n}_r\,\mathrm{d}\sigma\right),
\end{aligned}$$

where the second equality holds, since the normal vector is divided in its radial and angular component ($\boldsymbol{n}_r$ and $\boldsymbol{n}_\theta$) and the component $\boldsymbol{n}_x$ in $x$-direction. Because of the cylindrical geometry, $\boldsymbol{n}_\theta$ equals 0. Hence, $\boldsymbol{n}_x = \boldsymbol{n} - \boldsymbol{n}_r$ with $\boldsymbol{n}_r$ being equal to $\boldsymbol{e}_r\cdot n_r$. Since $\boldsymbol{n}_x$ is the normal vector component pointing in $x$-direction, $\nabla u_x\cdot\boldsymbol{n}_x$ is proportional to $\frac{\partial u_x}{\partial x}$, thus negligible. Considering these and equation (3.53) the Laplace term subsequently transforms into

$$\begin{aligned}
\lim_{\mathrm{d}x\to 0}\frac{\mu}{\mathrm{d}x}\int_{\mathcal{P}}\Delta u_x\,\mathrm{d}V &= \lim_{\mathrm{d}x\to 0}\frac{\mu}{\mathrm{d}x}\left(\underbrace{\int_{\Gamma^\omega_{\mathcal{P}}}\nabla u_x\cdot\boldsymbol{n}_x\,\mathrm{d}\sigma}_{=0} + \int_{\Gamma^\omega_{\mathcal{P}}}\nabla u_x\cdot\boldsymbol{n}_r\,\mathrm{d}\sigma\right) = \\
&= \lim_{\mathrm{d}x\to 0}\frac{\mu}{\mathrm{d}x}\int_{\Gamma^\omega_{\mathcal{P}}} n_r\nabla u_x\cdot\boldsymbol{e}_r\,\mathrm{d}\sigma = \lim_{\mathrm{d}x\to 0}\frac{\mu}{\mathrm{d}x}\int_{\Gamma^\omega_{\mathcal{P}}} n_r\frac{\partial u_x}{\partial r}\,\mathrm{d}\sigma \overset{(3.53)}{=} \\
&= \lim_{\mathrm{d}x\to 0}\frac{\mu}{\mathrm{d}x}\int_{\Gamma^\omega_{\mathcal{P}}} n_r\frac{\partial}{\partial r}\left(\bar{u}(x)\cdot s\left(\frac{r}{a(x,t)}\right)\right)\mathrm{d}\sigma = \\
&= \lim_{\mathrm{d}x\to 0}\frac{\mu}{\mathrm{d}x}\int_{\Gamma^\omega_{\mathcal{P}}} n_r\bar{u}(x)s'\left(\frac{r}{a(x,t)}\right)\frac{1}{a(x,t)}\,\mathrm{d}\sigma \overset{r=a}{\underset{\text{on }\Gamma^\omega_{\mathcal{P}}}{=}} \\
&= \lim_{\mathrm{d}x\to 0}\frac{\mu}{\mathrm{d}x}\int_{\Gamma^\omega_{\mathcal{P}}} n_r\bar{u}(x)s'(1)\frac{1}{a(x,t)}\,\mathrm{d}\sigma.
\end{aligned}$$

Via substitution of variables $n_r \, \mathrm{d}\sigma = 2\pi a \, \mathrm{d}x$ the last integral becomes

$$\begin{aligned}\lim_{\mathrm{d}x\to 0} \frac{\mu}{\mathrm{d}x} \int_{\mathcal{P}} \Delta u_x \, \mathrm{d}V &= \lim_{\mathrm{d}x\to 0} \frac{\mu}{\mathrm{d}x} \int_{\Gamma_{\mathcal{P}}^{\omega}} n_r \bar{u}(x) \cdot s'(1) \cdot \frac{1}{a(x,t)} \, \mathrm{d}\sigma = \\ &= \lim_{\mathrm{d}x\to 0} \frac{\mu}{\mathrm{d}x} \int_{x^*-\frac{\mathrm{d}x}{2}}^{x^*+\frac{\mathrm{d}x}{2}} \bar{u}(x) \cdot s'(1) \cdot 2\pi \, \mathrm{d}x \approx \\ &\approx \lim_{\mathrm{d}x\to 0} \frac{\mu}{\mathrm{d}x} 2\pi s'(1) \cdot \bar{u}(x^*) \cdot dx = 2\pi\mu s'(1)\bar{u}(x^*).\end{aligned}$$

Here, the integral after the second equality is approximated by estimating the integral with the integrand at the center $x^*$ multiplied by the length of the interval $\mathrm{d}x$. Altogether, the right hand of equation (3.61) is approximated by

$$\lim_{\mathrm{d}x\to 0} \frac{\mu}{\mathrm{d}x} \int_{\mathcal{P}} \Delta u_x \, \mathrm{d}V \approx 2\pi\mu s'(1)\bar{u}(x^*). \tag{3.65}$$

By substituting each term of equation (3.61) with their corresponding reduced forms given in equations (3.62), (3.64), (3.63) and (3.65), equation (3.61) can be rewritten as

$$\rho\frac{\partial q}{\partial t} + \rho\frac{\partial(\alpha A\bar{u}^2)}{\partial x} + A\frac{\partial p}{\partial x} = 2\pi\mu s'(1)\bar{u}. \tag{3.66}$$

Applying the relationship $q = A\bar{u}$, given in equation (3.57), the above given equation eventually becomes

$$\rho\frac{\partial q}{\partial t} + \rho\alpha\frac{\partial \frac{q^2}{A}}{\partial x} + A\frac{\partial p}{\partial x} = 2\pi\mu s'(1)\frac{q}{A}. \tag{3.67}$$

As the system of differential equations (3.59) and (3.67) is depending on three variables, namely pressure $p$, flow $q$ and cross-sectional area $A$, a third equation is needed for solving the system. In order to do so, one possibility is setting the pressure $p$ into relation with the cross-sectional area $A$ via

$$p - p_{ext} = Eh\sqrt{\pi}\frac{\sqrt{A} - \sqrt{A_0}}{\sqrt{A_0}}. \tag{3.68}$$

The equation has its origin in a mechanical model of the displacement of the wall. Here, $p_{ext}$ stands for the external pressure, $E$ is the Young-modulus, $h$ the wall thickness at $t = 0$ and $A_0$ the cross-sectional area at $t = 0$.

Altogether, the system of differential equations for modelling the blood flow via the one-dimensional non-linear Navier-Stokes equations is given by

$$\frac{\partial q}{\partial x} + \frac{\partial A}{\partial t} = 0, \tag{3.69}$$

$$\rho\frac{\partial q}{\partial t} + \rho\alpha\frac{\partial \frac{q^2}{A}}{\partial x} + A\frac{\partial p}{\partial x} = 2\pi\mu s'(1)\frac{q}{A}, \tag{3.70}$$

$$p - p_{ext} = Eh\sqrt{\pi}\frac{\sqrt{A} - \sqrt{A_0}}{\sqrt{A_0}}. \tag{3.71}$$

### 3.3.2 Literature Review of Applications of the One-Dimensional Non-Linear Navier-Stokes Equations in the Pulmonary Circulation

The one-dimensional non-linear Navier-Stokes equations can be used not only for considering spatial pressure and flow distribution with possible wave reflections but also for determining the influence of the small vessels on the whole pulmonary circulation. This influence can be investigated by for example structured tree boundary conditions or other right boundary conditions as it was done by Qureshi et al. [23] and Clipp and Steele [7]. But also other outlet boundary conditions are possible as for example a measured pressure curve of the LA, which was done by Li and Cheng [17], or a Windkessel model, which was used by Lee et al. [16]. But finding the adequate right boundary condition might not be an easy task and therefore is also an disadvantage of this modelling approach. In the following, a short overview of the before mentioned studies is provided.

#### Li and Cheng [17]

Li and Cheng [17] applied the one-dimensional non-linear Navier-Stokes equations to 17 generations of blood vessels of the human pulmonary circulation, including arterial, capillary and venous vessels. For modelling the lungs they were discretised into a four-lobe model: left-low lobe, right-low lobe, right-upper lobe and left-upper lobe. Furthermore, the venous structure was modelled similar to the arterial one. The model equations used in this paper are the Navier-Stokes equations formulated slightly different to those given in equations (3.69) - (3.71):

$$\frac{\partial A}{\partial t} + \frac{\partial \bar{u} A}{\partial x} = 0, \tag{3.72}$$

$$\frac{\partial \bar{u}}{\partial t} + \frac{\partial \frac{\bar{u}^2}{2}}{\partial x} + \frac{1}{\rho}\frac{\partial p}{\partial x} + F = G_z, \tag{3.73}$$

$$p_T = p_T(A), \tag{3.74}$$

with the new parameters $F$ being the friction force given as $F = \frac{8\pi\mu}{A\rho}V$ and $G_z$ representing the external force. $p_T$ stand for the transmural pressure and equals $p - p_0$, with $p_0$ being the external pressure. For simulation the pressure curve of the RV was used as the left boundary condition and the pressure in the LA was taken as right boundary condition. Furthermore, a two-step Lax-Wendroff finite difference method for the interior points of the vessels together with a hybrid method of characteristics at the bifurcation points was used for simulation. At the boundary points continuity of flow and pressure had to be ensured by characteristic method formulation of the continuity of pressure and flow. The results of the simulation were only given for the right side of the lungs. They show that in the precapillary vessels the pressure drops significantly and even becomes negative in the postcapillaries in a short period of time. Due to this negative pressure vessels collapse in the postcapillary segments, which was also observed in experiments. Calculated pressure and velocity in the capillaries are given by the values of 7-9 mmHg and 0.05 cm/s - 0.2 cm/s respectively.

**Qureshi et al. [23]**

Qureshi et al. [23] developed a mathematical model depending on one-dimensional non-linear Navier-Stokes equations for all arteries and veins with radii $\geq 50\ \mu$m. The blood flow in the large arteries and veins, which radii are greater than 4.5 mm, namely the main pulmonary artery (MPA), the right and left pulmonary arteries (RPA & LPA), right/left interlobular arteries (RIA & LIA) and right/left trunk arteries (RTA & LTA) in the arterial system and the right and left inferior (RIV & LIV) and the right and left superior pulmonary veins (RSV & LSV) in chronological branching order, is modelled explicitly by the one-dimensional non-linear Navier-Stokes equations given by equation (3.69) and

$$\frac{\partial q}{\partial t} + \frac{\partial}{\partial x}\left(\frac{q^2}{A}\right) + \frac{A}{\rho}\frac{\partial p}{\partial x} = \frac{-2\pi\nu a}{\delta}\frac{q}{A}. \tag{3.75}$$

Here, $\nu$ is the kinematic viscosity, $\delta$ represents the boundary layer thickness and $a(x,t)$ is the vessel radius. For relating pressure and cross-sectional area they used a slightly different form of equation (3.71) given by

$$p - p_{ext} = \frac{4}{3}\frac{Eh}{a_0}\left(1 - \frac{\sqrt{A_0}}{\sqrt{A}}\right), \tag{3.76}$$

with $a_0$ being the radius related to $p(x,t) = p_0$. At bifurcations continuity of pressure and flow is taken into account. For numerically solving these equations, they also used a two-step Lax-Wendroff numerical scheme. A schematic representation of the model geometry of the pulmonary circulation is shown in Figure 3.16.

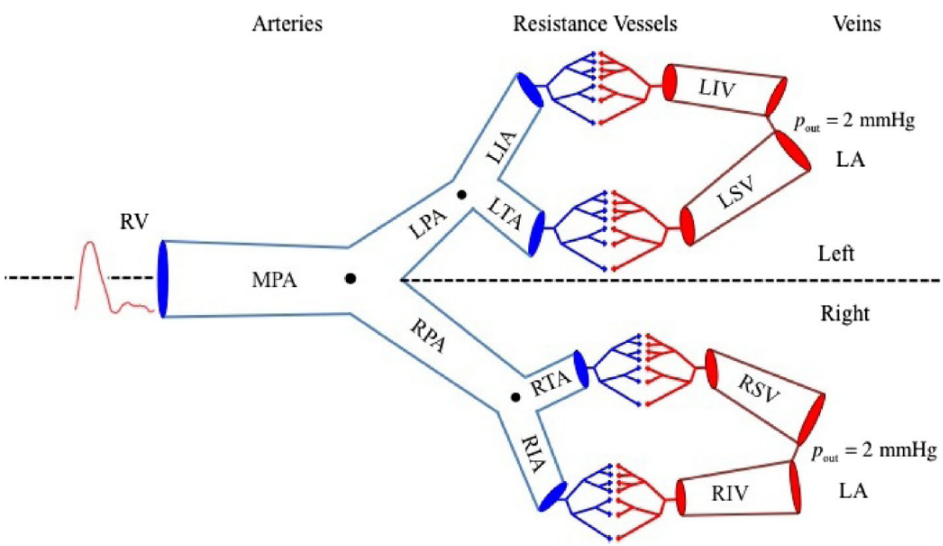


Figure 3.16: Illustration of the schematic description of the pulmonary circulation model by Qureshi et al. [23]. The large arteries and veins are modelled explicitly by the one-dimensional non-linear Navier-Stokes equations. The structured trees are represented in the figure as small branching arteries. (Source: [23, p. 1139])

All other arteries and veins, which were taken into account, were grouped together as small arteries and veins and modelled via the Womersley equations as pairs of structured arterial and venous trees connected at the smallest vessels. Since the venous tree was modelled as mirror image of the arterial tree, these trees have the same number of bifurcations and terminal vessels but different length-to-radius ratios and material properties, including compliance. Furthermore, the radii of the root vessels of the arterial and venous trees have to be equal to ensure the same number of branches in the corresponding trees. The radii of the vessels at each junction are assumed to be predictable from the radius of the root vessel $r_0$ by

$$r = \alpha^i \beta^j r_0, \tag{3.77}$$

with $\alpha, \beta$ being scaling factors. Here, $i, j$ are indices describing the pathway, with $i$ standing for the left path at a bifurcation and $j$ representing following the right branching vessels, see also Figure 3.17. The factors $\alpha$ and $\beta$, taken from the literature, are depending on three relations that govern the branching behaviour of smaller arteries.

$$r_p^\xi = r_{d_1}^\xi + r_{d_2}^\xi, \qquad 2.33 \leq \xi \leq 3, \tag{3.78}$$

$$\gamma = \frac{r_{d_1}^2}{r_{d_2}^2}, \tag{3.79}$$

$$\eta = \frac{r_{d_1}^2 + r_{d_2}^2}{r_p^2} = \frac{1+\gamma}{\left(1+\gamma^{\frac{\xi}{2}}\right)^{\frac{2}{\xi}}}, \qquad \eta > 1. \tag{3.80}$$

The first one is the so called powerlaw, $\gamma$ is an asymmetry ratio and $\eta$ is an area ratio. The subscripts stand for being a parent ($p$) or daughter ($d_1, d_2$) vessel. $\xi$ describes the type of flow and the value $\xi = 2.76$ is taken for arterial blood flow. The scaling factors $\alpha$ and $\beta$ also satisfy that $A_{d_1}$ and $A_{d_2}$ are both smaller than $A_p$ and that their sum $A_{d_1} + A_{d_2}$ is greater than $A_p$. Furthermore, also the length of a vessel has to be determined, which is done by the following length-to-radius ratios

$$l_{rr} = 15.75 r^{1.10} \qquad \text{for the arterial tree,}$$

$$l_{rr} = 14.54 r \qquad \text{for the venous tree.}$$

By this relation the asymmetry between the arterial and venous tree is obtained. The structured trees also serve as resistance to the flow and as a damping of the oscillations of the flow.

Each pair of structured trees represents a vascular bed for which the total admittance matrix is calculated by joining the admittances of the single vessels in parallel and series. This total admittance matrix is used as boundary condition for connecting the smallest large arteries with the corresponding large veins. For this, the distal diameters of the terminal large arteries and their corresponding veins have to be equal. For the arterial side of the pulmonary circulation an MRI measured flow rate waveform is the input boundary condition to the MPA. As mentioned the structured trees provide outflow boundary conditions for the large arterial side and inflow

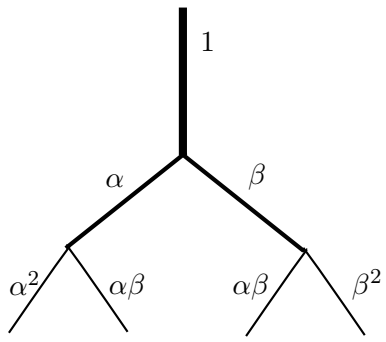


Figure 3.17: Schematic of numbering the branching vessels with their scaling factors $\alpha$ and $\beta$ for calculation of the radii given by equation (3.77).

boundary conditions for the large veins. The outflow boundary condition for the large veins is obtained by a constant pressure at the LA of 2 mmHg.

Qureshi et al. simulated the blood flows of a normal healthy young subject, here referred to as normal case, as well as for different kinds of pulmonary hypertension such as pulmonary arterial hypertension (PAH), pulmonary hypertension associated with hypoxic lung disease (HLD) and chronic thromboembolic pulmonary hypertension (CTEPH). The results of the normal case show that pressure is varying from 10 to 25 mmHg in the large arteries. Given that pressures and flows were predicted at the distal and proximal ends of a vessel, as well as its midpoint, peak pressures and arrival times for the reflected waves were differing in the different points of the MPA and RPA but not significantly in the LPA, which can be seen in the left column of Figure 3.18. For the venous large vessels the results indicated that the pressures have 2 maxima, hence they are biphasic, but they remain low in magnitude and variation. For the LIV the pressure is oscillating around 2 mmHg, while it stays above 2 mmHg for the RIV and RSV, see also Figure 3.18 at the right column. In the structured tree also the pressure drop was simulated and resulted in a decrease from 17 to 10 mmHg in the arterial structured tree and from 10 to 2 mmHg in the venous structured tree. In this context they also observed that the pressure in the $\alpha$ branches are smaller than those in the $\beta$ branches for the arterial structured tree and the other way around for the venous counterpart.

PAH was modelled by increasing the stiffness parameter $\frac{Eh}{r_0}$ due to the decrease in distensibility, which is caused by PAH. In the paper, they concluded that the increase of stiffness results in an increase of peak and pulse pressures as well as that the dicrotic notch tends to disappear in the MPA. The condition of PAH also implies amplified oscillations of the pressure in the RSV.

For modelling HLD the rarefaction of the vascular bed connected to this type of pulmonary hypertension was realised in the model by decreasing $\xi$ and $\gamma$ belonging to equations (3.78) and (3.79). Thus, also the area ratio $\eta$, given by equation (3.80), is decreasing within the structured tree. The results of blood flow simulation for HLD show that peak, trough and mean arterial pressures increase significantly with the decrease of vascular density. Also connected to this decrease is that incident and reflected pressure pulses tend to form only a single peak with less

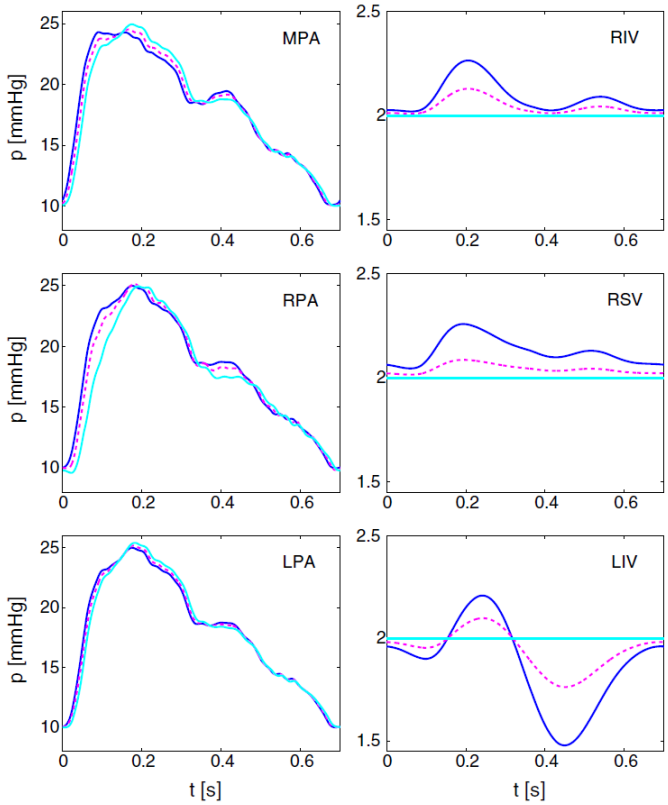


Figure 3.18: Simulated pressure waveforms of a healthy person at the inlet (blue line), the centre (magenta) and outlet (cyan) of the main arteries (main pulmonary artery (MPA), right pulmonary artery (RPA), left pulmonary artery (LPA)) and veins (right inferior pulmonary vein (RIV), right superior pulmonary vein (RSV), left inferior pulmonary vein (LIV)). The pressure waveforms of the arteries are depicted in the left column and venous pressure wavforms in the right column. (Source: [23, p. 1148])

characteristics in the pressure wave of the MPA. But the rarefaction also affects the pulmonary veins such that their pressure and flow amplitudes are reduced as well as shifting the pulse waves such that the pressure and flow waves are peaking earlier. The rarefaction also causes an overall higher pressure in the structured trees, since the inlet boundary to the structured trees is the increased pressure in the large arteries, as mentioned before.

Similar to PAH, CTEPH was also simulated by stiffening vessels, especially the large arteries up to doubling the normal value. The small vessels were also remodelled by uniform stiffening. Qureshi et al. observed that stiffening the large arteries causes an earlier as well as steeper and higher pressure peak followed by a second one shortly after the first. The stiffening of the large arteries also leads to a small decrease of the pressure amplitude and a small increase of the amplitude of the flow wave.

Overall, they found different characteristics for the different types of pulmonary hypertension, especially in terms of the pressure waveforms.

**Clipp and Steele [7]**

A study by Clipp and Steele [7] deals with creating a model, especially modelling its outlet boundary condition, which also takes effects of different states of respiration into account. They looked at the lungs divided up into 3 zones as described in Section 2.1.2. The paper again deals with the one-dimensional non-linear Navier-Stokes equations (3.69) and (3.70) together with equation (3.76) for modelling the large pulmonary arteries. The analogue to equation (3.70) was given in this paper by

$$\frac{\partial q}{\partial t} + \frac{\partial}{\partial x}\left(\frac{4}{3}\frac{q^2}{A}\right) + \frac{A}{\rho}\frac{\partial p}{\partial x} = -8\pi\nu\frac{q}{A} + \nu\frac{\partial^2 q}{\partial x^2}. \tag{3.81}$$

Clipp and Steele used a cast of lamb lungs to create the geometry of the large vessels of a lamb. The large vessels include the main pulmonary artery (MPA) and 3 to 4 levels of evolving vessels. Hence, their model consisted of 34 vessel outlets to which an impedance outlet boundary condition via structured trees was applied. As inlet boundary condition an experimentally measured blood flow waveform during expiration was used. Moreover, blood flows and pressures in the large arteries were calculated by an existing finite element analysis solver, which they developed earlier.

The small branches of each zone at expiration were modelled as structured trees. To simulate inspiration a scaling factor $f_e$ was introduced. With the help of $f_e$ they were able to modify the tree such that $r_e = f_e r$, with $r_e$ being the modified radius during inspiration. For modelling the structured trees they also used the powerlaw (3.78) and the root of the asymmetry ratio given in (3.79) as well as the length-to-radius ratio given by $l_{rr} = \frac{L}{r}$. Here, $L$ denotes the length and $r$ the radius of the vessel. This structured trees, as already mentioned, were used to determine an impedance boundary condition aligned to the zone specific vasculature during respiration.

They investigated the effects of different combinations of parameters for the structured trees. So, one parameter set was assuming a global $l_{rr}$ for all zones and on the other hand scaling factors, which were specific for each zone. The other parameter set was containing of length-to-radius ratios specified for each zone. For all three zones different asymmetry ratios and branch exponents $\xi$ in the powerlaw (3.78) were taken into account, but they were equal for both mentioned parameter sets. Furthermore, to be able to mimic respirational effects, the respiration factor $f_R$ was introduced to the structured tree model. This factor was again considered in two ways. Firstly, a global $f_R = 0.915$ was assumed. That means that $f_R$ is the same in all zones. Contrariwise, the second method was assuming a zonal $f_R$, which was determined by an optimization algorithm.

The previously mentioned two parameter sets were each applied to all three zones as well as to the assumption that the lungs are only composed of zone II and zone III. After that, both methods of modelling the effects of respiration were applied to all 4 given models. Overall, the results of the simulations showed that for expiration considering just 2 zones is better than considering 3 zones. Also using a zonal $l_{rr}$ showed better results than applying a global length-to-radius ratio. In terms of maximal inspiration, the zone dependent $l_{rr}$ was generally fitting

the experimental data better than the global $l_{rr}$ independent of the usage of a global or a zonal $f_R$. Furthermore, the results indicated that modelling just 2 zones with a zonal $l_{rr}$ as well as a zonal $f_R$ was better than applying the same parameters to a 3 zone model. On the other hand, the simulation of the three zones with zonal $l_{rr}$ and global $f_R$ showed better results than assuming only two zones. Altogether, Clipp and Steele concluded that the structured tree model with 2 zones and zonal $l_{rr}$ and zonal $f_R$ was the best method for modelling the outlet boundary condition under consideration of effects of respiration to the pulmonary circulation.

**Lee at al. [16]**

Lee et al. [16] used in their study the one-dimensional non-linear Navier-Stokes equations to set up a model for the first four generations containing of 13 vessels of the pulmonary circulation of a mouse. The Navier-Stokes equation in this paper are given by equations (3.69) and (3.75). By variation of the third necessary equation the model was applied to investigate the impact of a linear relation between pressure $p$ and vessel radius $r$ compared to the impact of a non-linear one. The linear formulation is given by equation (3.76), considering that $\sqrt{A} = r\sqrt{\pi}$. The non-linear pressure radius relation is an empirical function, which fits the measured data and is specified by

$$r(p) = r_0 + r_1 \left( \frac{1}{2} + \frac{\tan^{-1}\left(\frac{p-P_a}{P_b}\right)}{\pi} \right). \tag{3.82}$$

$r_0, r_1, P_a$ and $P_b$ are fitting parameters, which are determined numerically. As outlet boundary condition a 2-element Windkessel model was applied to the terminal arterioles. The inlet boundary condition was considered to be a periodic pulse, which was designated as a square pulse train with smoothed edges. At branching points continuity of pressure and mass conservation were taken into account. An illustration of this model description is shown in Figure 3.19. Furthermore, Lee et al. analysed the effects of applying the heterogeneity compared to the homogeneity of the vessel wall properties to the model. On the one hand, equation (3.82) was parametrised for each vessel differently. On the other hand, the mean properties of the whole vessel network was used for each vessel simultaneously. The required data of the vessel geometry was obtained from measurements by micro-computed tomography from a lung of a normal control mouse.

The equations were numerically solved by application of a finite difference method including a backward Euler, second-order Runge-Kutta and Godunov upwind method.

In addition to the already mentioned investigations, wave intensity analysis was considered as well as determining the effects of the size of the vessel network. Therefore, simulations of the heterogeneous non-linear wall model with $1, 2, 3$ and 4 vessel generations were performed. The pressure waveforms of the simulations can be seen in Figure 3.20. From this figure, they also concluded that at $t = 0.04$ s there is a local minimum in the pressure waveform of the main pulmonary artery, which approximately is the instant of time when the pulmonary valve closes. The pressure profiles of the 3 generation model compared to those of the 4 generation model only differ by 0.55%. Moreover, the results of the 3 generation model show that the pressure

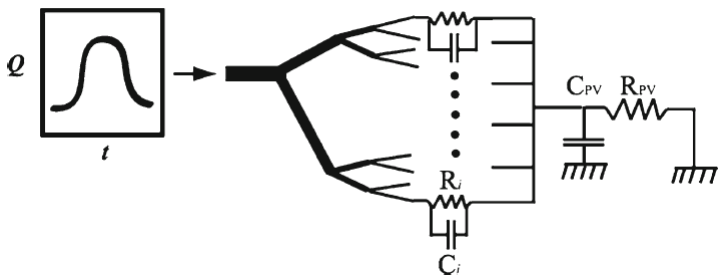


Figure 3.19: Illustration of the model description for four generations of arterial vessels used by Lee et al. with a square pulse train as inlet and a 2-element Windkessel model as the outlet boundary condition. (Source: [16, p. 1249])

pulse from the MPA first propagates into the vessel with the larger diameter and then into the smaller one.

In terms of the comparison of the heterogeneous and homogeneous model all simulation results were quite similar and differed with less than 3 percent in the MPA. But throughout the network there are differences in peak pulse wave velocity and also different impacts on the wall shear stress.

Comparing the heterogeneous linear and non-linear models they deduced that the pressures estimated by the linear model are a lot smaller than the pressures obtained by the non-linear model in the MPA, which also can be seen in Figure 3.21. Furthermore, with the help of wave intensity analysis, it was investigated that the linear model, in contrast to the non-linear one, underrates the amplitude of the incident and reflected compression waves.

Overall, Lee et al. concluded that it is not possible to decide with certainty if the linear or non-linear model is more accurate. But in terms of physiologically behaviour the non-linear model seems to be more realistic and therefore is also supposed to give more realistic results.

In Table 3.3 a short overview of the literature review of the papers of Li and Cheng [17], Qureshi et al. [23], Clipp and Steele [7] and Lee et al. [16] given before, is provided.

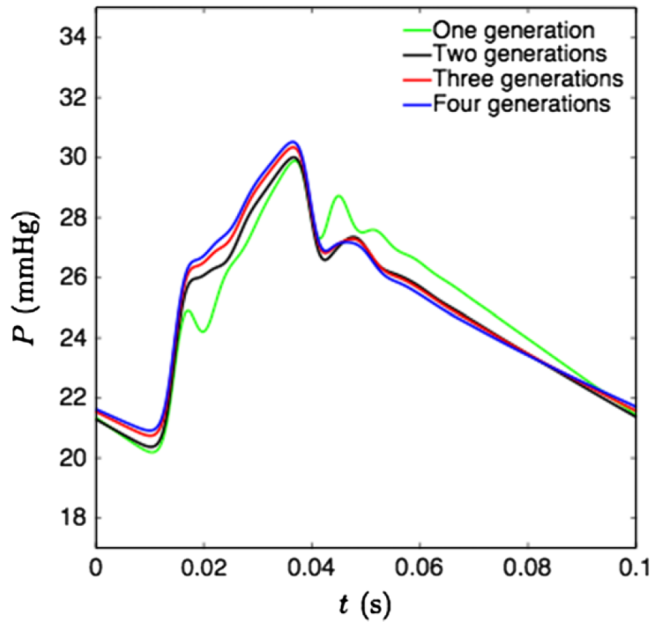


Figure 3.20: Illustration of the pressure waveforms of the simulations of the heterogeneous non-linear model through one to four generations. (Source: [16, p. 1255])

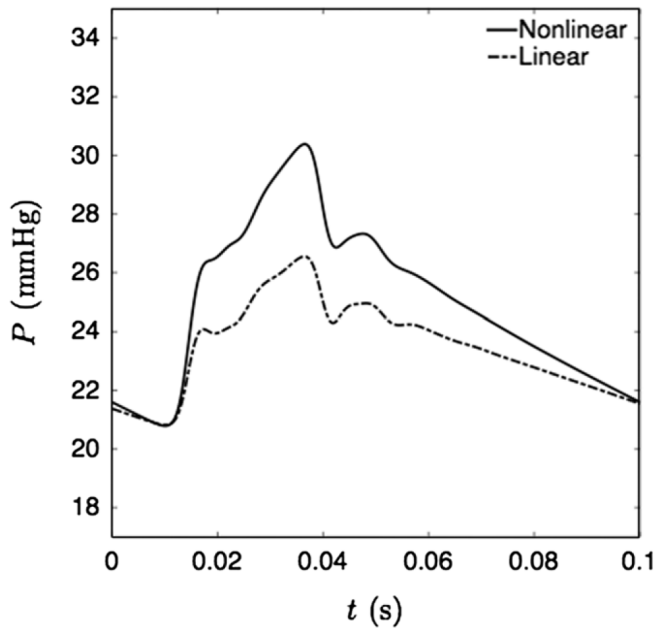


Figure 3.21: Mean pressure waveforms in the main pulmonary artery (MPA) of the simulations of the heterogeneous linear (dashed line) and heterogeneous non-linear (solid line) models. (Source: [16, p. 1256])

Table 3.3: Overview of the literature review of papers which used the one-dimensional non-linear Navier-Stokes equations for modelling the pulmonary circulation.

| | **Li and Cheng [17]** | **Qureshi et al. [23]** | **Clipp and Steele [7]** | **Lee et al. [16]** |
|---|---|---|---|---|
| species | human | human<br>*4 groups:* healthy, PAH, HLD, CTEPH | lamb | mouse |
| modelled geometry | 17 generations including arterial capillary and venous vessels | all arteries and veins with radii $\geq 50\ \mu$m;<br>veins and arteries $> 4.5$ mm were modelled explicitly | MPA $+ 3 - 4$ levels of evolving vessels (34 vessel outlets);<br>3 zones of respiration | 4 generations (13 vessels)<br>comparing heterogeneous and homogeneous vessel wall properties |
| geometry data obtained from | | MRI & literature | lamb cast | measurements by micro-CT |
| modelling equations | 1D non-linearised Navier-Stokes equations including friction and external force (3.72), (3.73), (3.74) | 1D non-linearised Navier-Stokes equations (3.69), (3.75), (3.76)<br>small vessels described via structured trees | 1D non-linearised Navier-Stokes equations (3.69), (3.81),(3.76) for expiration and inspiration | 1D non-linearised Navier-Stokes equations (3.69), (3.75) together with<br>($a$) (3.76) linear relation or<br>($b$) (3.82) non-linear relation |

Table 3.3 – continued from previous page

| | **Li and Cheng [17]** | **Qureshi et al. [23]** | **Clipp and Steele [7]** | **Lee et al. [16]** |
|---|---|---|---|---|
| boundary conditions | | | | |
| inlet | measured RV pressure curve | *arterial:* MRI measured flow rate waveform of MPA<br>*venous:* admittance matrix of structured trees | measured blood flow waveform during expiration | square pulse train with smoothed edges |
| outlet | measured LA pressure | *arterial:* admittance matrix of structured trees<br>*venous:* constant pressure of 2 mmHg | impedance outlet boundary condition via structured trees | 2-element Windkessel applied to terminal arterioles |
| numerical simulation | *interior points:* two-step Lax-Wendroff finite difference method<br>*bifurcation points:* hybrid method of characteristics<br>*boundary points:* partial difference method | two-step Lax-Wendroff numerical scheme<br>*structured trees:* Womersley equations | existing finite element analysis | finite difference method including backward Euler, second order Runge Kutta and Godunov upwind method |

Table 3.3 – continued from previous page

| | **Li and Cheng [17]** | **Qureshi et al. [23]** | **Clipp and Steele [7]** | **Lee et al. [16]** |
|---|---|---|---|---|
| results | significant pressure drop in precapillary vessels;<br>negative pressure in postcapillaries (collapse of vessels) | *healthy:* pressure in venous large vessels is biphasic<br>*PAH:* increase of peak and pulse pressure and dircrotic notch tends to disappear in MPA<br>*HLD:* peak, trough & mean arterial pressure increase significantly; single peak in pressure wave of MPA; pressure & flow waves peak earlier in pulmonary veins<br>*CTEPH:* earlier, steeper & higher pressure peak followed by second one | results for fitting outlet boundary condition in terms of<br>(*a*) *expiration:* 2 zonal model better than 3 zonal model; zonal $l_{rr}$ better than global $l_{rr}$<br>(*b*) *inspiration:* for 2 zones is zonal $l_{rr}$ and zonal $f_R$ the best choice, for 3 zones is zonal $l_{rr}$ and global $f_R$ the best choice | pressure of heterogeneous linear model is significantly smaller than in the heterogeneous non-linear model<br>results of homogeneous and heterogeneous model are not significantly different<br>the non-linear model overestimates the amplitude of incident & reflected waves compared to the linear model |

# 4 Comparison and Discussion of the Mathematical Models

In this section the differences and similarities of the three examined approaches of modelling the pulmonary circulation considered in Section 3 will be discussed. Therefore, the modelling equations of these approaches will be briefly recapitulated.

The simplest formulation of modelling the pulmonary circulation as a Windkessel is given in Section 3.1.1 by a 2-element Windkessel and specified by equation (3.2)

$$\dot{p}(t) + \frac{1}{R_p C_a} p(t) = \frac{1}{C_a} q(t),$$

with $p$ being the pressure, $q$ the flow, $R_p$ the peripheral resistance and $C_a$ the arterial compliance. Considering the characteristic impedance $Z_c$, leads to the 3-element Windkessel model described by equation (3.6), that is

$$p(t) = Z_c q(t) + p_{WK}(t),$$

where $p_{WK}(t)$ is the solution of the 2-element Windkessel model. The third Windkessel model considered was the parallel 4-element Windkessel model, which is given by equation (3.7)

$$p(t) = L\dot{q}(t) + Z_c q(t) + p_{WK}(t).$$

Here, $p_{WK}(t)$ again stands for the solution of the 2-element Windkessel model and $L$ is the fourth parameter of this model and represents the inertance.

The second approach taken into account are the Womersley equations given in Section 3.2.1 by the equations (3.42) and (3.43)

$$0 = \frac{\partial q}{\partial x} + \frac{A}{\rho c_0^2} \frac{\partial p}{\partial t},$$
$$\rho \frac{\partial q}{\partial t} + A \frac{\partial p}{\partial x} = -i\rho\omega \frac{F_{10}(\Omega)}{1 - F_{10}(\Omega)} q.$$

Here, $p$ and $q$ again are the pressure and the flow in the vessel. Furthermore, $A$ is the cross-sectional area of the considered vessel, $\rho$ the blood density, $c_0$ the wave speed, $\omega$ the angular velocity and $F_{10}(\Omega)$ is the Womersley function with $\Omega$ being the Womersley number.

The last approach considered here is that of the non-linear one-dimensional Navier-Stokes equations discussed in more detail in section 3.3.1 and given by equations (3.69)-(3.71)

$$\begin{aligned}\frac{\partial q}{\partial x} + \frac{\partial A}{\partial t} &= 0,\\ \rho\frac{\partial q}{\partial t} + \rho\alpha\frac{\partial \frac{q^2}{A}}{\partial x} + A\frac{\partial p}{\partial x} &= 2\pi\mu s'(1)\frac{q}{A},\\ p - p_{ext} &= Eh\sqrt{\pi}\frac{\sqrt{A}-\sqrt{A_0}}{\sqrt{A_0}}.\end{aligned}$$

Again, $p$ represents the pressure and $q$ the flow. Moreover, $A$ is the variable cross-sectional area and hence not seen as a parameter in this modelling approach. Therefore, $A_0$ is the cross-sectional area at $t = 0$. The further parameters are $\rho$, standing again for the blood density, $\alpha$, describing the correction coefficient, $\mu$, representing the dynamic viscosity of the blood and $s$, being a function of the radial coordinate and the radius of the vessel and describing the velocity profile of the blood. Furthermore, $E$ is the Young-modulus, $h$ the vessel wall thickness at $t = 0$ and $p_{ext}$ the external pressure.

Table 4.1 shows an overview of the characteristics of these three models. The main differences between the models based on the Navier-Stokes equations, specifically the Womersley equations and the one-dimensional non-linear Navier-Stokes equations, and the simple Windkessel models are that the latter ones only depend on time $t$ and do not take spatial distribution into account. Moreover, the Windkessel models depend on ordinary differential equations compared to systems of partial differential equations for the models based on the Navier-Stokes equations. Also the number of variables and parameters as well as the number of boundary conditions needed is differing in all three models. Furthermore, the one-dimensional non-linear Navier-Stokes equations are the only modelling approach considered in this thesis, which is described by a non-linear system. The main difference between the two considered types of modelling the pulmonary circulation based on the Navier-Stokes equations is, that for the derivation of the Womersley equations stronger assumptions are required. Two of these assumptions are that the wave length is much larger than the vessel radius at time $t = 0$ as well as that the wave velocity is assumed to be large compared to the average flow velocity. Further assumptions for the derivation of the Womersley equations are that the cross-sectional area $A$ is not directly depending on $t$ and that $\frac{\partial A}{\partial p}$ is assumed to be constant. Hence, this might be seen as a disadvantage of the Womersley equations and on the other hand as an advantage of the one-dimensional non-linear Navier-Stokes equations. A further advantage is, that for example via structured tree boundary conditions the influence of the small vessels can be determined differently to the linearised approach. But finding the adequate boundary condition might not be an easy task and therefore is also an disadvantage of the one-dimensional non-linear Navier-Stokes equations. Moreover, also possible wave reflections at bifurcations and hence forward and backward travelling pressure and flow waves can be considered with the models based on the Navier-Stokes equations. It is not possible to take these features of pressure and flow waves into account by the Windkessel model since it is a lumped parameter model. But on the other hand the Windkessel modelling method

is easier to handle. Its usage for simulation is also straight forward and all considered parameters have physiological meanings. Furthermore, the simulation results in literature showed that via the parameters of the Windkessel models there is a possibility to distinguish patients suffering from different types of pulmonary hypertension as well as various disease stages. On the other hand, it is remarkable that the $RC$-time was identified to be constant independent of the patients and hence also independent of the type of pulmonary hypertension and its disease order. This leads to the assumption of $R$ and $C$ being inversely related. But the simulation results from literature showed that it is also possible to distinguish between patients suffering from pulmonary hypertension and healthy patients by using the Womersley equations approach as well as using one-dimensional non-linearised Navier-Stokes equations. Referring to this, the phase velocity as well as the characteristic impedance of patients without pulmonary hypertension are significantly lower than in patients with pulmonary hypertension considering the Womersley equations. Furthermore, by this modelling approach spectra shifted to the right with increasing disease stage are obtained. In this context, the simulation results of one-dimensional non-linear Navier-Stokes equations also show characteristics for different patient groups. The pressure waveform, especially the pressure peak and the dicrotic notch, tends to show different characteristics in different types of pulmonary hypertension. This modelling approach was not only used to find properties to differentiate various kinds of pulmonary hypertension, but also to investigate zonal depending respiratory models as well as comparing the effects of using homogeneous and heterogeneous vessel wall properties. Moreover, a non-linear relation of pressure and vessel radius was compared to the common linear relation, which is stated in the last of the modelling equations for the one-dimensional non-linear Navier-Stokes approach given above. However, this results in an overestimation of the amplitude of the incident and reflected waves compared to the linear pressure and vessel radius relation.

Altogether, the three considered modelling methods show significant differences not only in their corresponding modelling equations and their derivations but also in terms of complexity, possibilities of applications and simulation results.

Table 4.1: Overview of characteristics of the three modelling approaches - Windkessel models, Womersley equations and one-dimensional non-linear Navier-Stokes equations - which all were discussed in further detail in Chapter 3.

| | **Windkessel model** | **Womersley equations** | **1D non-lin. Navier-Stokes eq.** |
|---|---|---|---|
| dimension | 0-dimensional | 1-dimensional | 1-dimensional |
| linearity | linear | linear | non-linear |
| type of differential equation | ordinary differential equation | system of partial differential equations | system of partial differential equations |
| order | first order | first order | first order |
| assumptions | - whole arterial tree is seen as one compartment $\Rightarrow$ lumped parameter model<br>- no wave reflections or wave transmissions | - blood is an incompressible Newtonian fluid $\Rightarrow \mu, \rho = const.$<br>- uniform elastic tube with constant length and circular cross-sectional area<br>- shear stress and velocity gradient are linearly correlated<br>- gravitation and external forces are neglected<br>- axisymmetric flow field (independence of angular velocity component and $\theta$)<br>- non-slip boundary condition at vessel wall<br>- matching boundary condition<br>- $A$ not explicitly depending on $t$<br>- $\frac{\partial A}{\partial p} = const.$<br>- $\lambda \gg r_0$<br>- $c_0 \gg \bar{u}$ | - blood is an incompressible Newtonian fluid $\Rightarrow \mu, \rho = const.$<br>- uniform elastic tube with constant length and circular cross-sectional area<br>- shear stress and velocity gradient are linearly correlated<br>- gravitation and external forces are neglected<br>- axisymmetric flow field (independence of angular velocity component and $\theta$)<br>- non-slip boundary condition at vessel wall<br>- matching boundary condition<br>- $\frac{\partial u_x}{\partial x}$ is negligible |

Table 4.1 – continued from previous page

| | **Windkessel model** | **Womersley equations** | **1D non-lin. Navier-Stokes eq.** |
|---|---|---|---|
| variables of model | $p$ pressure | $p$ pressure<br>$q$ flow | $p$ pressure<br>$q$ flow<br>$A$ cross-sectional area |
| expressions (parameters, functions, ...) used in the modelling equations | $R$ resistance<br>$C$ compliance<br>$Z$ characteristic impedance<br>$L$ inertance | $A$ cross-sectional area<br>$\rho$ density<br>$c_0$ inviscid wave velocity<br>$\omega$ angular frequency<br>$F_{10}(\Omega)$ Womersley function | $\rho$ density<br>$\mu$ dynamic viscosity<br>$E$ Young's modulus<br>$h$ wessel wall thickness<br>$\alpha$ correction coefficient<br>$s$ function describing the velocity profile<br>$p_{ext}$ external pressure<br>$A_0$ cross-sectional area at $t = 0$ |
| initial values | *pressure:*<br>- measured $p_0$<br>- arbitrary $p_0$ | *pressure:*<br>measured $p_0$<br>*flow:*<br>measured $q_0$ | *pressure:*<br>measured $p_0$<br>*flow:*<br>measured $q_0$ |
| boundary conditions/ input of the models used in literature | input<br>$q$ flow; represents the right side of the equation | one boundary condition needed<br>*inlet:*<br>- measured pressure (MPA, LA)<br>- measured flow (MPA) | two boundary conditions needed<br>*inlet:*<br>- measured pressure curve of RV<br>- measured flow curve of MPA<br><br>*outlet:*<br>- measured pressure in LA<br>- 2-element Windkessel model<br>- structured trees |

Table 4.1 – continued from previous page

| | **Windkessel model** | **Womersley equations** | **1D non-lin. Navier-Stokes eq.** |
|---|---|---|---|
| modelled geometry used in literature | - whole pulmonary arterial system lumped together<br>- 17 generations of the arterial system via RC-tree model | - MPA (large arteries)<br>- arterial & venous system | varying from considering only 4 generations up to all vessels with radii $\geq 50\ \mu$m |
| simulation methods used in literature | ode solver | Fourier analysis/ transformation computation of coefficients of forward and backward pressure and flow waves of the analytical solutions | finite difference methods,<br>finite element method |
| simulation results in literature | constant $RC$-time throughout all patients, independent of disease type and stage $\Rightarrow$ inverse relationship between $R$ and $C$<br>considering pressure dependent compliance leads to more realistic results<br>$R$ is increasing with disease stage<br>$C$ decreases with disease severity | pressure pulse acts contrarily to flow (pressure is peaked during systole and flattens during diastole)<br>pressure is also damped considerably more in small arteries and the capillary bed than flow<br>pulmonary hypertension patients can be differentiated from NONPH patients due to lower phase velocity and characteristic impedance in NONPH patients<br>the spectra are also shifted to the right with increasing disease stage | pressure drops significantly in precapillary vessels<br>pressure waveforms differ notably in different pulmonary hypertension groups<br>considering a non-linear relation of pressure and vessel radius (equation (3.82)) instead of the common linear relation (equation (3.71)) leads to an overestimation of the amplitude of incident and reflected waves |

# 5 Simulation of the Pulmonary Circulation

A 2-element Windkessel model as well as an $RC$-tree model, based on the model of Lankhaar [14], were considered for simulation of the pressure of the pulmonary arterial system. The $RC$-tree model was already roughly described in Section 3.1.2, but in Section 5.2 it will be explained in more detail. Both models were implemented in MATLAB, version 8.2.0.701 (R2013b) on a personal computer (Intel Core i5-6200U, 2.3-GHz CPU with 8-GB RAM). For all simulations, as in the PhD thesis of Lankhaar [14], a stroke volume of 80 ml and a heart rate of 70 beats per minute were considered. Furthermore, as input to the models, a triangular flow peaking at one third of the systole is taken into account. Diastole and thus zero flow starts at one third of the regarded heart beat period.

## 5.1 Implementation of a 2-element Windkessel Model

For comparison with the later described $RC$-tree model, a 2-element Windkessel model, as described in Section 3.1.1, was considered for implementation. The modelling equation is given by (3.2), specifically by

$$\dot{p}(t) = -\frac{1}{R_p C_a} p(t) + \frac{1}{C_a} q(t).$$

The above mentioned triangular flow and the pressure $P_0$ at time $t = 0$ served as input to the model. $P_0$ was arbitrarily set equal to 0 since pressure $p$ and flow $q$ are periodic and the system is stabilising after few cardiac cycles independent of the chosen initial value. Before simulation, also values for the parameters $R_p$ and $C_a$ have to be defined. Afterwards the ordinary differential equation describing the 2-element Windkessel model is solved numerically by a stiff ODE solver pre-implemented in MATLAB. Such a solver is applied to the differential equation since the factor $-\frac{1}{R_p C_a}$, by which $p(t)$ is multiplied, is smaller than 0 and thus the differential equation is stiff [22].

## 5.2 Implementation of an $RC$-tree Model

An $RC$-tree model, based on the $RC$-tree model developed by Lankhaar [14], was implemented. Its advantage is that it distributes resistance and compliance over several generations of vessels. Thus, compared to a single 2-element Windkessel model it is not an utterly lumped parameter model.

For the $RC$-tree model $N = 17$ generations of pulmonary arterial vessels were taken into account. The order of a generation is denominated by $k$ with $k \in \{1, \ldots, N\}$. The number of daughter vessels of a parent vessel of order $k$ is represented by $\alpha_k$, $k \in \{1, \ldots, N\}$. The model is basically built of three sections: the entrance, middle and terminating sections (see also

Figure 3.10). The MPA is represented by the entrance section and thus modelled by a 2-element Windkessel. Each of the other vessels is also represented by a 2-element Windkessel model. All generations are connected in series, while all vessels, also referred to as segments, within one generation are seen as parallel. Furthermore, all segments of the same order $k$ are assumed to be equal and thereby have the same resistance $r_k$, compliance $c_k$ and number of daughters $\alpha_k$. For the terminating section, illustrated in Figure 3.10, resistances of the vessels of the subsequent generation are needed for the termination of the model. As already mentioned, they are assumed to be equal for all vessels of that order and hence given by $r_{N+1}$. Altogether, the model consists of $N-1$ generations following the entrance section. Each order $k = 2, ..., N-1$ has in total $n_k$ middle sections and the total number of terminating sections is given by $n_N$. In detail, $n_k$ is given by $n_1 = 1$ and $n_k = \prod_{i=1}^{k-1} \alpha_i$ for $k = 2, ..., N$. In the pulmonary arterial tree different parent vessels of the same order $k$ can have different numbers of daughter vessels, thus $\alpha_k$ is not obligatory an integer. The differential equation system for the $RC$-tree model is given by

$$\dot{\boldsymbol{x}}(t) = A \cdot \boldsymbol{x}(t) + \begin{pmatrix} \frac{1}{c_1} \\ 0 \\ \vdots \\ 0 \end{pmatrix} \cdot q(t) \tag{5.1}$$

$$p(t) = \boldsymbol{x_1}(t) + r_1 \cdot q(t) \tag{5.2}$$

with

$$A = \begin{pmatrix} -\frac{\alpha_1}{\tau_{21}} & \frac{\alpha_1}{\tau_{21}} & 0 & & & & \\ \frac{1}{\tau_2} & -\left(\frac{1}{\tau_2} + \frac{\alpha_2}{\tau_{32}}\right) & \frac{\alpha_2}{\tau_{32}} & 0 & & & \\ & & \ddots & & & & \\ 0 & & \frac{1}{\tau_k} & -\left(\frac{1}{\tau_k} + \frac{\alpha_k}{\tau_{k+1,k}}\right) & \frac{\alpha_k}{\tau_{k+1,k}} & 0 & \\ & & & \ddots & & & \\ & & & 0 & \frac{1}{\tau_{N-1}} & -\left(\frac{1}{\tau_{N-1}} + \frac{\alpha_{N-1}}{\tau_{N,N-1}}\right) & \frac{\alpha_{N-1}}{\tau_{N,N-1}} \\ & & & & 0 & \frac{1}{\tau_N} & -\left(\frac{1}{\tau_N} + \frac{\alpha_N}{\tau_{N+1,N}}\right) \end{pmatrix}.$$

The parameters $\tau_{ij}$ are given by $\tau_{ij} = r_i c_j$ for all $1 \leq i \neq j \leq N$ and $\tau_i = r_i c_i$ ($= \tau_{ij}$ for $i = j$), respectively. The values for the segmental number of vessels $\alpha_k$, the resistance $r_k$ and the compliance $c_k$, which were taken from [14] and used for simulation, are given in Table 5.1. In this table two different values for $r_k$ are given for generations 11 to 18. This is due to Lankhaar [14] listing different values for the resistances in these generations than those which were depicted in [14, Figure 10.3]. The mentioned differences are also illustrated in Figure 5.2.

The given differential equation (5.1) and consideration the data from Table 5.1 let conclude that all eigenvalues of the matrix $A$ are real and negative. Furthermore, the ratio $\frac{max_{\lambda \in \Lambda}|\mathrm{Re}(\lambda)|}{min_{\lambda \in \Lambda}|\mathrm{Re}(\lambda)|}$ with $\Lambda$ being the set of all eigenvalues of $A$ is of order $10^4$. Thus, a MATLAB ODE solver for

Table 5.1: For each order $k$ the values for $\alpha_k$, segmental resistance $r_k$ and compliance $c_k$ are tabulated as given in [14]. The first column of $r_k$ lists the resistances given in [14, Table 10.1] and the second column of $r_k$ belongs to the values, which were taken from [14, Figure 10.3 A].

| $k$ | $\alpha_k$ | $r_k$ (table) | $r_k$ (figure) | $c_k$ |
|---|---|---|---|---|
| 1 | 3.0 | $1.09 \cdot 10^{-4}$ | $1.09 \cdot 10^{-4}$ | $1.38 \cdot 10^{0}$ |
| 2 | 2.67 | $6.46 \cdot 10^{-4}$ | $6.46 \cdot 10^{-4}$ | $1.19 \cdot 10^{-1}$ |
| 3 | 2.5 | $2.52 \cdot 10^{-3}$ | $2.52 \cdot 10^{-3}$ | $1.20 \cdot 10^{-2}$ |
| 4 | 3.3 | $1.76 \cdot 10^{-2}$ | $1.76 \cdot 10^{-2}$ | $1.18 \cdot 10^{-2}$ |
| 5 | 3.08 | $9.84 \cdot 10^{-2}$ | $9.84 \cdot 10^{-2}$ | $5.90 \cdot 10^{-3}$ |
| 6 | 3.33 | $5.37 \cdot 10^{-1}$ | $5.37 \cdot 10^{-1}$ | $1.13 \cdot 10^{-3}$ |
| 7 | 3.39 | $2.06 \cdot 10^{0}$ | $2.06 \cdot 10^{0}$ | $3.35 \cdot 10^{-4}$ |
| 8 | 2.65 | $8.77 \cdot 10^{0}$ | $8.77 \cdot 10^{0}$ | $9.72 \cdot 10^{-5}$ |
| 9 | 3.1 | $4.06 \cdot 10^{1}$ | $4.06 \cdot 10^{1}$ | $2.50 \cdot 10^{-5}$ |
| 10 | 3.09 | $1.35 \cdot 10^{2}$ | $1.35 \cdot 10^{2}$ | $7.42 \cdot 10^{-6}$ |
| 11 | 3.1 | $5.35 \cdot 10^{2}$ | $4.91 \cdot 10^{2}$ | $1.99 \cdot 10^{-6}$ |
| 12 | 3.15 | $2.45 \cdot 10^{3}$ | $2.11 \cdot 10^{3}$ | $4.97 \cdot 10^{-7}$ |
| 13 | 3.15 | $1.16 \cdot 10^{4}$ | $8.58 \cdot 10^{3}$ | $1.38 \cdot 10^{-7}$ |
| 14 | 3.15 | $5.05 \cdot 10^{4}$ | $3.28 \cdot 10^{4}$ | $2.17 \cdot 10^{-8}$ |
| 15 | 3.6 | $2.12 \cdot 10^{5}$ | $1.23 \cdot 10^{5}$ | $5.66 \cdot 10^{-9}$ |
| 16 | 3.6 | $1.00 \cdot 10^{6}$ | $5.05 \cdot 10^{5}$ | $1.49 \cdot 10^{-9}$ |
| 17 | 0.32 | $4.44 \cdot 10^{6}$ | $1.97 \cdot 10^{6}$ | $5.44 \cdot 10^{-10}$ |
| 18 | | $1.44 \cdot 10^{6}$ | $7.17 \cdot 10^{5}$ | |

stiff differential equations is applied to equation (5.1). [22]

The above mentioned triangular flow $q$ at the entrance section is serving as the input of the model. Furthermore, an initial value for $\boldsymbol{x}$ has to be defined. This value is again chosen arbitrarily as 0 for the same reasons as given in Section 5.1 since the entries of $\boldsymbol{x}$ represent the pressures at the nodes of the corresponding order. With the defined values for $\alpha_k$, $r_k$ and $c_k$ equation (5.1) can be solved numerically via a stiff ODE solver, as already mentioned. Via the obtained solution for $\boldsymbol{x}$, pressure $p$ at the entrance section and hence the output of the model can be subsequently calculated by equation (5.2).

In terms of calculation of the total $RC$-time of this model, total resistance and compliance have to be determined by the total order resistances and compliances. The total order resistance $R_k$ of order $k$, resulting from parallel segments, can be calculated by

$$\begin{aligned} R_1 &= r_1 \qquad \text{and} \\ R_k &= \frac{r_k}{n_k} = r_k \prod_{i=1}^{k-1} \frac{1}{\alpha_i} \qquad \text{for} \quad k \in \{2, ..., N\}, \end{aligned} \tag{5.3}$$

which is described in more detail in [14]. Since the generations are connected in series, the total tree resistance $R$ is obtained by

$$R = \sum_{k=1}^{N} R_k = \sum_{k=1}^{N} \frac{r_k}{n_k} = r_1 + \sum_{k=2}^{N} r_k \prod_{i=1}^{k-1} \frac{1}{\alpha_i}. \tag{5.4}$$

Analogously, total order compliance $C_k$ of order $k$ is given by

$$C_1 = c_1 \qquad \text{and}$$
$$C_k = c_k n_k = c_k \prod_{i=1}^{k-1} \alpha_i \qquad \text{for} \quad k \in \{2, ..., N\}, \tag{5.5}$$

and total tree compliance $C$ is calculated by

$$C = \sum_{k=1}^{N} C_k = \sum_{k=1}^{N} c_k n_k = c_1 + \sum_{k=2}^{N} c_k \prod_{i=1}^{k-1} \alpha_i. \tag{5.6}$$

The computed total resistance $R$ and total compliance $C$ are also used as parameters for simulation of the 2-element Windkessel model.

In particular, the $RC$-tree model was also used to simulate occlusion and the loss of vessels. This was realised by reduction of $\alpha_k$ of a given order $k$. Thereby, equations (5.3) and (5.5) imply that the total resistances and compliances of the orders $j > k$ are changed as well.

## 5.3 Results

This section will provide some basic simulation results of the $RC$-tree model. First of all, a comparison of the total order resistances $R_k$ for different values of $r_k$ will be done. Moreover, the simulated pressure of the default case (no occlusion) will also be compared to the result of a single 2-element Windkessel model. Furthermore, occlusion will be simulated for various generations and percentages of occlusion.

For all further simulations the MATLAB ODE solver "ode15s" was applied to the differential equations (3.2) and (5.1). This is due to better accuracy when using a smaller maximum step size (see also Figure 5.1) compared to the MATLAB ODE solver "ode23s". Also the number of needed time steps did not differ significantly for the "ode23s" and "ode15s" solvers for maximum step sizes less than or equal to $1 \cdot 10^{-2}$ s (see Table 5.2). Simulation results obtained with maximum step sizes smaller than $1 \cdot 10^{-4}$ s did not show significant differences to the solution calculated with this threshold. Thus, a maximum step size of $1 \cdot 10^{-4}$ s and a time interval representing 20 cardiac cycles was chosen to obtain a best approximated and truly periodic solution for all simulations. All these results were obtained by only taking the second column of $r_k$ of Table 5.1 into consideration.

On the left side of Figure 5.2 the total order resistances $R_k$ for both cases of segmental resistances $r_k$, given in Table 5.1, are plotted against their corresponding order $k$. It is notable that the resistances only differ in generations 11 to 18. The according pressures $p$ are shown on the right side of this figure. Based on these results the second column of the segmental resistances $r_k$ of Table 5.1 is chosen. This is due to an unrealistic high pressure for the other values. Although they are referred to as "normal" in [14], their pressure ranges between 21 mmHg and 36 mmHg. Normally, in case of no hypertension, the maximum pressure is less than or equal to 25 mmHg.

Table 5.2: Comparison of the number of time steps needed for calculation of the numerical solution of differential equation (5.1) by the MATLAB routines "ode15s" (red) and "ode23s" (blue) for simulation of 10 cardiac cycles with different maximas for the step size. Here, only 10 cardiac cyclces were simulated since a truly periodic solution can already be obtained by this number of cycles for the default case (second column for $r_k$ of Table 5.1).

| maximum step size | ode15s | ode23s |
|---|---|---|
| $1 \cdot 10^{-1}$ | 438 | 302 |
| $1 \cdot 10^{-2}$ | 927 | 913 |
| $1 \cdot 10^{-3}$ | 8597 | 8592 |
| $1 \cdot 10^{-4}$ | 85721 | 85716 |

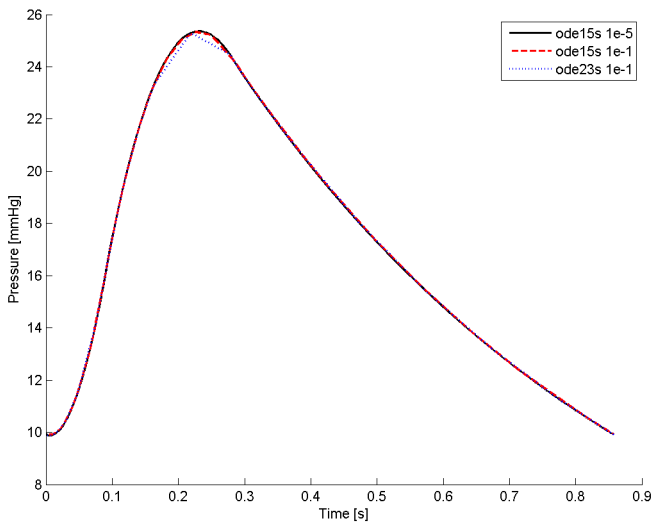


Figure 5.1: Comparison of the accuracy of the numerical solutions for the pressure of the $RC$-tree model obtained by the MATLAB functions "ode15s" and "ode23s" with a maximal step size of $1 \cdot 10^{-1}$ s. The black line shows the solution estimated via the "ode15s" solver with a maximum step size of $1 \cdot 10^{-5}$ s representing the assumed best approximation of the solution.

Simulated blood pressure at the entrance section of the $RC$-tree model was set in contrast to the blood pressure simulated by a single 2-element Windkessel model. The corresponding parameters $R$ and $C$ for the single 2-element Windkessel model were obtained by the total resistance and compliance of the $RC$-tree model. Additionally, blood pressure was also simulated by a 2-element Windkessel model with parameters given in [14], which were referred to as the default values of the $RC$-tree. These three pressure curves are depicted in Figure 5.3. Note that the maximum of the $RC$-tree pressure (blue solid line) is about 0.5 mmHg higher than the maximum of the 2-element Windkessel pressure arising from the calculated total tree resistance and compliance (red dash-dotted line). The minima of the pressures of these two methods differ about the same amount. Furthermore, it can be seen that the pressure simulated by this 2-element Windkessel model peaks a little bit later. It also increases before the peak and

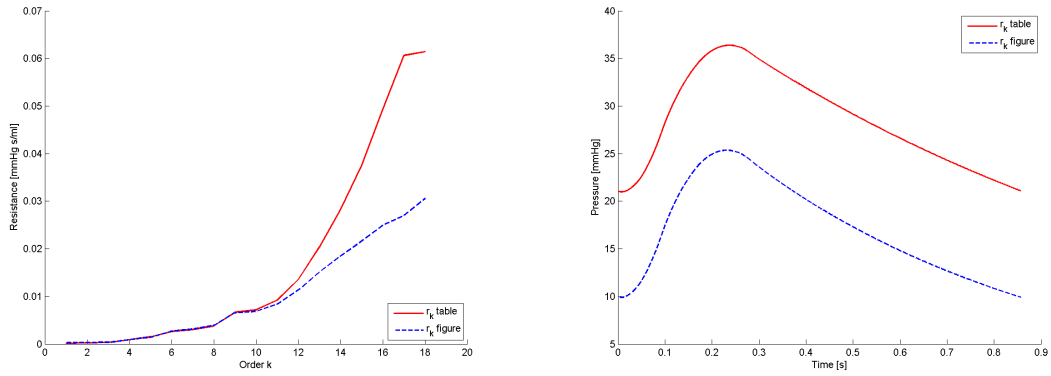


(a) Total order resistances $R_k$

(b) Blood pressure for different values of segmental resitances $r_k$

Figure 5.2: Comparison of (a) the total order resistances $R_k$ based on the segmental resistances $r_k$ and (b) of their resulting pressures at the entrance of the $RC$-tree. The different values for $r_k$ are given in Table 5.1. In the legend of the graphics $r_k$ *table* refers to the first column and $r_k$ *figure* to the second column of the considered resistances in the table.

decreases after the peak slower than the $RC$-tree pressure. The pressure waveform representing the 2-element Windkessel model with the default values of Lankhaar [14] (green dashed line) seems to represent the simulated $RC$-tree pressure waveform very well.

### 5.3.1 Simulation Results for Occlusion

Occlusion of vessels of the pulmonary arterial tree in general can occur in healthy persons as well as in persons suffering from several diseases, for example hypoxia or CTEPH.

In terms of occlusion various factors for decreasing the number of daughters $\alpha_k$ of a specific generation $k$ have been taken into account. These factors were ranging from 1 (no occlusion) up to 0.15 (85% of the vessels of the considered order are occluded). The generation primarily affected by occlusion ranged from order 5 to order 17. As already mentioned, occlusion in a specific generation $k$ affects all subsequent generations as well. This is due to changes in total order resistance and compliance of all orders $j > k$.

Blood pressure affected by occlusion is exemplary given in Figure 5.4 for generations 5, 9, 13, 15, 16 and 17 for various factors causing a decrease of $\alpha_k$. It can be seen that the factor 0.15 leads to a blood pressure ranging from about 101 mmHg to 122 mmHg for $k = 5$. For $k = 17$ the blood pressure ranges from 26 mmHg up to 41 mmHg for this factor. Altogether, the graphics show that the magnitude of the blood pressure in the MPA is most influenced by this factor independent of the order of occlusion. Least effects on the blood pressure are seen by a factor of 0.85 (15% of the vessels are occluded) throughout all orders of occlusion. For the small pulmonary arterioles (coinciding with high generation number) the factor 0.85 does not influence the blood pressure notably, especially for orders $k = 16$ and $k = 17$. It is also remarkable that the magnitude of the blood pressure, independent of the factors of occlusion,

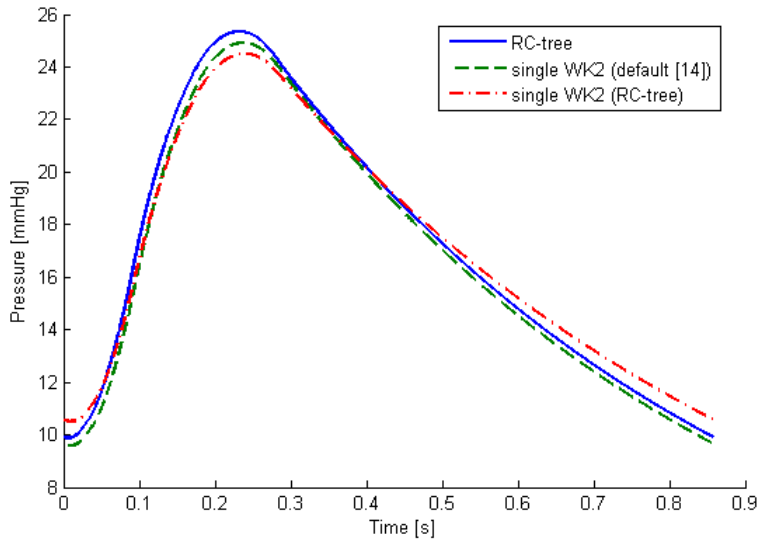


Figure 5.3: Simulated blood pressures of the $RC$-tree model (blue) for the "normal" case and the corresponding 2-element Windkessel models are shown. For the single 2-element Windkessel model the calculated total tree resistance and compliance (red) $R \approx 0.18$ mmHg s/m, $C \approx 3.8$ ml/mmHg as well as parameters taken from [14] (green) ($R = 0.18$ mmHg s/m, $C = 3.5$ ml/mmHg) were used.

is decreasing significantly with increasing order of occlusion.

Figure 5.5 shows the same generations and factors for decreasing $\alpha_k$ (0.85, 0.7, 0.5, 0.3, 0.15) as Figure 5.4, but in a rearranged way. The difference between Figure 5.5 and Figure 5.4 is that in Figure 5.5 the factors are fixed and the order $k$ of occlusion varies while in Figure 5.5 the orders were fixed and the factors were varying. The results for occlusion of order 5 and 7 tend to coincide. This property can especially be investigated at the beginning of systole and at the end of diastole throughout all factors of occlusion. Furthermore, it can be seen that with increasing percentage of occluded vessels the blood pressure waveforms significantly increase. Looking at the distance of two pressure waveforms of neighbouring generations, it can be observed that these distances remarkably raise with increase of occlusion. This effect can be especially noticed in vessels of higher orders.

Moreover, Figure 5.6 shows on the left side the total tree resistances $R$ for various factors (0.85, 0.7, 0.5, 0.3, 0.15) of occlusion. Occlusion was separately applied to each generation of the orders 5 to 17. On the right side the according total tree compliances $C$ are depicted. Only when higher factors of occlusion are taken into account, specifically when 70% or 85% of the vessels of considered order are occluded, the resistance is increasing evenly when the order $k$ of occlusion decreases. Contrariwise, compliance is decreasing with decreasing order $k$ of occlusion. Occlusion of only small arteries does not increase the corresponding compliance. Thus, in contrast to Lankhaar's results given in [14, Figure 10.4], it does not rise above the compliance that is related to no occlusion. This difference is due to different values of total

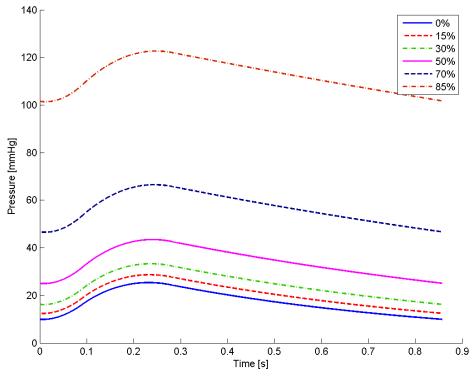


(a) Order $k = 5$

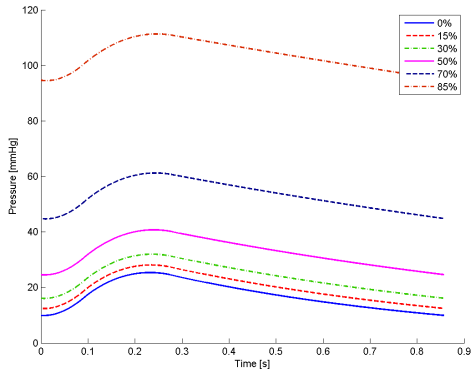


(b) Order $k = 9$

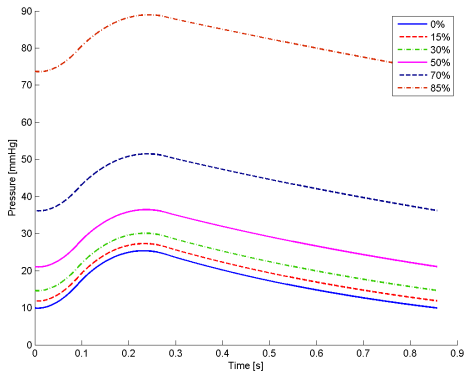


(c) Order $k = 13$

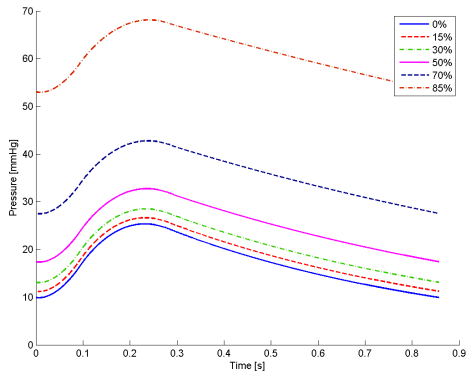


(d) Order $k = 15$

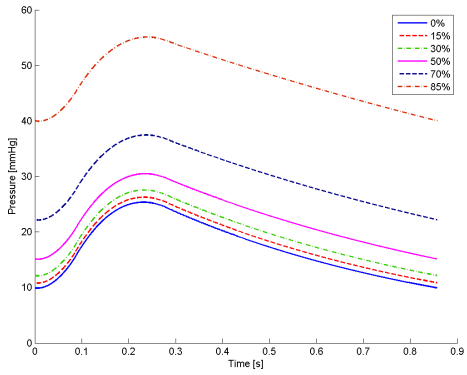


(e) Order $k = 16$

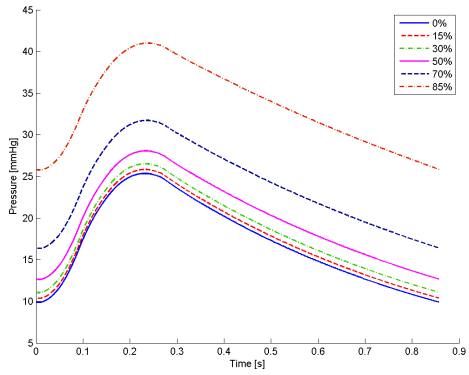


(f) Order $k = 17$

Figure 5.4: Simulated blood pressure at the entrance section of the $RC$-tree affected by various factors (1, 0.85, 0.7, 0.5, 0.3, 0.15) for decreasing the number of daughters $\alpha_k$. Occlusion was considerd at generations of order (a) $k = 5$, (b) $k = 9$, (c) $k = 13$, (d) $k = 15$, (e) $k = 16$ and (f) $k = 17$.

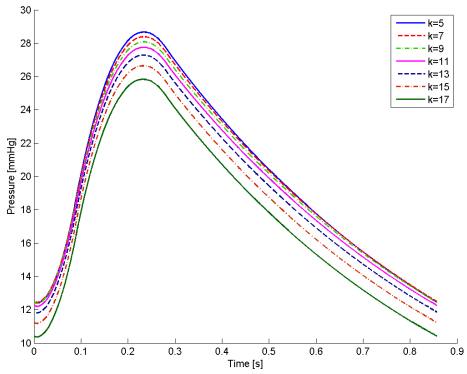


(a) Factor 0.85

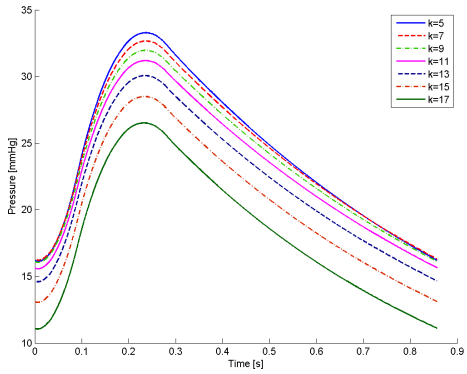


(b) Factor 0.7

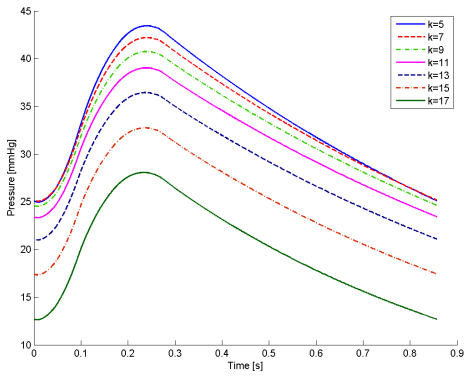


(c) Factor 0.5

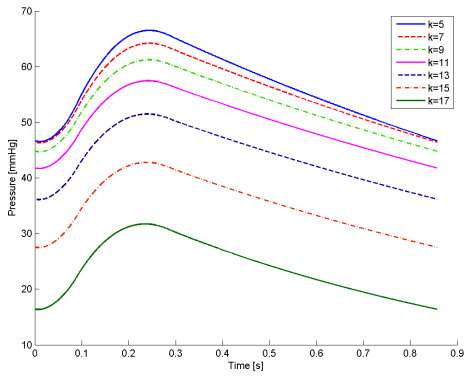


(d) Factor 0.3

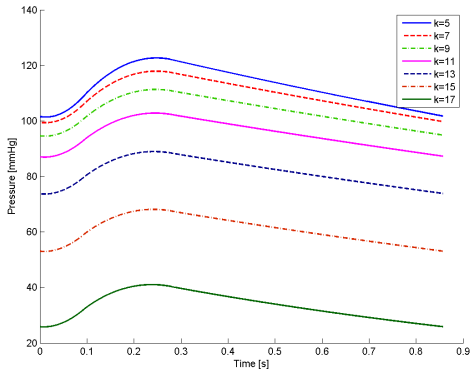


(e) Factor 0.15

Figure 5.5: Simulated blood pressure at the entrance section of the $RC$-tree at various generations ($k \in \{5, 7, 9, 11, 13, 15, 17\}$) affected by various factors to decrease the number of daughters $\alpha_k$. The values of the factors for the increase of occlusion were considerd to be (a) 0.85 (b) 0.7, (c) 0.5, (d) 0.3 and (e) 0.15.

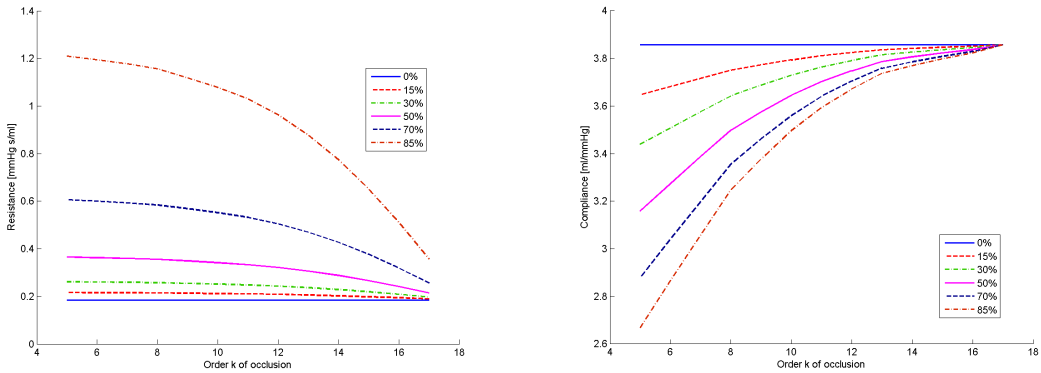


(a) Total tree resistance $R$ over order $k$ that is occluded

(b) Total tree compliance $C$ over order $k$ that is occluded

Figure 5.6: Simulated (a) total tree resistances $R$ and (b) compliances $C$ in respect to various factors (0.85, 0.7, 0.5, 0.3, 0.15) for decreasing $\alpha_k$ in terms of occlusion. Generations primarily affected by occlusion were considered to be ranging from orders 5 to 17.

tree compliance. In [14] $C$ took the value of 3.5 ml/mmHg for the "normal" case. Contrariwise, considering the values given in Table 5.1 and applying equation (5.6) leads to a compliance of $\approx 3.8$ ml/mmHg. In terms of total tree resistance there was no difference.

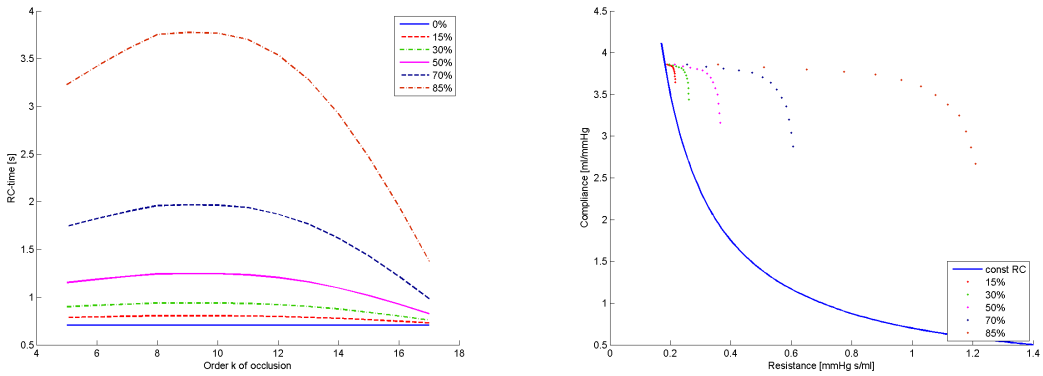


(a) Total $RC$-time over order $k$ that is occluded

(b) Total tree resistance $R$ versus total tree compliance $C$ over order $k$ that is occluded

Figure 5.7: Simulated (a) total $RC$-time and (b) total tree resistance $R$ against total tree compliances $C$ in respect to various factors (0.85, 0.7, 0.5, 0.3, 0.15) for decreasing $\alpha_k$ in terms of occlusion. Generations primarily affected by occlusion were considered to range from orders 5 to 17.

Figure 5.7 illustrates on the left side the total $RC$-times resulting from total tree resistances $R$ and compliances $C$ over the occluded order $k$ ranging from 5 up to 17. The factors of occlusion were again considered to be 1, 0.85, 0.7, 0.5, 0.3 and 0.15. The $RC$-time for the "normal" case (no occlusion) took the value of 0.7097 s. Lankhaar [14] reported an $RC$-time of 0.63 s for the corresponding case. This difference is again due to the difference of the total tree compliances,

as reported before. The right side of this figure shows the relationship between $R$ and $C$. Taking constant compliance into account the reported inverse relationship [15, 24] of $R$ and $C$ cannot be explained. Similar results and conclusion were also reported by Lankhaar [14].

## 5.4 Conclusion

An $RC$-tree model for 17 generations of vessels developed by Lankhaar [14] was implemented and compared to a single 2-element Windkessel model. The resistance $R$ and compliance $C$ used for the single 2-element Windkessel model were calculated by equations (5.4) and (5.6). Here, only constant and not pressure-dependent segmental compliance was considered for modelling the $RC$-tree. An advantage of this RC-tree model compared to a single 2-element Windkessel model is that resistances and compliances of several generations are not lumped together to two single corresponding parameters. Quite the opposite, resistance and compliance are distributed longitudinal over the various generations that were considered for the model. A further advantage of this model is that it would be possible to estimate pressure waveforms at different generations.

This model was also used to simulate and investigate occlusion of vessels of various generations. Also, different amounts of occluded vessels of a given order $k$ were taken into account. All computed values for $R$ and $C$ under occlusion are in the range of possible values for these parameters, which are stated in [24, Table 1].

Furthermore, the obtained simulation results for comparison with a 2-element Windkessel model as well as for occlusion were compared to the results given in [14]. In general the results showed similar qualitative behaviour, but the comparison showed significant differences especially in respect to segmental resistances $r_k$ of orders 11 through 17 and total tree compliance $C$. In the case of no occlusion being present, Lankhaar stated that the total tree compliance is 3.5 ml/mmHg. Contrariwise, the total tree compliance calculated here is about 3.8 ml/mmHg. Thus, the disagreement of the results of the 2-element Windkessel models and of the comparison of the total tree compliance under occlusion can be explained by the difference of the total tree compliances.

Moreover, assuming constant compliance and taking occlusion into account cannot explain the inverse relationship of $R$ and $C$ and thus constant $RC$-time, as stated in [15, 24].

# List of Figures


2.1 Circulation of the blood through the cardiovascular system . . . . . 4
2.2 Anatomy of the Pulmonary Circulation . . . . . 5
2.3 Pressure pulse curve of the pulmonary artery and the RV . . . . . 6
2.4 Pressure Distribution in the pulmonary circulation . . . . . 7
2.5 Classification of the three zones of the lung . . . . . 8
2.6 Different classifications of the pulmonary arterial branching tree . . . . . 10

3.1 2-element Windkessel model . . . . . 13
3.2 3-element Windkessel model . . . . . 14
3.3 4-element Windkessel model . . . . . 15
3.4 Electrical circuit analogue of Bouwmeester's et al. [3] reservoir-wave model . . . 16
3.5 PVR components at each intervention simulated by Bouwmeester et al. [3] . . . 17
3.6 Electrical circuit analogue of the 3-element Windkessel model used by Lungu et al. [18] . . . . . 18
3.7 Parameters of the 3-element Windkessel model used by Lungu et al. [18] . . . . . 19
3.8 Parameter estimations of the 3-element Windkessel model used by Lankhaar et al. [15] . . . . . 20
3.9 Relationship of $R$ and $C$ investigated by Lankhaar et al. [15] . . . . . 20
3.10 Schematic representantion of the entrance, middel and terminating sections of the $RC$-tree model developed by Lankhaar [14] . . . . . 21
3.11 Comparison of measured and computed flow waveforms in the MPA and the pulmonary vein by Wiener et al. [29] . . . . . 36
3.12 Pressure and flow waveforms throughout the whole pulmonary circulation simulated by Wiener et al. [29] . . . . . 37
3.13 Apparent phase velocity, input impedance modulus and input impedance phase calculated by Milnor et al. [19] . . . . . 39
3.14 Average apparent phase velocity calculated by Bargainer [1] . . . . . 40
3.15 Visualisation of an elastic tube for derivation of one-dimensional non-linear Navier-Stokes equations . . . . . 44
3.16 Schematic model representation of Qureshi et al. [23] . . . . . 50
3.17 Illustration of $\alpha$ and $\beta$ numbering of the structured trees . . . . . 52
3.18 Pressure waveforms of the pulmonary circulation of a healthy person by Qureshi et al. [23] . . . . . 53
3.19 Schematic model illustration of the model used by Lee et al. [16] . . . . . 56
3.20 Comparison of pressure waveforms of the heterogeneous non-linear model through one to four generations by Lee et al. [16] . . . . . 57
3.21 Comparison of the heterogeneous linear and non-linear model by Lee et al. [16] . 57

5.1 Comparison of solutions of the $RC$-tree model obtained by "ode15s" and "ode23s" 71
5.2 Comparison of different values for segmental resistances . . . . . 72
5.3 Comparison of $RC$-tree and single 2-element Windkessel pressures . . . . . 73
5.4 Simulated blood pressure affected by various factors of occlusion at specific generations . . . . . 74
5.5 Simulated blood pressure at various generations affected by specific factors of occlusion . . . . . 75
5.6 Variation of total tree resistance and compliance with respect to simulation of occlusion. . . . . 76
5.7 Total $RC$-time and relationship between $R$ and $C$ over occluded order $k$ . . . . . 76

# List of Tables

3.1 Overview of applications of the Windkessel model in literature . . . . . 23
3.2 Overview of applications of the Womersley equations in literature . . . . . 41
3.3 Overview of applications of 1D non-linear Navier-Stokes equations in literature . 58

4.1 Overview of the comparison of the Windkessel, Womersley and 1D non-linear Navier-Stokes modelling approaches . . . . . 64

5.1 Values for $\alpha_k$, $r_k$ and $c_k$ for simulation taken from [14] . . . . . 69
5.2 Comparison of needed time steps for different maximum step sizes of "ode15s" and "ode23s" . . . . . 71

# Bibliography


[1] J. Bargainer. Pulse wave velocity in the main pulmonary artery of the dog. *Circ Res*, 20:630–637, 1967.

[2] J. C. Bouwmeester. *Reservoir-Wave Analysis Applied to the Pulmonary Circulation.* PhD thesis, University of Calgary, 2012.

[3] J. C. Bouwmeester, I. Belenkie, N. G. Shrive, and J. V. Tyberg. Partitioning pulmonary vascular resistance using the reservoir-wave model. *J Appl Physiol*, 115(12):1838–1845, 2013.

[4] K. S. Burrowes. *An Anatomically-Based Mathematical Model of the Human Pulmonary Circulation.* PhD thesis, University of Auckland, 2005.

[5] H. R. Cajigas and R. Awdish. Classification and diagnosis of pulmonary hypertension. *Heart Fail Rev*, 21(3):229–237, 2016.

[6] C. G. Caro, T. J. Pedley, R. C. Schroter, and W. A. Seed. *The Mechanics of the Circulation*, chapter 15 The Pulmonary Circulation, pages 467–505. Cambridge University Press, New York, 2nd edition, 2012.

[7] R. B. Clipp and B. N. Steele. Impedance boundary conditions for the pulmonary vasculature including the effects of geometry, compliance, and respiration. *IEEE Trans Biomed Eng*, 56(3):862–870, March 2009.

[8] X. Descovich. *Randbedingungen für eindimensionale Blutflusssimulation.* Diplomarbeit, Technische Universität Wien, 2008.

[9] Encyclopædia Britannica. Pulmonary circulation. `http://www.britannica.com/science/pulmonary-circulation`, January 2009. Online, accessed 04. April 2016, 16:28.

[10] A. Gerstenmayer. *Modelling pulse wave propagation in the arterial tree for the estimation of aortic blood pressure.* Diplomarbeit, Technische Universität Wien, 2015.

[11] A. C. Guyton and J. E. Hall. *Textbook of Medical Physiology*, chapter 38 Pulmonary Circulation; Pulmonary Edema; Pleural Fluid, pages 444–451. W.B Saunders Company, Philadelphia, Pennsylvania, 10th edition, 2000.

[12] W. Huang, R. T. Yen, M. McLaurine, and G. Bledsoe. Morphometry of the human pulmonary vasculature. *J Appl Physiol*, 81(5):2123–2133, 1996.

[13] R. Klinke and S. Silbernagl, editors. *Lehrbuch der Physiology*, chapter 8.7 Der Lungenkreislauf, pages 181–185. Georg Thieme Verlag, Stuttgart, 3rd edition, 2001.

[14] J. W. Lankhaar. *Hemodynamics of pulmonary hypertension: A model-based analysis*. PhD thesis, Vrije Universiteit Amsterdam, 2008.

[15] J. W. Lankhaar, N. Westerhof, T. J. C. Faes, K. M. J. Marques, J. T. Marcus, P. E. Postmus, and A. Vonk-Noordegraaf. Quantification of right ventricular afterload in patients with and without pulmonary hypertension. *Am J Physiol Heart Circ Physiol*, 291(4):H1731–H1737, 2006.

[16] P. Lee, B. E. Carlson, N. Chesler, M. S. Olufsen, M. U. Qureshi, N. P. Smith, T. Sochi, and D. A. Beard. Heterogeneous mechanics of the mouse pulmonary arterial network. *Biomech Model Mechanobiol*, 15(5):1245–1261, 2016.

[17] C. W. Li and H. D. Cheng. A mathematical model for pulmonary blood circulation. In *Computer-Based Medical Systems, 1990., Proceedings of Third Annual IEEE Symposium on*, pages 397–404, June 1990.

[18] A. Lungu, J. Wild, D. Capener, D. Kiely, A. Swift, and D. Hose. MRI model-based non-invasive differential diagnosis in pulmonary hypertension. *J Biomech*, 47(12):2941–2947, 2014.

[19] W. Milnor, C. Conti, K. Lewis, and M. O'Rourke. Pulmonary arterial pulse wave velocity and impedance in man. *Circ Res*, 25:637–649, 1969.

[20] S. Parragh. *Modelle zur Bestimmung des aortalen Blutflusses basierend auf Optimalitätsbedingungen*. Diplomarbeit, Technische Universität Wien, 2013.

[21] A. Peacock. Pulmonary hypertension. *Eur Respir Rev*, 22(127):20–25, 2013.

[22] A. Quarteroni, R. Sacco, and F. Saleri. *Numerical Mathematics*, chapter 11.10 Stiff Problems, pages 519–521. Texts in Applied Mathematics. Springer New York, 2006.

[23] M. U. Qureshi, G. D. A. Vaughan, C. Sainsbury, M. Johnson, C. S. Peskin, M. S. Olufsen, and N. A. Hill. Numerical simulation of blood flow and pressure drop in the pulmonary arterial and venous circulation. *Biomech Model Mechanobiol*, 13(5):1137–1154, 2014.

[24] N. Saouti, N. Westerhof, P. E. Postmus, and A. Vonk-Noordegraaf. The arterial load in pulmonary hypertension. *Eur Respir Rev*, 19(117):197–203, 2010.

[25] S. Singhal, R. Henderson, K. Horsfield, K. Harding, and G. Cumming. Morphometry of the human pulmonary arterial tree. *Circ Res*, 33(2):190–197, 1973.

[26] M. H. Tawhai, A. R. Clark, and K. S. Burrowes. Computational models of the pulmonary circulation: Insights and the move towards clinically directed studies. *Pulm Circ*, 1(2):224–238, 2011.

[27] F. van de Vosse and van Dongen MEH. *Cardiovascular Fluid Mechanics - Lecture Notes*. Einhoven University of Technology, 1998.

[28] N. Westerhof, J. W. Lankhaar, and B. E. Westerhof. The arterial windkessel. *Med Biol Eng Comput*, 47(2):131–141, 2008.

[29] F. Wiener, E. Morkin, R. Skalak, and A. P. Fishman. Wave propagation in the pulmonary circulation. *Circ Res*, 19(4):834–850, 1966.

[30] M. Zamir. *The Physics of Pulsatile Flow.* Biological Physics Series. Springer, New York, 2000.